Integrated Masters in Chemical Engineering

Simulation of Tubular Reactors for Photocatalytic Applications

Master's Dissertation

Author:

Nuno Gonçalo Pacheco Lourenço

Developed for the Dissertation course unit and carried at:

LSRE - Laboratory of Separation and Reaction Engineering

Associate Laboratory

Supervisor:

José Carlos Lopes, Associate Professor

Co-supervisor:

Vítor Jorge Pais Vilar, Assistant Researcher

Chemical Engineering Department

September 2013

“Le Genie Chimique c’est pas de la plomberie.”

Pierre Le Goff (1923-2005),

via Alíro E. Rodrigues [1]

Acknowledgements

I'm sincerely thankful to Professor José Carlos Lopes and to LSRE's Assistant Researcher Vítor Vilar for the judicious guidance, prompt availability and inexhaustible patience – along with their acute technical expertise they have been a role model for exertion, dedication and accomplishment.

To my colleagues at LSRE, I duly acknowledge their support and motivation while carrying this endeavour. We have had many discussions - technical and non-technical – which have steered along the tortuous path towards this end.

However, a special display of gratitude must go to Cláudio Fonte and Carlos Fonte, whose provision and unwavering patience – even when set apart or focused on own matters – have never failed me.

Also, a word of appreciation goes to the Associate Laboratory LSRE/LCM for, among much else, providing the facilities, the compulsory paraphernalia and all other means necessary to complete this dissertation. This recognition should be extended to FEUP's ChE Department staff and Faculty for setting high standards on research and education.

To Cláudia, I am truly grateful - and fortunate - for her undivided attention, incessant motivation and clear bearings whenever I'd felt strayed.

I must apologise to Leonor for any blemished devotion and drained stamina during the past few months - I'm truly sorry.

To my close family, I'm obliged for the nurturing environment and the ever earnest advices that I have, unassumingly, been offered all my life.

Thank you.

Intentionally left blank

Resumo

O trabalho apresentado centrou-se na caraterização de um reator para aplicação a processos fotocatalíticos, por intermédio de uma ferramenta de dinâmica de fluídos computacional (CFD), incluída no pacote ANSYS ®.

Para tal, foi conduzido um estudo alargado da hidrodinâmica do escoamento num tubo, por modulação de diversos parâmetros dimensionais e operacionais, tendo sido avaliada, monitorizada e, sempre que possível, validada a resposta do simulador àquelas condições. Para melhor captação do comportamento na região junto à parede, foi definida uma metodologia de geração de grelha com apuro suficiente de forma que o primeiro ponto se situe à distância desejada da parede. Esta metodologia mostrou-se adequada para as condições estudadas sem necessidade de estratégias adicionais de geração ou adaptação da grelha, ou recurso a estratagemas avançados de inicialização das condições fronteira.

A confiança nos modelos hidrodinâmicos usados na consistência da grelha gerada e na discretização definida abriu caminho para a caracterização do tubo como um reator, em termos de distribuição dos tempos de residência, e à posterior introdução de uma reação química simples, quer dando uso às capacidades da interface do utilizador, quer programando funções definidas pelo utilizador (UDF) no FLUENT ®.

O passo final consistiu na introdução de um campo de radiação que conduziu aos primeiros passos na integração da intensidade de radiação, calculada pelo modelo *Discrete Ordinates*, como fator determinante do processo fotocatalítico. Neste âmbito, as funções definidas pelo utilizador assumem um papel incontornável.

Os procedimentos adotados lançam as bases para um futuro aprofundamento dos modelos químicos, mecanismos de reação e radiação. Mostra-se necessária refinação adicional para melhor poder reproduzir-se o comportamento do processo, bem como de estudos experimentais complementares para suportar a correta implementação ou validação. No entanto, os resultados obtidos deixam boas indicações sobre a possibilidade de aplicação prática com enorme potencial de aproveitamento de recursos e tempo, para além do efeito sinérgico complementar aos esforços da componente fortemente experimental de alguns grupos de investigação do LSRE.

Palavras Chave (Tema): Simulação; Turbulência; CFD; Fotocatálise; Reação/Radiação;

Abstract

The present work has focused on the characterization of a reactor for photocatalytic processes by means of a computational fluid dynamics (CFD) tool included in the ANSYS® package.

For this purpose, a comprehensive study of the hydrodynamic flow in a tube was conducted through modulation of several dimensional and operational parameters. The results have been used to evaluate, monitor and, whenever possible, validate the simulator response to those conditions. To better capture the behaviour in the near wall region, a methodology was used for generating a grid with sufficient refinement so that the first point is equal to the desired wall distance. This practice was proven adequate for the conditions studied without the need for additional strategies to generate or adapt the grid, or use advanced initialization features for boundary conditions.

The gained confidence in the hydrodynamic models used, and the consistency of grid discretization, paved the way for the characterization of the tube as a reactor in terms of residence time distribution. Subsequently, a simple chemical reaction was introduced, either by giving use to capabilities of the graphical user interface of FLUENT, either by programming user defined functions (UDF) and attaching them to the case study.

The final step was the introduction of a radiation field that led to the first stages in integrating the radiation intensity, calculated by the Discrete Ordinates model, as a determinant part of the photocatalytic process. In this context, the user defined functions play a key role.

The procedures adopted lay the foundations for a future deepening of chemical reaction models, mechanisms and radiation. Further refining is still necessary to be able to completely reproduce the behaviour of the process, as well as experimental complementary studies to support the correct implementation or validation. However, the results provide a good insight regarding the practical applications, with huge potential for taking advantage of resource and time savings, in addition to the synergistic effect complementary to the efforts of some experimental intensive research groups at LSRE.

Keywords: Simulation; Turbulence; CFD; Photocatalysis; Reaction/Radiation;

DECLARAÇÃO

Declaro, sob compromisso de honra, que este trabalho é original e que todas as contribuições não originais foram devidamente referenciadas com identificação da fonte.

Nuno Gonçalo Pacheco Lourenço
Porto, 24 de outubro de 2013

Intentionally left blank

Index

List of Figures

List of Tables

Intentionally left blank

Nomenclature

Roman letters

$\hat{R}_{i,r}$	Molar rate of creation/destruction of species i in reaction r	
h_f	Head loss	m
k′	Rate constant independent of light intensity	$s^{-1}(Wm^{-2})^{-\alpha}$
A_r	Pre-exponential factor	s^{-1}
$C_{j,r}$	Molar concentration of each component j in reaction r	
D_i	Internal Diameter	m
E_r	Activation energy	kJ mol^{-1}
F_i	Flow rates (of i species)	kg s^{-1}
I_λ	Light intensity at a wavelength λ	W m^{-2}
$M_{w,i}$	Molecular weight of product species i	
N_A	Avogadro's number (6.023 x10^{23})	
N_r	Number of chemical species in reaction r	
Q_{UV}	Accumulated UV energy per volume	kJ L^{-1}
R_h	Hydraulic radius	m
R_i	Reaction term source for species i	
S_{ij}	Mean strain rate tensor	
$k_{f,r}$	Forward rate constant for reaction r	
$r_\parallel$	Amplitude of radiant energy parallel to the plane of incidence	
$r_\perp$	Amplitude of radiant energy perpendicular to the plane of incidence	
$\overline{t}$	Mean residence time, V/Q	s^{-1}
$v_{x,max}$	Maximum axial velocity	m s^{-1}
v_τ; v^*	Frictional Velocity	
y^+	Dimensionless distance from the wall	
$\gamma_{j,r}$	Third body efficiency of the j species in r reaction	
$\eta'_{j,r}$	Forward rate exponent	
$\eta''_{j,r}$	Backward rate exponent	
g	Gravity acceleration	m^2s^{-1}
g	Gravity acceleration	m s^{-2}
h	Planck's constant (6.6256x10^{-34})	J s $photon^{-1}$
K	Global kinetic constant	L kJ^{-1} (or s^{-1})
V	Volume	m^3
A	Area	m^2
$A(\lambda)$	Absorbance	
C	Concentration	mol m^{-3}
D; d	Diameter	m
E	Energy magnitude	J
$E(t)$	Exit age distribution	s^{-1}
$F(t)$	Non-dimensional breakthrough curve	
I	Radiation intensity OR incident radiation	W sr^{-1} OR Wm^{-2}
L	Length	m
P	Pressure	Pa
Q	Flow Rate	m^3 s^{-1}
R	Radius OR Universal gas constant OR Reflectance	m OR J mol^{-1} K^{-1}
Re	Reynolds number $\rho vD/\mu$	
T	Temperature	K

Roman letters

$T(\lambda)$,	Transmittance	
U	Mean velocity	m s^{-1}
a	Absorption coefficient	m^{-1}
c	Speed of light (2.9979 x10^8)	m s^{-1}
f	Friction factor	
k	Turbulent kinetic energy	m^2s^{-2}
n	refractive indices	
p	Pressure	Pa
r	Radial distance	m
t	time	s
$u;\ v$	Velocity	m s^{-1}
x	Space coordinate	
y	Distance from the wall	m
y	Space coordinate	
z	Space coordinate	

Greek symbols

$\Delta_{x,min}$	Minimum axial mesh dimension	m
Ω_{ij}	Mean rotation tensor	
β_r	Temperature exponent	
$\gamma_{j,r}$	Third body efficiency of the j species in r reaction	
δ_{ij}	Kronecker delta	
$\eta'_{j,r}$	Forward rate exponent	
$\eta''_{j,r}$	Backward rate exponent	
θ	incident angle/ refractive angle	rad.
σ^2	Variance	
σ_s	Scattering coefficient	m $^{-1}$
τ_{ij}	Reynolds stress tensor($-u'_iu'_j$)	
τ_w	Wall shear stress	
υ_t	Kinematic eddy viscosity	m^2 s^{-1}
Φ	phase function OR Quantum yield	
Ω	Solid angle	steradian, sr
γ	Specific Weight	N m^{-3}
ε	Turbulent dissipation	m^2 s^{-3}
$\varepsilon(\lambda)$	Molecular absorption coefficient	L $mole^{-1}$ cm^{-1}
λ	Radiation wavelength	m
μ	Molecular viscosity	Pa.s
ν	Kinematic molecular viscosity	m^2 s^{-1}
ρ	Density	Kg m^{-3}
σ	Stefan-Boltzmann constant (5.6697x10-8)	W m^{-2} K^{-4}
ω	Specific dissipation rate	s^{-1}
ϑ	Frequency (of radiation)	s^{-1}

Indexes

$\bullet$	Radical notation
$^{*};^{+}$	Dimensionless variable
x'	Fluctuation of variable x
i	Index or counter
i,j	Any direction
k	Index or counter
in	Inlet
out	Outlet
j	Index or counter
avg	Average
$\overrightarrow{\ }$	Vector

Acronym list

AOP	Advanced Oxidation Process
CFD	Computational Fluid Dynamics
CSTR	Continuous Stirred Tank Reactor
DO	Discrete Ordinates
DNS	Direct Numerical Simulation
EP	Emerging pollutant
FCT	Fundação para a Ciência e Tecnologia
LDA	Laser Doppler Anemometry
LES	Large Eddy Simulation
LSI	Line Source Integration
MPSS	Multiple Points Source Summation
MSSS	Multiple Segment Source Summation
PFR	Plug Flow Reactor
PIV	Particle Image Velocimetry
RAD-LSI	Radial Intensity Model + Line Source Integration
RANS	Reynolds Averaged Navier-Stokes
RTD	Residence Rime Distribution
2D	Two dimension
3D	Three Dimension
PFR	Plug flow Reactor
RAM	Random Access Memory
HDD	Hard Disk Drive
CPU	Central Processing Unit

Mathematical operations

$\frac{\partial}{\partial x}$	Partial derivative
lim	Limit
$\sum$	Sum operator
$\int$	Integral
$\prod$	Product operator

Intentionally left blank

1

INTRODUCTION

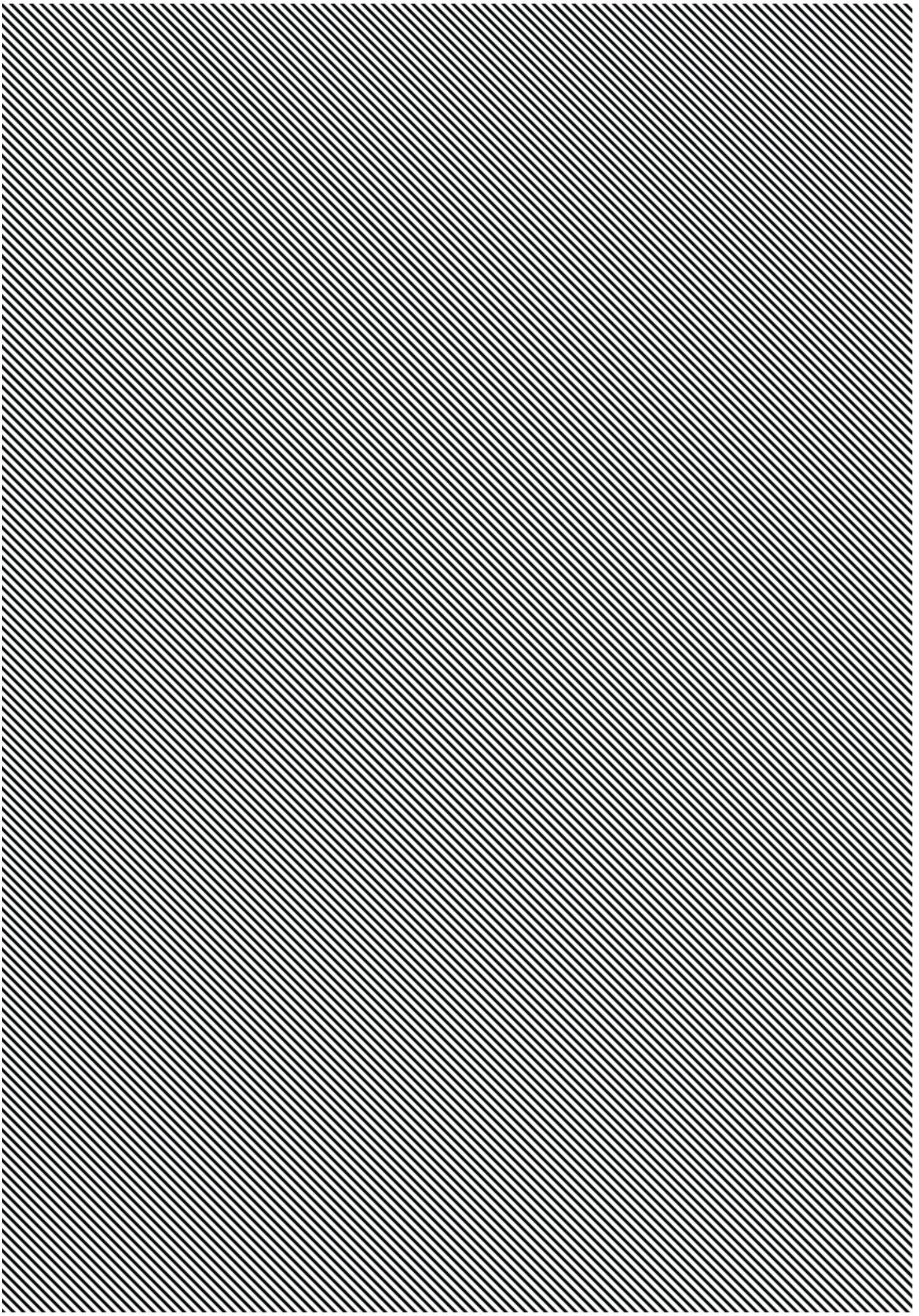

1 Introduction

1.1 Background and Relevance

The past couple of centuries have witnessed the advent of the industrial revolution, the exponential economic growth and the burst of population numbers that followed. These events have placed considerable strain upon earth's natural resources and on the environment. Pollution related to such activities has transformed and augmented accordingly over the past few decades, in such way that the standard traditional treatment methods, such as biological processes, are now deemed unsuitable for dealing with what are commonly called emerging pollutants (EPs) [2, 3]. More recently, Advanced Oxidation Processes (AOPs) have been successfully applied for the treatment of recalcitrant waters and effluents, whose characteristic composition would not allow the usage of traditional treatment techniques. The AOPs are based on the production of extremely reactive and unselective oxidants, such as hydroxyl radicals (HO•), which are clean, low-cost and can mineralize almost any organic compound, even bio-recalcitrant ones [4, 5].

First described in 1894, Fenton's reaction [6] is currently one of the most popular AOPs. The production of hydroxyl radicals can be depicted as:

$$Fe^{2+} + H_2O_2 \longrightarrow Fe^{3+} + OH^- + {}^{\bullet}OH \qquad (1)$$

$$Fe^{3+} + H_2O_2 \longrightarrow Fe^{2+} + HO_2^{\bullet} + H^+ \qquad (2)$$

In the homogeneous Fenton reaction, ferrous iron (Fe^{2+}) reacts with hydrogen peroxide (H_2O_2) leading to the production of one mole of ${}^{\bullet}OH$ per mole of H_2O_2 initially decomposed (Eq. (1)). The regeneration of ferric ions (Fe^{3+}) to ferrous ions (Fe^{2+}) occurs by Eq. (2), which is the rate limiting step in the catalytic iron cycle and thus limiting the efficiency of the process.

To overcome this limitation, Fenton's reaction efficiency can be enhanced by coupling UV/Vis radiation [7]. The main advantage of the UV/Vis radiation is that Fe^{2+} species can be regenerated from Fe^{3+} to Fe^{2+} by photochemical reactions (Eqs. (3) and (4)), including the photoreduction of Fe^{3+} and intermediate complexes dissociation, leading to the production of another mole of ${}^{\bullet}OH$ per mole of H_2O_2 initially decomposed, closing the catalytic cycle in combination with Eq. (1). Depending on the ligand, the Fe^{3+}complex can make use of UV and visible radiation of the solar spectrum up to 580 nm.

$$[Fe(OH)]^{2+} + h\upsilon \longrightarrow Fe^{2+} + {}^{\bullet}OH \qquad (3)$$

$$[Fe^{3+}L] + h\upsilon \longrightarrow Fe^{2+} + L^{\bullet} \qquad (4)$$

The oxidation/reduction reactions occur between the contaminants and the hydroxyl radicals repeatedly, while the organic pollutants are degraded sequentially into intermediate compounds and, ultimately, completely mineralized into CO_2, H_2O and mineral acids.

One of the obvious disadvantages of a homogeneous Fenton reaction is the presence of large quantities of dissolved iron after the treatment which must be kept below discharge limits. Other drawbacks are first, the necessary acidification of the solution to lower the pH values to avoid the precipitation of iron and second, its latter neutralization which, for high effluent volumes, might not be feasible. Indeed, these additional steps may involve costly additional processes.

Therefore, an efficient design or optimization of such photocatalytic systems must integrate both reactor engineering, such as hydrodynamics and space-time analysis (RTD), the technical constrains affecting UV distribution inside the reactor, usually limited by the geometry, materials and configuration/arrangement, and chemical reaction mechanisms and kinetic rate constants. This is clearly no easy task and is where computer aided simulations come into play to effectively assist such enterprise.

Computational Fluid Dynamics is a trending tool for numerically solving the equations of fluid dynamics over both space and time, including mass, momentum, and energy conservation. When combined with the appropriate boundary and initial conditions, these governing equations can accurately describe both the physical and chemical changes within a reactional system. In fact, the set of governing equations for momentum conservation, usually referred to as the Navier-Stokes equations, where deduced in the early Victorian period but, due to their complicated nature, wasn't until the birth of modern computing that it was prossible to take full advantage of their modelling capabilities.

Nonetheless, a numerical solution of the Navier–Stokes equations for turbulent flow is still extremely difficult to achieve, as the fine mesh necessary to capture all the different mixing-length scales resulting in turbulent flow would inter the computational time so significantly it becomes infeasible (at the time of writing), but also owing to its unsteady nature which fundamentally leads to divergence.

To overcome these limitations when modelling such flows, computational fluid dynamics packages resort to time-averaged equations, such as the Reynolds-averaged Navier–Stokes equations (RANS), as proposed per Reynolds in 1895 [8], supplemented with turbulence models.

The first approach for proposing a mathematical model of turbulent stresses aimed to replicate the events related to the molecular gradient-diffusion. In this line of thought, Boussinesq [9] introduced the concept of an eddy viscosity. The Boussinesq hypothesis is employed to bring closure, *i.e.*, providing a sufficient number of equations to solve all of the unknown variables, to many turbulence models, offering a relatively low cost computation for the turbulence viscosity v_t.

1.2 Objectives and Contents

This work aims at laying a base strategy for using CFD modelling to aid the design of photocatalytic processes. The project drive was:

- to understand the CFD package capabilities, the strategy towards the outcomes and to gain confidence on the results. One should always remember that even if a result is presented to the user this does not necessarily mean that it is the best solution or, in some cases, physically possible. Sufficient time and effort should be devoted to this goal.
- to select and assess a suitable turbulence model and subsequent hydrodynamics characterization of the fluid flow. The results will be either compared with experimental results or with theoretical approximations. Several operation conditions should be studied.
- to characterize the reactor in terms of space-time distribution. Results should account for operational parameters.
- to introduce a simple chemical reaction in FLUENT. Taking advantage of FLUENT's UDFs, a protocol for implementing chemical reaction should be used.
- by using one of the radiation models, an irradiation field must be obtained. Strategies for coupling with chemical reaction are to be developed and implemented.
- to obtain an integrated - yet simplified - approach, combining the hydrodynamics, chemical reaction and radiation.

A motivational introduction to the task at hand was already provided in this chapter, clearly stating the relevance and challenges of such endeavour.

A review of past developments and more recent studies on subjects related to this work will be described in Chapter 2.

The conceptual description, the methods, strategies and models used will be introduced in Chapter 3 and 4. Results obtained will also be presented and its validity scrutinized.

Chapter 5 comprises the conclusions, assessment of the above projected goals and proposals for consolidating this work as future development and further study.

1.3 About LSRE

The Associate Laboratory LSRE/LCM results of a partnership between LSRE, Laboratory of Separation and Reaction Engineering and LCM, Laboratory of Catalysis and Materials. The Associate Laboratory status was granted in December 2004 by FCT. The two research lines of the Associate Laboratory are:

1. New cyclic separation/reaction technologies for chemical and pharmaceutical industries; and,
2. Synthesis and formulation of high-added value products.

The mission of LSRE/LCM is to contribute to the National and European scientific and technological development in the areas of Separation and Reaction Processes in Chemical Engineering. LSRE's vision of Chemical Engineering involves contributions from Molecular, Materials, Process and Product Engineering (ChE = M2P2E), which is imprint in the arrangement of the research structure.

LSRE/LCM is assembled under the following clusters, conforming to the Research Groups I to IV from LSRE and the remaining from LCM:

I. Process Engineering;
II. Product Engineering;
III. Environmental Science and Engineering;
IV. Chemical Engineering Thermodynamics; and,
V. Catalysis and Materials.

LSRE pioneered in fluid dynamics research coupled with mixing, chemical reaction and reactor design, later resulting in a spin-off venture FLUIDINOVA (www.fluidinova.com), which still commercializes technologies first developed at LSRE along with a broad range of services to companies in this field of knowledge. Nonetheless, LSRE continues to closely collaborate with industrial partners and performs advanced research and training in these areas, as part of the efforts carried at the Product Engineering research group.

LSRE is hosted by the Faculty of Engineering of the University of Porto. The Associate Laboratory also comprises a pole located at Polytechnic Institute of Bragança and, more recently, a pole at Polytechnic Institute of Leiria. Some individual faculty staff of other private and public higher education institutions are also involved in LSRE's research activities.

Overall, LSRE regularly accounts for more than 150 collaborators, distributed by faculty and research staff, Post-doc researchers, PhD candidates and research fellows. Among these, over 65 members hold a PhD degree.

2

STATE OF THE ART

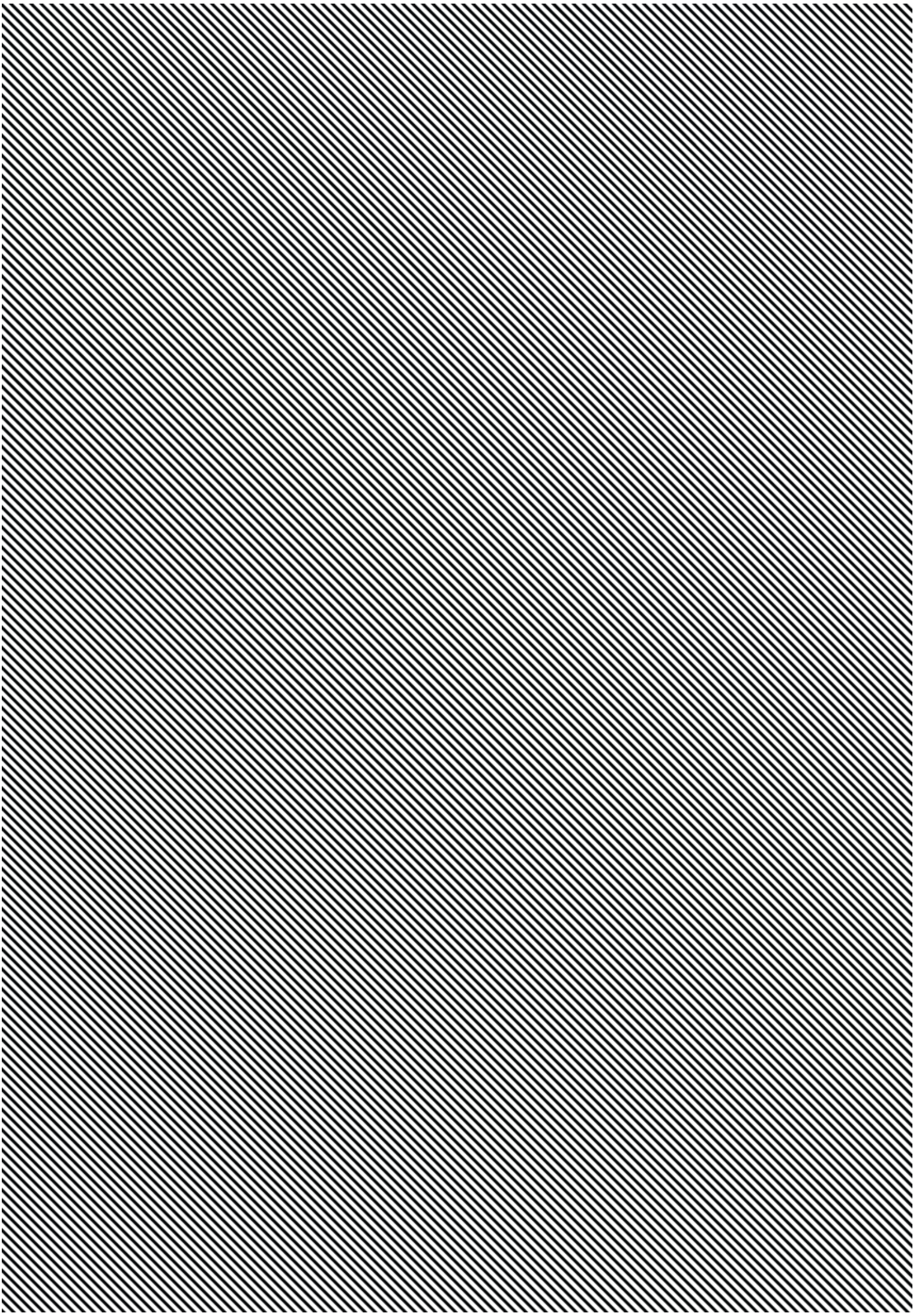

2 State of the art

The design of highly efficient photocatalytic processes for environmental applications place a series of challenges to meet the desired operational conditions, while keeping low functioning costs and observing regulatory requirements.

To effectively accomplish such goals, the case of study must be unfolded in several research fields intrinsic to the design. The process' hydrodynamics, chemical reaction and radiation must be thoroughly studied and modelled in order to achieve a unified system capable of answering to the desired design goals and provide for future scale-up. With the incorporation of radiation it is obvious that the design of such reactors presents additional difficulties when compared with the conventional catalytic systems.

Therefore, modelling a radiation source - and the corresponding field - is mandatory due to the key role on the initiation of the catalytic process. A wide variety of tools, such as Line Source Integration (LSI), Multiple Points Source Summation (MPSS), Multiple Segment Source Summation (MSSS), RAD-LSI, and Discrete Ordinates (DO) [10], are commonly used to solve the Radiative Transfer Equation (RTE) thus providing for a radiation field inside the reactor.

With the wide availability of computer power, CFD is rapidly becoming an invaluable engineering tool for predicting fluid flow, heat and mass transfer with chemical reaction coupling, by numerically solving the set equations that govern these phenomena using an algorithm. With such arguments, it is not surprising that (Chemical) Engineering Science is relying ever more increasingly on computational fluid dynamics to analyse the performance of unit operation. CFD allows for an in-depth analysis of the fluid mechanics and local effects in these types of equipment. With the correct approach, this may result in gain on performance, reliability and productivity or allowing for dependable scale-up. Moreover, CFD simulations may provide relevant data that might assist conceptual studies, troubleshooting or redesign.

As in most industrial streams, UV photoreactors are expected to operate in conditions that would result in turbulent flow regime. Therefore, CFD simulations of such process must account for the impact of turbulent mixing on any chemical reactions that occur within the photoreactors.

Virtually no prior studies combining solar UV radiation initiated photocatalytic processes have been modelled with CFD packages. That said, over the past few decades, there has been a growing interest in UV reactor design, operation and modelling aided by CFD. Successful applications to inactivation of biohazard agents [11-14] or for the elimination of chemical pollutants [15, 16] in reactors with a discrete light source have been carried with promising results.

2.1 Computational Fluid Dynamics

As stated before, the equations of fluid dynamics include the mass, momentum and energy conservation balances. For an incompressible fluid, the continuity equation, *i.e.*, the equation for mass conservation, can be written as:

$$\frac{\partial u_x}{\partial x} + \frac{\partial u_y}{\partial y} + \frac{\partial u_z}{\partial z} = 0 \qquad (5)$$

where u_x, u_y and u_z correspond to the velocity components on x, y and z flow direction, respectively. For turbulent incompressible flow and disregarding the gravity term, the Reynolds-averaged Navier-Stokes equation may be expressed as:

$$\rho \frac{\partial U_i}{\partial t} + \rho U_j \frac{\partial U_i}{\partial x_j} = -\frac{\partial P}{\partial x_i} + \frac{\partial}{\partial x_j}(2\mu S_{ij} + \rho \tau_{ij}) \qquad (6)$$

In equation (6), ρ is the fluid density, U_i is the mean velocity, t is time, P is the static pressure, μ is the molecular viscosity and S_{ij} is a stress rate tensor:

$$S_{ij} = \frac{1}{2}\left(\frac{\partial U_i}{\partial x_i} + \frac{\partial U_j}{\partial x_j}\right) \qquad (7)$$

and the Reynolds stress tensor is $\tau_{ij} = \tau_{ji} = -\rho\overline{u_i' u_j'}$.

From left to right, in eq. (6), the first term represents the local acceleration, the second term corresponds to the non-linear convective acceleration, the third term denotes the pressure gradients and the last term represents viscous forces and the derivatives of the Reynolds stresses.

Time averaging is achieved by:

$$F(x) = \lim_{T\to\infty} \frac{1}{T} \int_t^{t+T} f(x_i, t)dt \qquad (8)$$

and the instantaneous field is defined by the sum of the mean and fluctuating component, such as for pressure or velocity:

$$p = P + p' \qquad u_i = U_i + u_i' \qquad (9)$$

The equation for species transport accounting for turbulent convective-diffusion is given by [17]:

$$\frac{\partial C_i}{\partial t} + U_j \frac{\partial C_i}{\partial x_j} = \frac{\partial}{\partial x_j}\left((D + Dt)\frac{\partial C_i}{\partial x_j}\right) + R_i + S_i \qquad (10)$$

where C_i is the average concentration of species i, U is the mean velocity, S_i account for custom sources (e.g., defined by UDF), R_i is the source corresponding to the reaction term for species i, and D denotes the molecular diffusivity coefficient and D_T represents the turbulent diffusivity that may be defined as:

$$D_T = \frac{\nu_T}{Sc_T} \tag{11}$$

Given that ν_T is the turbulent eddy viscosity and Sc_T is the turbulent Schmidt number. Hence, the $D_T \frac{\partial c_i}{\partial x_j}$ term in eq. (10) accounts for the turbulent fluctuations effects on the concentration and velocity.

2.2 Turbulence Modelling

As mentioned earlier and from the practical engineering standpoint, virtually all flows found on industrial processes and unit operations are turbulent.

At increasingly higher Reynolds numbers the viscous stresses are overcome by the fluid's inertia and laminar motion becomes unstable, resulting in turbulent motion. This involves quick pressure and velocity fluctuations and, as it is three dimensional and unsteady, it is inherently complex.

As no single turbulence model is unanimously accepted as being capable of tackling all types of flow conditions, the selection of a turbulence model will heavily depend on considerations as, for instance, the flow characteristics, the desired accuracy, but also the access to computational resources, the time cost for the simulation and the previous experience on a specific problem.

Typically, Reynolds Averaged Navier-Stokes (RANS) Turbulence Models offer the most cost-effective strategy for modelling the turbulent flows usually found in industrial processes and equipment. Two examples of these models are the k-ε or the k-ω, which may be presented with a few other modifications. These models simplify the problem to the solution of two additional transport equations and introduce an Eddy-Viscosity, or turbulent viscosity, to compute the Reynolds Stresses. RANS models are suitable for many engineering applications and usually provide the level of accuracy required [18].

A comparison regarding turbulence model complexity – and computational cost – is schematically provided in Figure 2.1. As in many other process methodologies, it is expected that engineers are capable of obtaining the best possible result at minimum cost (time, money, feedstock, etc.), hence the paramount importance of model selection.

Most of the problems with the two-equation approach can be dealt with the Boussinesq hypothesis, which relates the Reynolds stress tensor to the mean strain rate tensor by means of an eddy viscosity [20]. While models based on such approximation provide reasonable predictions for many engineering applications, there are some issues for predicted flow properties which contrast greatly from corresponding measurements. This includes flows with abrupt changes in mean strain rate, flows over curved surfaces, as well as flows in ducts with secondary motions [20]. For these types of flows, the eddy-viscosity concept may be too simplistic and, as

such, may not describe the complex strain rate field, in which the key role of non-isotropic turbulent characteristics is very important.

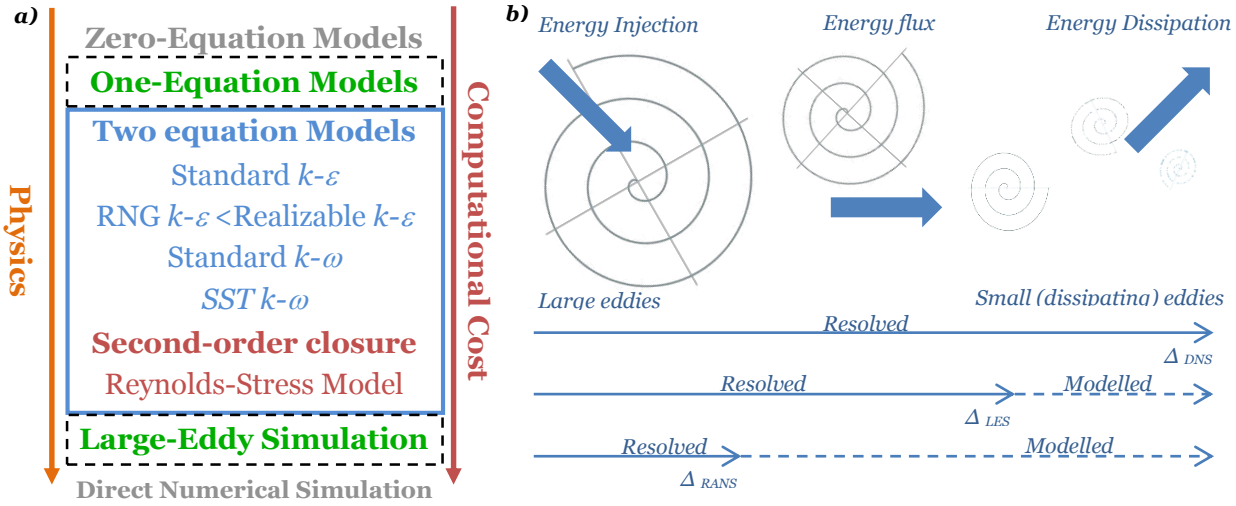

Figure 2.1 – a) turbulent model cumulative complexity and computational cost; b) model approach to predict all flow scales. Adapted from [19]

In order to test the sensitivity to turbulent models, previous studies [21] have shown that $k-\varepsilon$ and the $k-\omega$ provide reasonable prediction of the fluid flow characteristics. As expected, better reproduction of the turbulent phenomena can be achieved resorting to more computational intensive methods.

The same study suggests that the fluence rate is sensible to the selected turbulence model, mainly due to differences on model reproduction when predicting the far wake turbulent region.

The standard $k-\omega$ model implemented in FLUENT incorporates modifications for low-Reynolds number effects, compressibility, and shear flow spreading introduced by Wilcox [20]. The $k-\omega$ model has been adapted over the years where production terms have been added to both the k and ω equations. One of the drawbacks of this model is the sensitivity of the solutions to values for k and ω outside the shear layer. Though the new implementations have reduced this effect, it can still have a significant impact on the solution, in particular for free shear flows [18]. The turbulence kinetic energy is modelled by [20]:

$$\rho\frac{\partial k}{\partial t}+\rho U_j\frac{\partial k}{\partial x_j}=\tau_{ij}\frac{\partial U_i}{\partial x_j}+\frac{\partial}{\partial x_j}\left[(\mu+\sigma^*\mu_t)\frac{\partial k}{\partial x_j}\right]-\beta^*\rho k\omega \qquad (12)$$

as the specific dissipation rate is given by:

$$\rho\frac{\partial \omega}{\partial t}+\rho U_j\frac{\partial \omega}{\partial x_j}=\alpha\frac{\omega}{k}\tau_{ij}\frac{\partial U_i}{\partial x_j}+\frac{\partial}{\partial x_j}\left[(\mu+\sigma\mu_t)\frac{\partial \omega}{\partial x_j}\right]-\beta\rho\omega^2 \qquad (13)$$

and the eddy viscosity is defined as:

$$\mu_t = \rho \frac{k}{\omega} \tag{14}$$

where the Reynolds stress tensor is given by:

$$\tau_{ij} = 2\mu_t S_{ij} - \frac{2}{3}\rho k \delta_{ij} \tag{15}$$

with the empirical revised closure coefficients and auxiliary relations:

$\beta^* = \beta_0^* f_{\beta^*}$, $\sigma = 1/2$, $\sigma^* = 1/2$, $\alpha = 13/25$, $\beta = \beta_0 f_\beta$, $\beta_0^* = 9/100$, $f_{\beta^*} = \begin{cases} 1, & \chi_k \leq 0 \\ \frac{1+680\chi_k^2}{1+400\chi_k^2}, & \chi_k > 0 \end{cases}$, $\chi_k \equiv \frac{1}{\omega^3}\frac{\partial k}{\partial x_j}\frac{\partial \omega}{\partial x_j}$, $\beta_0 = 9/125$, $f_\beta = \frac{1+70\chi_\omega}{1+80\chi_\omega}$, $\chi_\omega = \left|\frac{\Omega_{ij}\Omega_{jk}S_{ki}}{(\beta_0^*\omega)^3}\right|$, $\Omega_{ij} = \frac{1}{2}\left(\frac{\partial U_i}{\partial x_i} - \frac{\partial U_j}{\partial x_j}\right)$, $\varepsilon = \beta^*\omega k$ and $l = \frac{k^{\frac{1}{2}}}{\omega}$

2.3 Reaction in FLUENT

Modelling mixing and transport of chemical species is done by solving conservation equations describing convection, diffusion, and reaction sources for each component (eq. (7)). FLUENT allows for multiple simultaneous chemical reactions, with reactions occurring in the bulk phase combined, or not, with reaction occurring at the walls or particle surfaces, and also in a porous region [18]. The reaction term in eq. (10) can be expressed as:

$$R_i = M_{w,i} \sum_{r=1}^{N_r} \hat{R}_{i,r} \tag{16}$$

where $M_{w,i}$ is the molecular weight of product species i and $\hat{R}_{i,r}$ is the molar rate of creation/destruction of species i in reaction r that is given by:

$$\hat{R}_{i,r} = \Gamma\left(\nu''_{i,r} - \nu'_{i,r}\right)\left(k_{f,r}\prod_{j=1}^{N_r}\left[C_{j,r}\right]^{\eta'_{j,r}} - k_{b,r}\prod_{j=1}^{Nr}\left[C_{j,r}\right]^{\eta''_{j,r}}\right) \tag{17}$$

and, N_r is the number of chemical species in reaction r, $C_{j,r}$ corresponds to the molar concentration of each component j in reaction r, $\eta'_{j,r}$ denotes the forward rate exponent while $\eta''_{j,r}$ represents the same for the backward reaction. The effect of third bodies (*e.g.*, catalysts) is depicted by:

$$\Gamma = \sum_{j}^{N_r} \gamma_{j,r} C_j \tag{18}$$

where, $\gamma_{j,r}$ corresponds to the efficiency of the j species in r reaction, with respect to the third body. The forward rate constant for reaction r, $k_{f,r}$ is obtained using an expanded version of the Arrhenius expression:

$$k_{f,r} = A_r T^{\beta_r} e^{-\frac{E_r}{RT}} \quad (19)$$

In eq. (19) A_r is a pre-exponential factor, E_r is the activation energy, while R corresponds to the universal gas constant, T to the temperature and β_r to a temperature exponent. The backward rate constant for reaction r, $k_{b,r}$ can be easily computed using the equilibrium constant.

The modelling depicted above was based on the approach of previous studies [22, 23], where the turbulent mixing in an agitated tank with competitive chemical reactions was simulated through CFD. The researchers found that this type of mixing model accurately foretold the mixture time and distribution for the product species.

2.4 Radiation

2.4.1 Photochemistry and Optics Primer

UV Photocatalysis can be described as the crucial process were a chemical reaction, or a set of chemical reactions, is initiated or driven by the absorption of ultraviolet radiation by the catalyst. This mechanism clearly depends on the energy of the UV radiation incident on the reacting molecule/catalyst surface/photoactive species. The magnitude of energy, E, within a photon of UV radiation is described by Planck's equation:

$$E = h\vartheta = h\frac{c}{\lambda} \quad (20)$$

where, h is the Planck's constant, c is the speed of light, λ denotes the wavelength of radiation and ϑ corresponds to the radiation's frequency.

Multiplying the energy per photon as calculated in eq. (20) by the Avogadro number results in energy per einstein, where by definition an einstein is one mole of photons. The quantum yield, Φ, which represents the moles of a given species photochemically transformed per mole of photons (einstein) absorbed [24], can be used to access the effectiveness of a photochemical process.

The molar absorption coefficient, $\varepsilon(\lambda)$, expresses the ability of a molecule to absorb light in a given solvent, and the efficiency of such light absorption at a wavelength λ by an absorbing medium is given by the absorbance, $A(\lambda)$, or the transmittance, $T(\lambda)$, defined by:

$$A(\lambda) = log\frac{I_\lambda}{I_{\lambda,0}} = \log T(\lambda) \quad (21)$$

where, $I_{\lambda,0}$ and I_λ are the light intensities of the beams entering and leaving the absorbing medium, at wave length λ, respectively. Typically, the absorbance of a medium follows the Beer-Lambert's Law:

$$A(\lambda) = \varepsilon(\lambda)Cl \quad (22)$$

given that, C is the concentration of absorbing species and l is the light path length.

It is also important to remember that the absorbance follows the additive property. Thus if there are multiple absorbing species in the solution, absorbance is then obtained by:

$$A = \sum_i \varepsilon_i C_i l \tag{23}$$

As in any photocatalytic water treatment system the UV light travels through multiple media (*i.e.*, air, quartz, and water) and thus the laws of optics should be accounted for. Refraction describes the change in direction of a wave as it passes through media with different refractive indices. This effect is described by Snell's law:

$$n_1 \sin\theta_1 = n_2 \sin\theta_2 \tag{24}$$

which relates the incident angle θ_1, the refractive angle θ_2, and the refractive indices $n_1$and n_2, as shown in Figure 2.2(a). In the same figure, it is also shown that a portion of the incident wave is reflected from the interface formed between the two media which, for un-polarized light, the reflectance R is defined by the Fresnel Laws:

$$R = \frac{1}{2}\left(r_{\parallel}^2 + r_{\perp}^2\right) \tag{25}$$

where $r_{\parallel}$ and $r_{\perp}$ are the amplitude of radiant energy parallel and perpendicular to the plane of incidence, respectively, given by:

$$r_{\parallel} = \frac{n_2\cos\theta_1 - n_1\cos\theta_2}{n_1\cos\theta_2 + n_2\cos\theta_1} \quad AND \quad r_{\perp} = \frac{n_1\cos\theta_1 - n_2\cos\theta_2}{n_1\cos\theta_1 + n_2\cos\theta_2} \tag{26}$$

2.4.2 Radiation Modelling

Discrete Ordinates (DO) is one of many methods for solving the radiative transfer equation that accounts for absorption and scattering effects when radiation passes through a homogeneous and isotropic medium.

Despite the widespread and popularity of other radiation models and techniques [10, 15, 16, 25], the DO Model was chosen, since it is already integrated in FLUENT and promptly available to implementation without further programming. Moreover, the simulation of a solar radiation (load) poses a number of challenges that UV lamp approach could not as easily cope with, namely the absence of a discrete light source. Since FLUENT also incorporates a Solar Load Model option capable of simulating several operational conditions which, given the case in study, presented as an option worth exploring. Furthermore, previous studies have shown good prediction of UV reactor performance when a DO model was used to simulate the fluence rate field [26, 27]. Given these considerations, the DO model seemed the natural choice for the radiation simulation.

As for the other conservative equations, the RTE is solved for a discrete number of solid angles, each associated with a vector direction $\vec{s}$:

$$\frac{\partial I(\vec{r},\vec{s})}{\partial s} + (a+\sigma_s) I(\vec{r},\vec{s}) = an^2 \frac{\sigma T^4}{\pi} + \frac{\sigma_s}{4\pi} \int_0^{4\pi} I(\vec{r},\vec{s}\,') \Phi(\vec{s}\cdot\vec{s}\,') d\Omega' \qquad (27)$$

where $\vec{r}$ is a position vector, $\vec{s}'$ denotes a scattering direction vector, s represents the path length, a is the absorption coefficient, n refers to the refractive index, σ_s denotes the scattering coefficient, σ corresponds to the Stefan-Boltzmann constant, I is the radiation intensity, T is the temperature, Φ a phase function and Ω is the solid angle. Note that, $(a+\sigma_s) I(\vec{r},\vec{s})$ illustrates the optical thickness or opacity of the medium and accounts for absorption and scattering. The next term denotes the importance of the refractive index n when considering radiation in semi-transparent media and accounts for emission. The last term, will account for the scattering effects.

Figure 2.2(b) illustrates the process of radiative transfer. While it should be clear the importance of the radiation field accounting for the participation of several radiative terms, looking at this scheme, the question regarding how it impacts the quantum yield may also arise. While the global yield may be intrinsic to the nature of each process, one may define the initial process of activation, or primary event, as the initial absorption and the immediate events that follow, disregarding any subsequent secondary actions [24]. For these and for single photons absorption processes, the rate of the primary step is intimately related to the rate of the energy absorbed. Together with the radiation field, this is of utmost importance to understand and analyse the process efficiency and its eventual improvement. The quantum yield for the catalyst (Fe) is well understood and extensively studied [28].

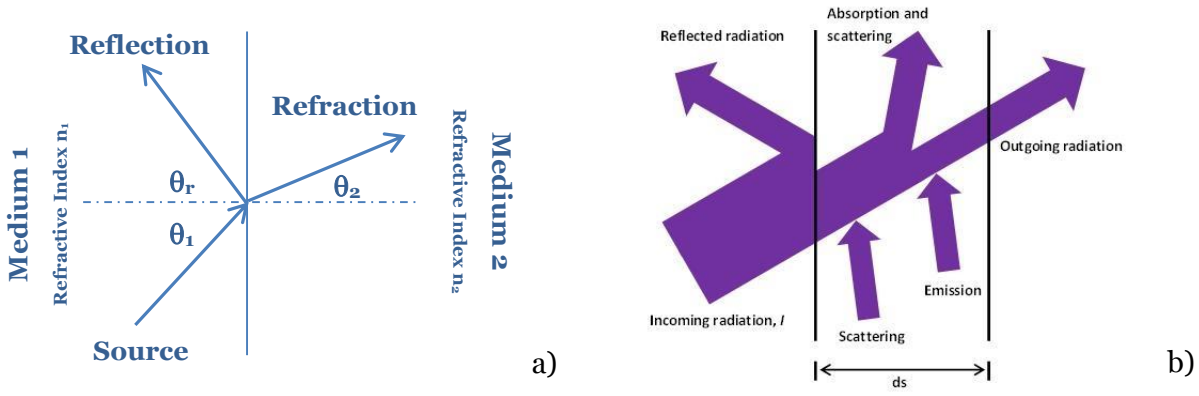

Figure 2.2 – a)Wave interface between two media; b) Radiative transfer schematic

Currently, from the selection of radiation models embedded in FLUENT, DO is the only model that works across the full range of conditions while accounting for scattering, absorption particulate effects (gas and solid), keeping accuracy in a wide variety of medium with moderate computational costs for the typical angular discretization [18].

3

MATERIALS AND METHODS

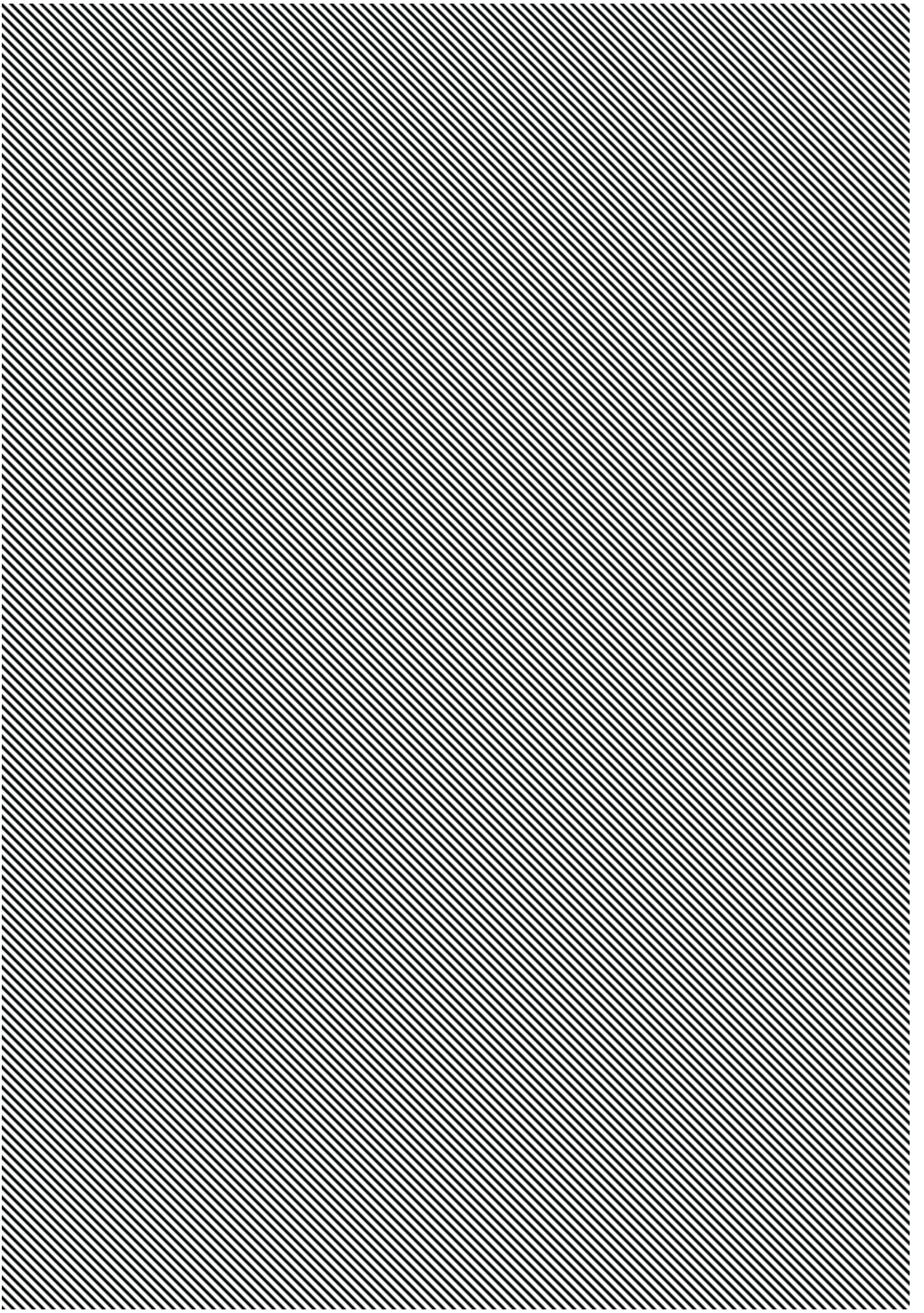

3 Materials and Methods

3.1 Experimental Setup

The experimental setup to obtain the global kinetic parameter is described below. The pilot plant can be seen in Figure 3.1. The autonomous unit is comprised of Compound Parabolic Collectors (CPCs), a recirculating pump, an UV Radiometer and a control unit. With the installed photovoltaic system it can be operated off the grid in remote locations.

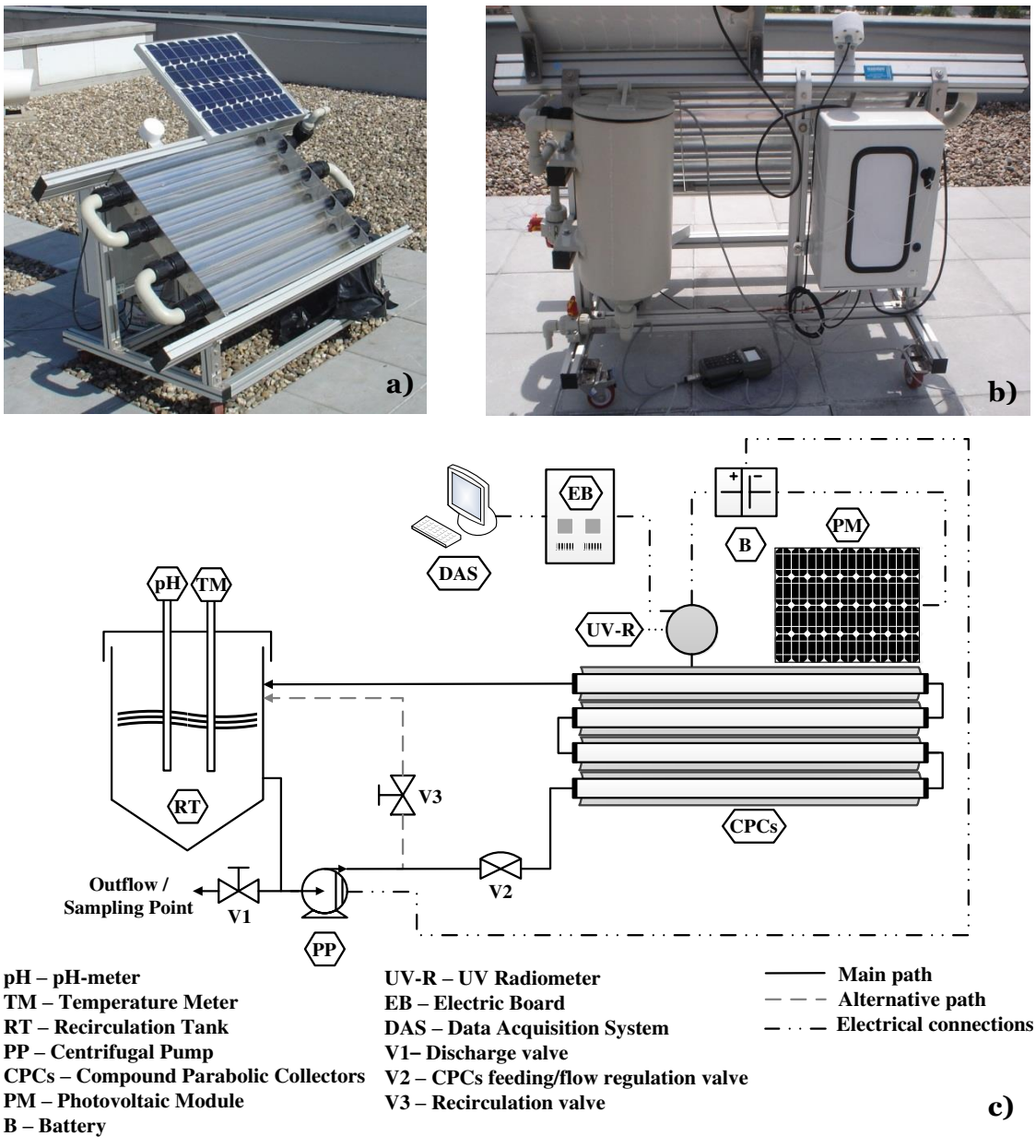

Figure 3.1 - Autonomous pilot plant with CPCs: a), b) – front and back pictures; c) operational diagram

Experiments were performed using sulfamethoxazole (SMX), $C_{10}H_{11}N_3O_3S$ (>95%), a recalcitrant antibiotic, hydrogen peroxide, H_2O_2 (50% (w/v), 1.10 g cm^{-3}) as oxidizing agent, iron sulfate

heptahydrated, $FeSO_4.7H_2O$, as catalyst, and sulfuric acid, H_2SO_4 (96%, 1.84 g cm^{-3}) for pH adjustment. SMX is expected to be mineralized according to:

$$C_{10}H_{11}N_3O_3S + 33H_2O_2 \longrightarrow 10CO_2 + 36H_2O + H_2SO_4 + 3HNO_3 \quad (28)$$

while the concentration decay can be adjusted to a pseudo-first-order reaction, according to:

$$r = -\frac{dC}{dQ_{UV}} = kC \quad (29)$$

where r is reaction rate, Q_{UV} is accumulated UV energy per volume, k is the kinetic constant and C is the instantaneous SMX concentration.

The operational and dimensional parameters are listed in table Table 3.1, while Table 3.2 lists the obtained kinetic parameters for SMX degradation under the described conditions.

Table 3.1 – operational and dimensional conditions for SMX degradation

Pilot unit		
Reactor Volume	21	L
Illuminated Area	0.63	m²
Flow rate	1200	L/h
Number CPCs	4	
Tube		
Diameter	D_e=0.05; D_i=0.0464	m
Length (irradiated)	1 (or 1.5)	m
Material	Borosilicate (Schott-Duran type 3.3, cut-off at 280 nm)	
Effluent		
[SMX]	20	mg/L
[H_2O_2]	in excess	
[Catalyst]	< discharge limit	
pH	2.8	
Density	1000	Kg/m³
Viscosity	0.001	Pa s

Table 3.2 - Pseudo-first-order kinetic parameters for SMX concentration decay

Experiment	C_0 (mg/L)	k (L/kJ)	r_0 (mg/kJ)	R^2	S_{R^2} (mg²/L²)
$Fe^{2+}/H_2O_2/UV/$; pH = 2.8	19.4	9 ± 2	175 ± 39	0.999	4.9×10^{-2}

By taking in to account the total reactor volume, the irradiated area and the mean radiation power the presented kinetic constant can be converted to time dependency, s^{-1}, for implementation in FLUENT.

3.2 Simulation Environment

The simulations were carried out mainly in the first system described in *Table 3.3* and, for testing and assessing purposes, the grid computing cluster was also used.

Table 3.3 – Available simulation environment

Machine	*CPU*	*RAM*	*HDD*	*OS*	*CFD*
DELL Precision T7500 Workstation	Dual Intel XENON E5620@2.4GHz (8 cores total)	24 GB	500 GB	Windows 7 Enterprise, SP1, 64-bit	ANSYS v.14.5
GRID@FEUP AVALANCHE Cluster	29 nodes / 16 cores per node, connected via a 40Gbps InfiniBand network	64GB to 128GB per node	500GB (local) 10TB (central)	Scientific Linux operating system, v.6	

The software operated was included in ANSYS package, version 14.5. The tools used were:

- DESIGN MODELLER, for 2D/3D case modelling;
- MESHING tool, for mesh generation and refinement;
- FLUENT, for fluid dynamics simulations; and
- WORKBENCH, for integrating all the above and setting up the simulation, thus providing for parametric studies.

This integrated environment, further than the added convenience, offers great flexibility, excellent documentation and a relaxed learning curve while providing for promptness and confidence in the results.

3.3 Mesh Generation and Control

To simulate tubular flow, an axis symmetrical planar (2D) strategy was adopted. This is a simplistic approach, assuming that the flow will not be greatly affected by swirling and rotational fluid motion. The plane used is better understood by looking at Figure 3.2. It should be noted that only the green section will be simulated and that the 3-dimensional arrangement is presented solely for clarity.

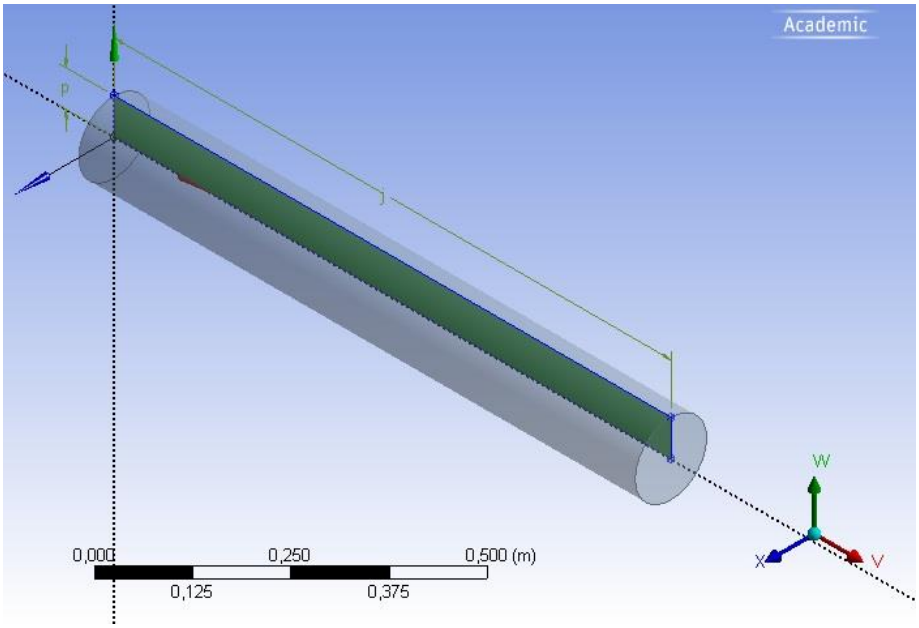

Figure 3.2 – DESIGN MODELLER Drawing depicting 2D section overlay on 3D pipe.

Having selected a two dimensional analysis setup, a strategy for computing the dimensionless wall distance, y^+, was adopted [19] to assist selecting the most suitable near-wall treatment (wall functions or near-wall modelling) and the corresponding turbulence model based on desired wall y^+. Nonetheless, other approximations were used to estimate skin friction, namely the Darcy-Weisbach eq. (31).

Frictional head losses are dissipated due to shear stress on the pipe walls. The general equation for head loss due to friction is given by:

$$h_f = C_f \frac{L}{R_h} \frac{v^2}{2g} \tag{30}$$

where $R_h = D/4$, $C_f = f/4$, which results in the common form of Darcy-Weisbach equation:

$$h_f = f \frac{L}{D} \frac{v^2}{2g} \tag{31}$$

At steady-state, uniform flow in a pipe the momentum flux is zero and pressure distribution across pipe is hydrostatic, equilibrium exists between pressure, gravity and shear forces, which mean we can relate the head loss due to wall shear stress [29]:

$$h_f = \frac{\tau_w L}{\gamma R_h} \tag{32}$$

where h_f corresponds to the head loss in length L, τ_w defines the wall shear stress, γ is the fluid specific weight and R_h is the hydraulic radius (D/4, for circular pipes). Combining eq. (31) and eq. (32), results in:

$$\frac{\tau_w L}{\gamma R_h} = f\frac{L}{D}\frac{v^2}{2g} \qquad or \qquad \tau_w = \frac{f}{8}\rho v^2 \tag{33}$$

The Darcy–Weisbach friction factor f can be obtained through the Goudar-Sonnad equation [30]. This is an approximation of the implicit Colebrook–White equation, and it is deemed the most accurate calculation to solve that equation directly for flow in a circular pipe:

$$\frac{1}{\sqrt{f}} = a\left[ln\left(\frac{d}{q}\right) + D_{CFA}\right] \tag{34}$$

where:

$D_{CFA} = D_{LA}\left(1 + \frac{z/2}{(g+1)^2+(z/3)(2g-1)}\right)$, a=2/ln(10), b=$(\varepsilon/D)/3.7$, d=$(ln(10)Re)/5.02$, s=$bd+ln(d)$, q=$s^{s/(s+1)}$, g=$bd+lnd/q$, z=$ln(q/g)$ and D_{LA}=$z(g/(g+1))$.

The dimensionless wall distance y^+ is defined by:

$$y^+ \equiv \frac{u_* y}{\nu} \tag{35}$$

Here, the kinematic viscosity is given by $\nu \equiv \frac{\mu}{\rho}$, and the turbulent velocity u_* corresponds to:

$$u_* = \sqrt{\frac{\tau_w}{\rho}} \tag{36}$$

Therefore, in order to obtain the first mesh centroid distance to the wall, which corresponds to the desired dimensionless wall distance of $y^+ = 1$, substituting in eq. (35) results:

$$y = \frac{\mu}{u_* \rho} \tag{37}$$

On the other hand, to fully outline the mesh grid, the number of mesh intervals of all edges must be controlled. First, the number of edge divisions for inlet/outlet was defined by:

$$n = int\left(\frac{log\left\{1 + \frac{i-1}{y}\frac{D}{2}\right\}}{log(i)}\right) \tag{38}$$

where i is a control parameter from ANSYS DESIGN MODELER/WORKBENCH denoted as inflation (or *growth ratio*), and D corresponds to the diameter. The *Bias factor*, also an ANSYS DESIGN MODELLER/WORKBENCH control feature, is defined by the ratio between the biggest and the smallest edge size division. Thus, this can be obtained by:

$$Bias\ factor = \frac{y \times i_1 \times i_2 \times i_3 \times \ldots i_n}{y} \quad \text{or} \quad bias\ factor = i^n \tag{39}$$

Secondly, the other two edges – pipe wall and symmetry axis – were defined using a high integer for the number of divisions, typically ≥ 1000.

This strategy was implemented in WORKBENCH to obtain the desired mesh to support the parametric studies that followed. The mesh was obtained using a mapped 2D surface defined by the number of edge divisions at inlet and outlet, consistent with the design point of y^+=1, and likewise for the wall. The result can be seen in Figure 3.3.

Following this procedure the mesh obtained is consistently of good quality and thus considered appropriate for the case at hand.

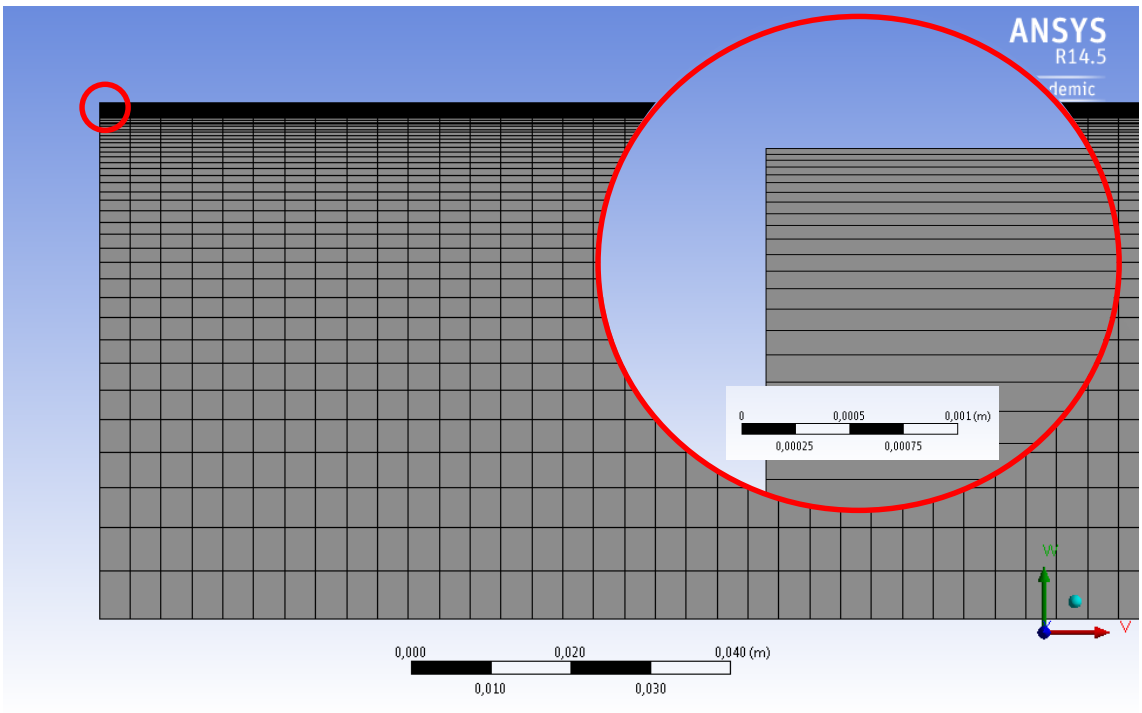

Figure 3.3 – Mesh used for 2D axisymmetric flow simulation.

3.4 Simulation Workflow

Following and implementing the procedure outlined above in ANSYS WORKBENCH, and by providing a minimum of input parameters, will allow for the definition of many design features such as the geometry of the 2D model, the desired mesh features and key FLUENT configuration constrains. Nonetheless, many of FLUENT's initial configuration has to be done in the program itself. The simulation steps can be better understood by looking at the schematic shown in Figure 3.4 which, in turn, corresponds to the WORKBENCH environment shown in Figure 3.5.

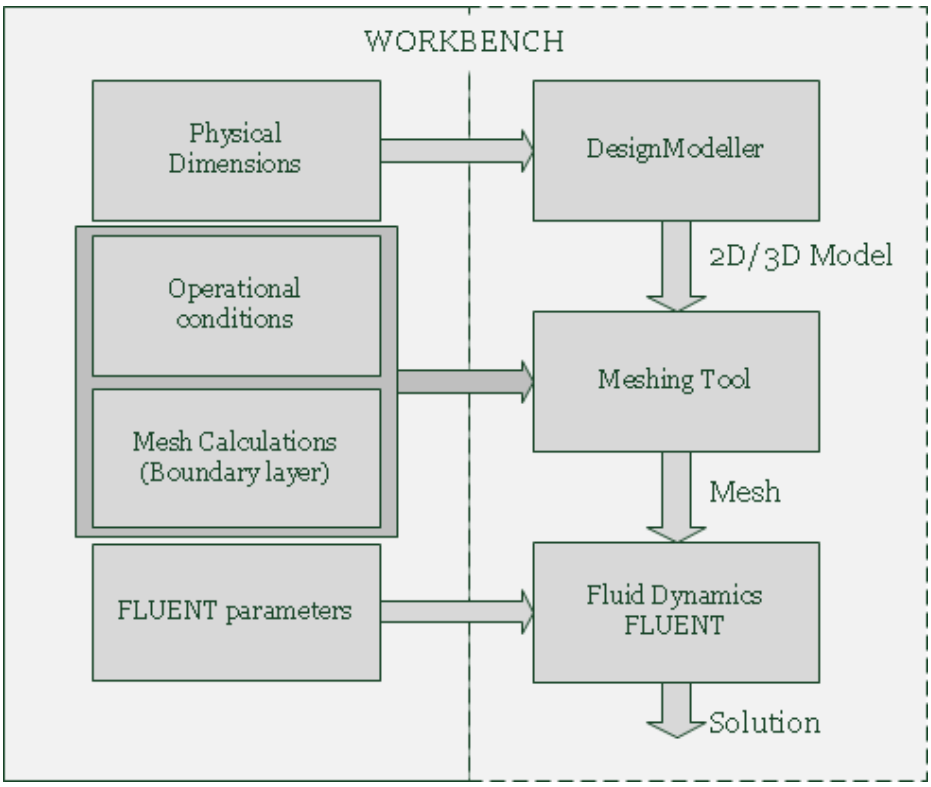

Figure 3.4 – ANSYS WORKBENCH workflow

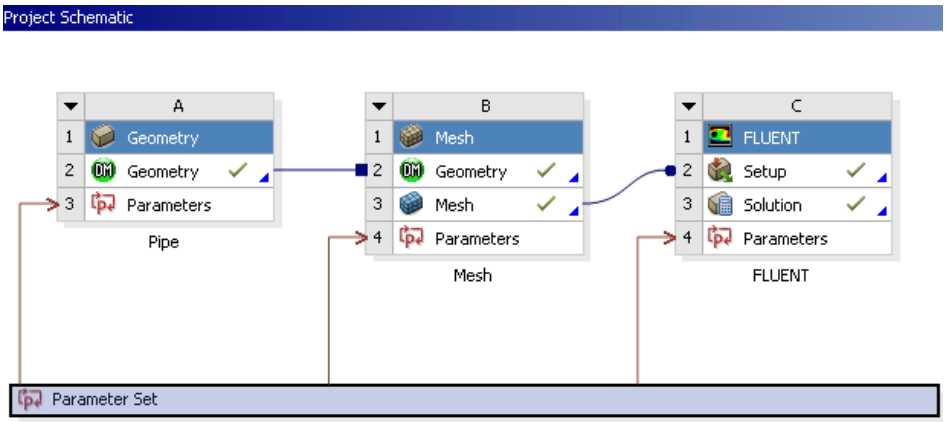

Figure 3.5 – Project schematic as seen inside ANSYS Workbench

Further information regarding WORKBENCH environment can be found in Appendix A.

Intentionally left blank

4

RESULTS AND DISCUSSION

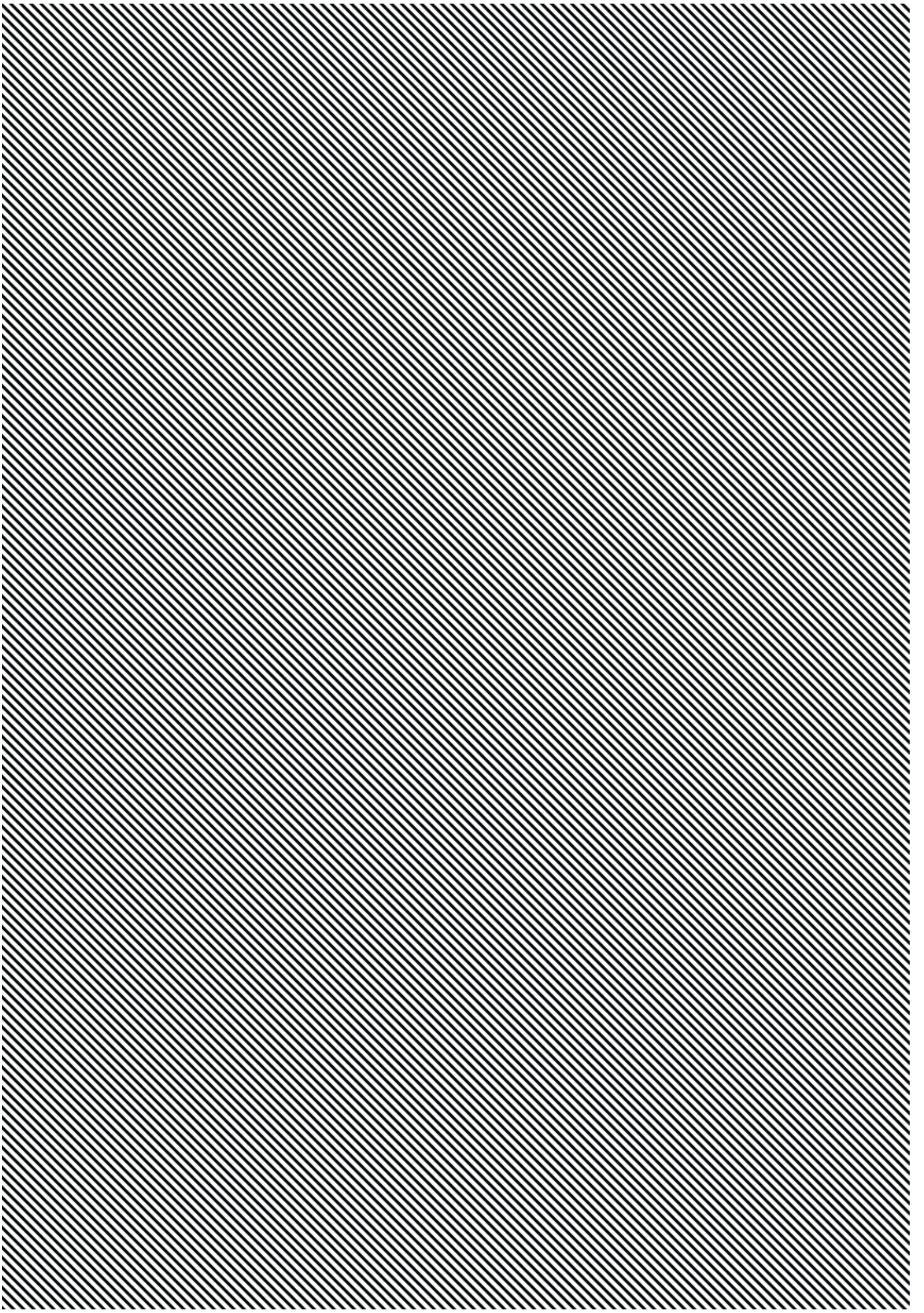

4 Results and Discussion

Following the conceptual considerations outlined in the previous chapters, the sketch in Figure 4.1 summarizes the strategy adopted to tackle such intricate problem. The steps were taken sequentially.

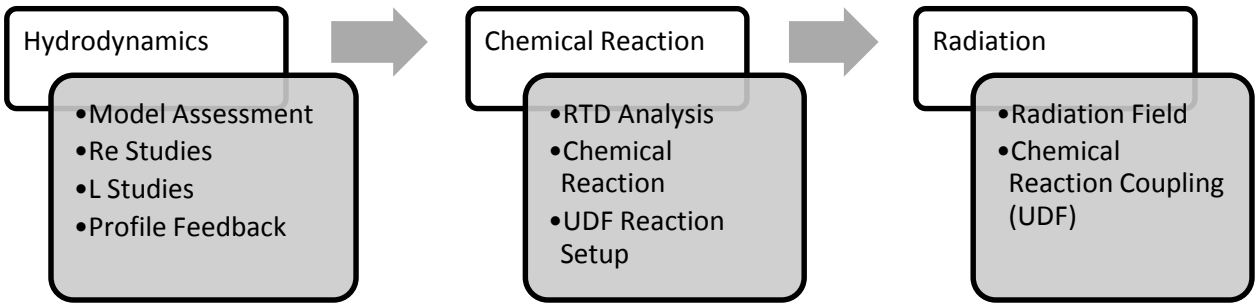

Figure 4.1 – Case tackling strategy

4.1 Turbulence Model: Implementation and Validation

A $k-\omega$ turbulence model was selected to assist the prediction of the flow characteristics inside the circular section pipe. While the $k-\varepsilon$ turbulence model has a wide acceptance and spread usage in many engineering applications, the $k-\omega$ was adopted due to better definition of the boundary layer at little more computational cost. This approach is very important as the results obtained will show.

Previous experiments have shown that the near-wall region can be largely subdivided into three layers [31], as can be seen in Figure 4.2. In the layer closest to the wall, called the viscous sub-layer, the flow can be considered laminar and, therefore, the molecular viscosity plays a dominant role in momentum, heat and mass transfer. In the outer layer, also known as the fully-turbulent layer, it is the turbulence that has the major role in transport phenomena. In between, there is a transitional area amid the previously described layers, where the contributions of viscosity and turbulence are both important.

To further improve these results, the enhanced wall treatment was used. This is a near-wall modelling method that combines the described a two-layer model with enhanced wall functions [18]. As outlined in chapter 3, the near-wall mesh can be refined to be able to resolve the laminar sub-layer (typically for $y^+ = 1$) and then the enhanced wall treatment will be identical to the traditional two-layer zonal model. However, care should be taken as, depending on the case study, this near-wall mesh refinement might come attached with a computational cost beyond reasonable.

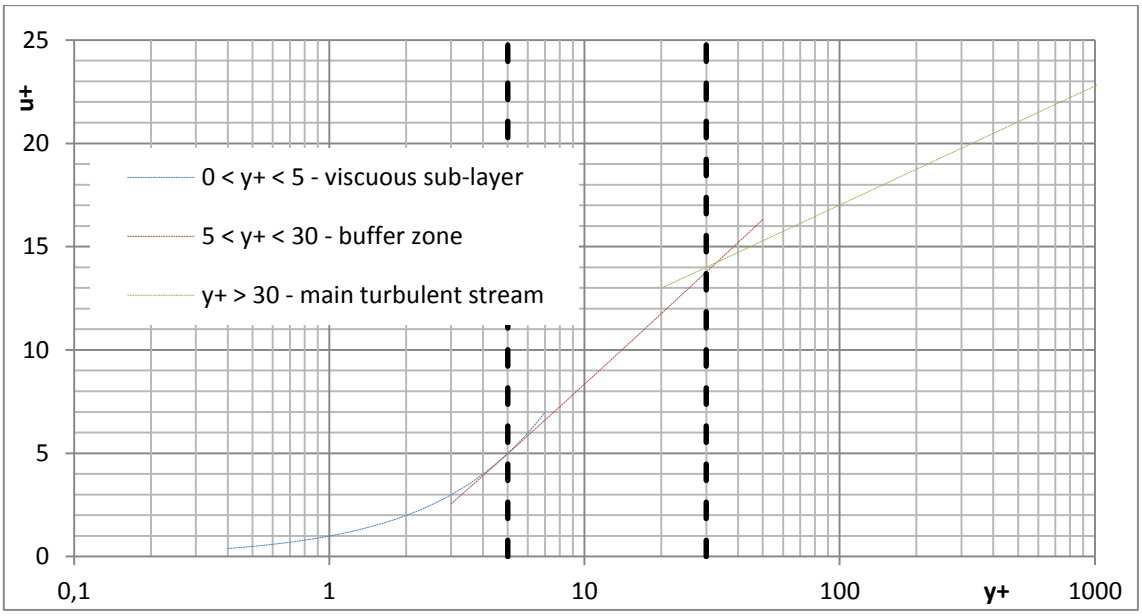

Figure 4.2 - Dimensionless velocity distribution at the near-wall region for turbulent flow

The flow behaviour in the above regions are governed by the following relations [31]:

$$u^+ = y^+, \qquad 0 < y^+ < 5 \tag{40}$$

$$u^+ = 5\ln(y^+ + 0.205) - 3.27\,, \qquad 5 < y^+ < 30 \tag{41}$$

$$u^+ = 2.5\ln(y^+) + 5.5\,, \qquad y^+ > 30 \tag{42}$$

The simulation results presented in Figure 4.3 shows the results for the operational conditions of the pilot plant, as described in *Table 3.1* and assuming the fluid properties in Table 4.1.

Table 4.1 – Fluid properties

Properties	**Pilot plant**	**Superpipe**
Material	Water	Air
Density (kg m^{-3})	1000	1.183
Viscosity (Pa s)	$1x10^{-3}$	$1.841x10^{-5}$

The simulations were initially set on ANSYS WORKBENCH, selecting and configuring FLUENT case on demand. The workflow devised in the previous chapter was followed.

Figure 4.3 to Figure 4.8 overlay several results to depict a good correlation between theory, experimental and simulation predictions.

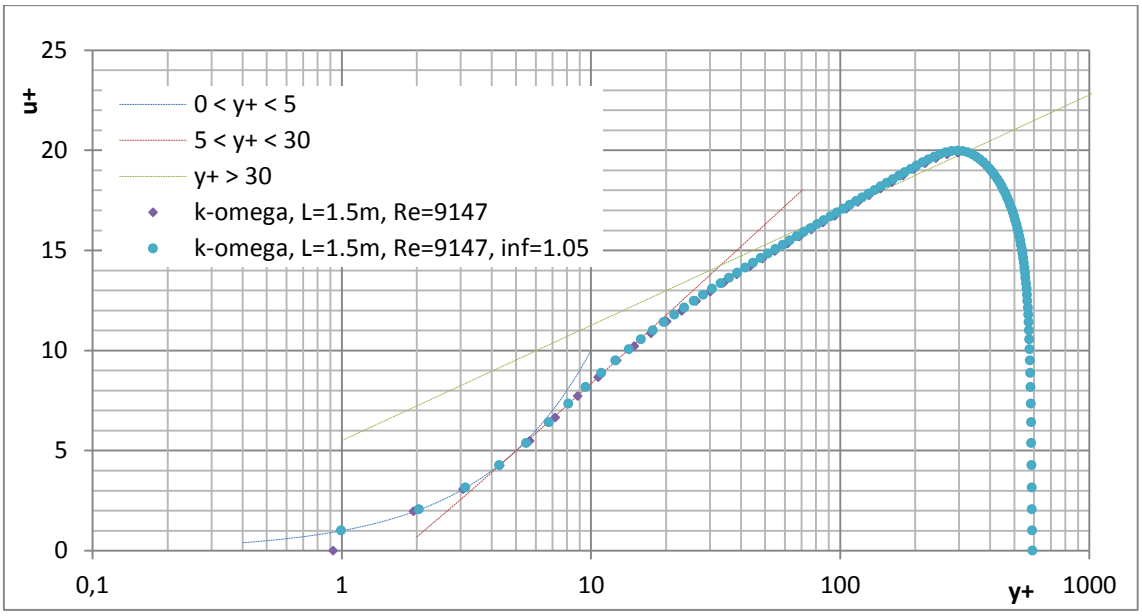

Figure 4.3 – Dimensionless velocity Vs. dimensional wall distance for pilot plant operational conditions (inflation=1.1) compared with mesh refinement (inflation=1.05)

Results in Figure 4.3 show good agreement with the boundary layer theory, while little to no improvement is visible by further refining the mesh (inflation 1.1 to 1.05).

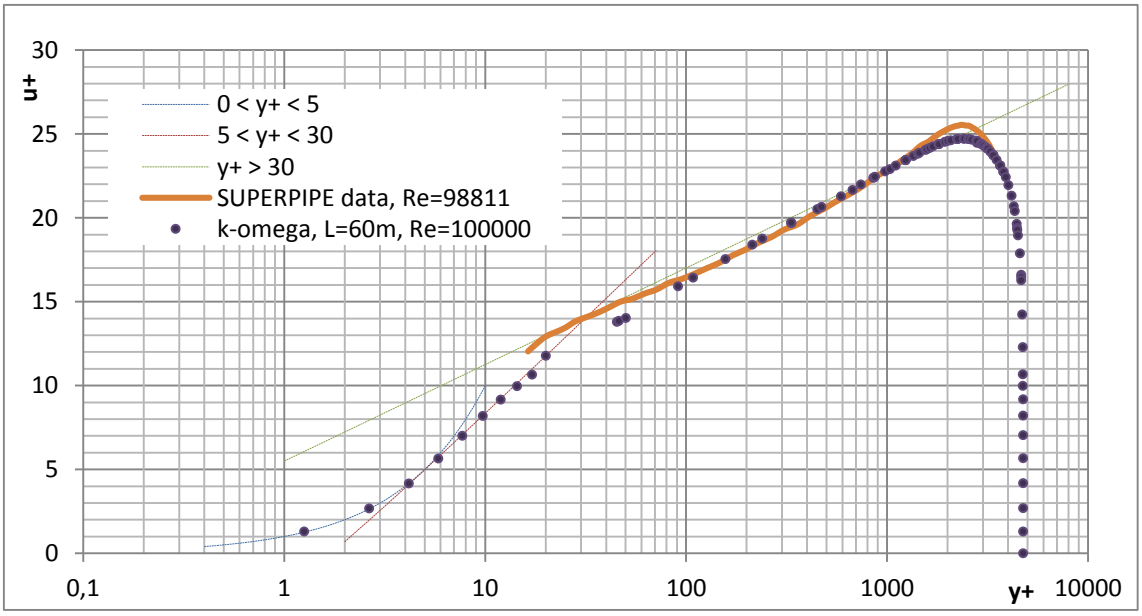

Figure 4.4 – Dimensionless velocity Vs. dimensional wall distance for SUPERPIPE simulation and experimental data

Figure 4.4 shows that the k-ω performs reasonably well when compared with the SUPERPIPE experimental results [32, 33].

As regards to the velocity profiles (Figure 4.5 and 4.6) obtained at the outlet, a good correlation with the theory [34] is also obtained. Here, the solid lines are obtained applying the dimensional

analysis proposed in the literature, namely by combining and rearranging Equations (35),(36),(37)and (42) to provide the desired velocity profile data (solid line).

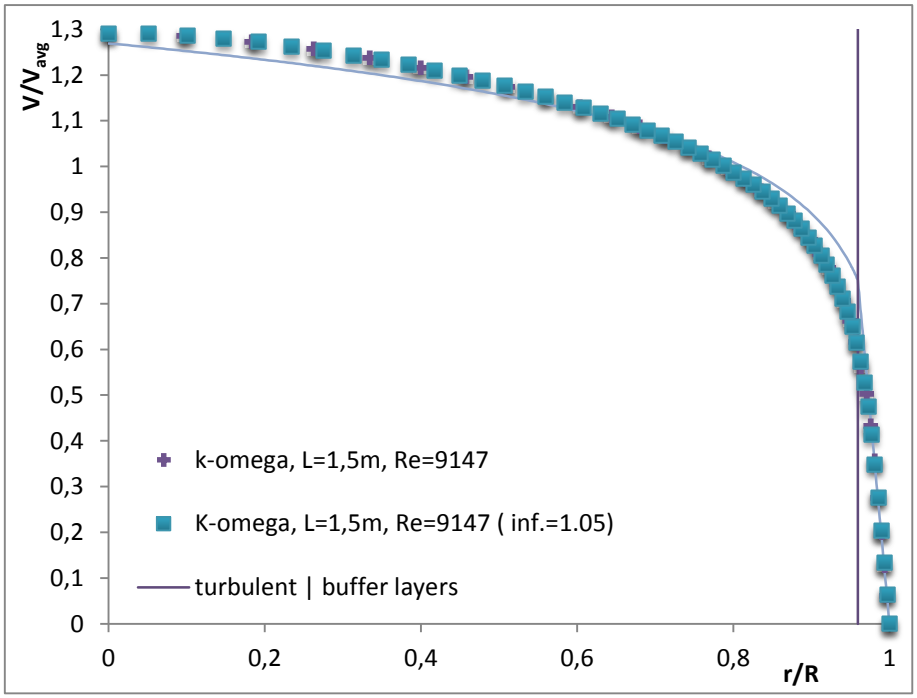

Figure 4.5 – Outlet velocity profiles for pilot plant operational conditions (inflation=1.1) compared with mesh refinement (inflation=1.05)

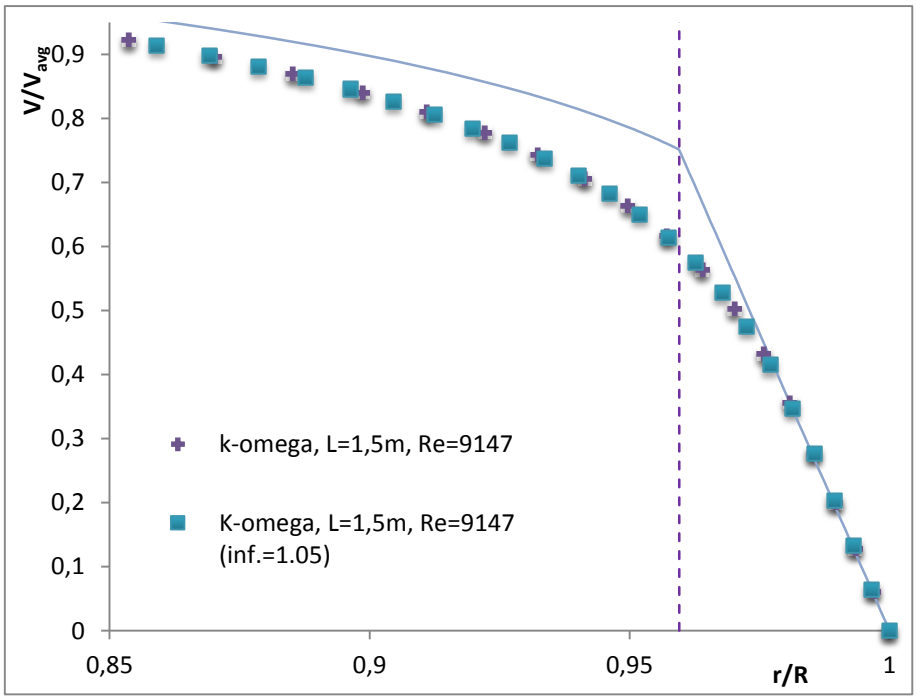

Figure 4.6 – Outlet velocity profiles detail (turbulent/buffer regions) for pilot plant operational conditions (inflation=1.1) compared with mesh refinement (inflation=1.05)

It is also clear that the mesh refinement applied (inflation 1.1 to 1.05) does not improve on the solutions and thus the result can be deemed mesh independent at this stage.

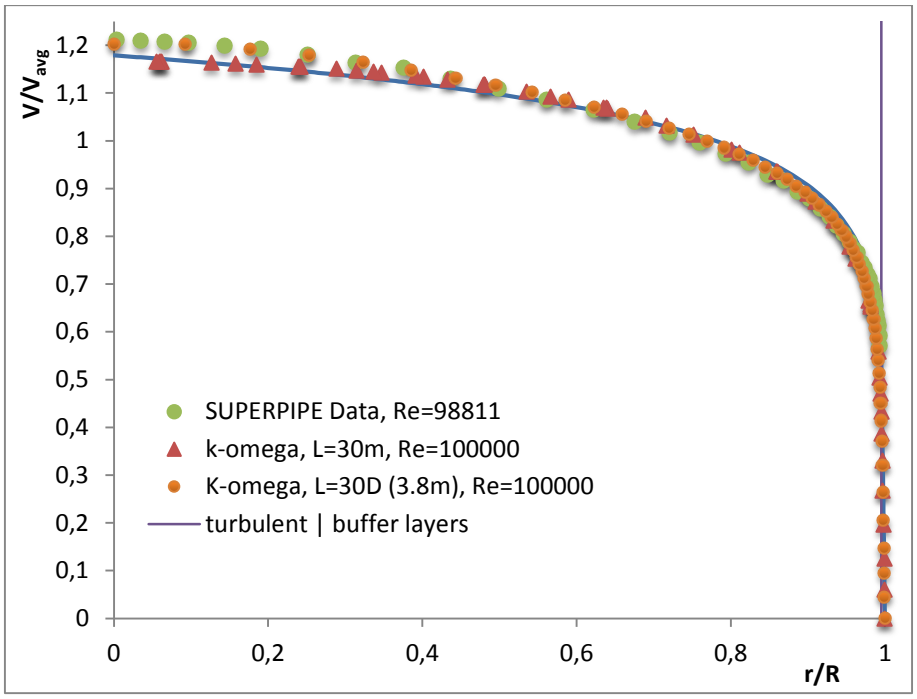

Figure 4.7 - Outlet velocity profiles for SUPERPIPE simulation and experimental data

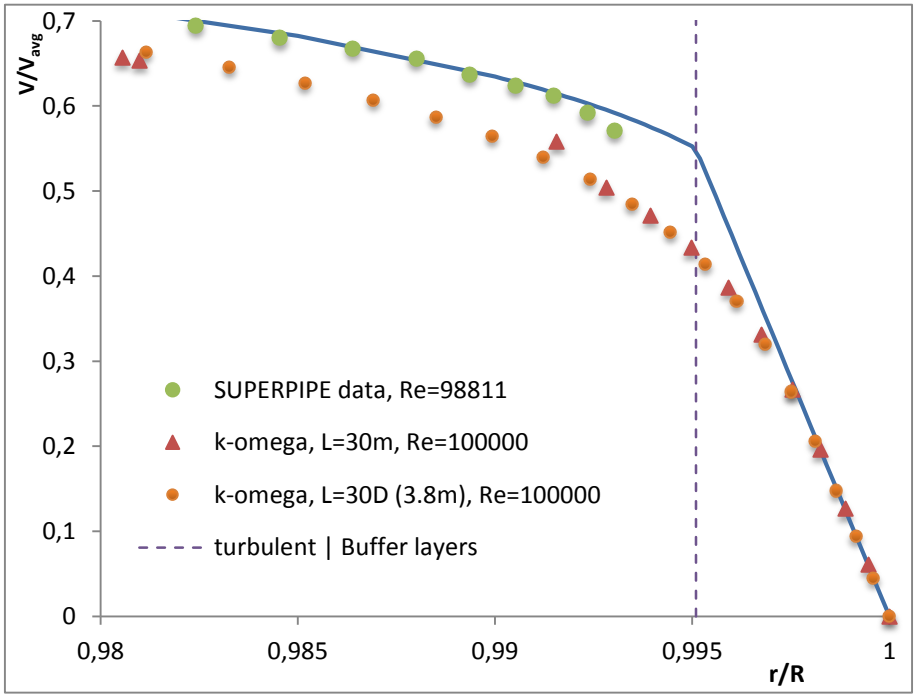

Figure 4.8 –Outlet velocity profiles detail (turbulent/buffer regions) for SUPERPIPE simulation and experimental data

Comparing Figure 4.5 with Figure 4.7 it is noticeable that, for higher *Re* number there is slightly better correlation between the theory and the model predictions.

To further access the model performance, the Reynolds stress tensor was plotted against experimental results found in the literature. Since no value or functions are promptly available in

FLUENT to extract such simulation results it was necessary to implement a custom field function to calculate that parameter. The Boussinesq Hypothesis states that the Reynolds stress tensor τ_{ij}, can be related to the mean strain rate tensor S_{ij} (eq. (7)), as follows:

$$\tau_{ij} = 2\mu_t S_{ij} - \frac{2}{3}\rho k \delta_{ij} \tag{43}$$

where, μ_t is turbulent or eddy viscosity, ρ is the density, $k$is the turbulence kinetic energy and δ_{ij} is the Kronecker delta. This, in combination with other FLUENT calculated values result in a plot of Reynolds stress tensor normalized by the frictional velocity (Figure 4.9).

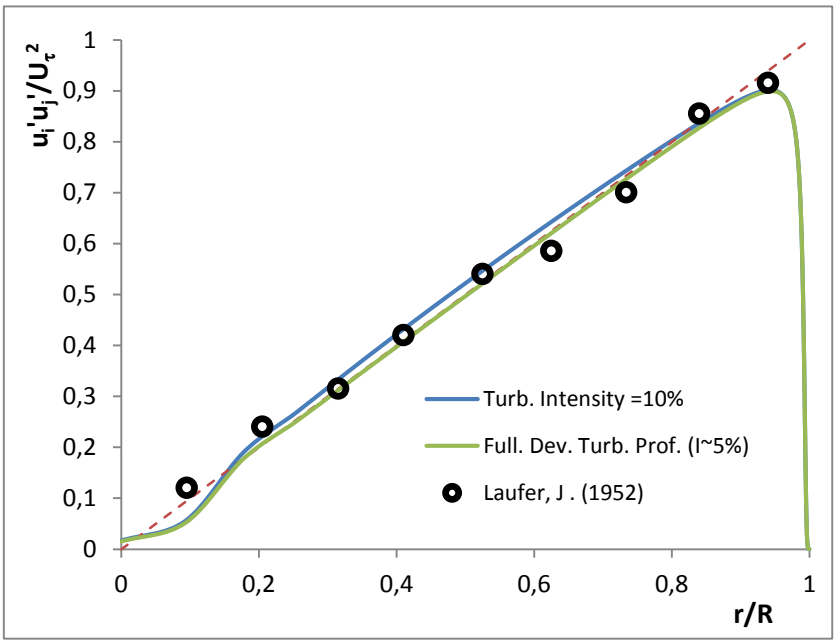

Figure 4.9 – Normalized pipe-flow properties, Re = 40 000

Being that the turbulence intensity I is defined by:

$$I \equiv \frac{u'}{U} = 0.16\, Re^{-\frac{1}{8}} \tag{44}$$

where, $u'$and U are the fluctuating and mean velocity, respectively, and Re is the Reynolds number calculated with respect to the pipe diameter. The turbulence intensity of a fully-developed flow can be estimated at the core from derived formulas obtained from empirical correlations, as shown above [18]. For reference the result obtained using a turbulence intensity of 10% is shown to demonstrate that it slightly overshoots, as expected. The data obtained at 5% turbulence intensity have a good correlation with the experimental values found in the literature [20].

4.1.1 Study of Reynolds Number

To access how good the model behaves across a wide range of operating conditions, a parametric study was setup in WORKBENCH. This study defines several design points, in which the Reynolds

number is modulated, from low Reynolds number and up to $Re = 200\,000$. The operational conditions were those stated in *Table 3.1*.

The simulations results were compared against the calculations provided by eq. (33), (34) and (36) and are presented in Table 4.2:

Table 4.2 – Results for calculated and simulated wall shear stress τ_w, and shear stress velocity u_* at several Re numbers

Re	τ_w (Pa), FLUENT	τ_w (Pa), eq. (33)	Diff. (%)	u_* (m/s), FLUENT	u_* (m/s), eq. (36)	Diff. (%)
5 000	6.052x10^{-02}	5.428 x10^{-02}	10.32%	7.780 x10-03	7.367 x10^{-03}	5.30%
10 000	1.902 x10^{-01}	1.793 x10^{-01}	5.73%	1.379 x10-02	1.339 x10^{-02}	2.91%
15 000	3.778 x10^{-01}	3.632 x10^{-01}	3.85%	1.944 x10-02	1.906 x10^{-02}	1.94%
20 000	6.184 x10^{-01}	6.011 x10^{-01}	2.80%	2.487 x10-02	2.452 x10^{-02}	1.41%
40 000	2.059 x10^{+00}	2.041 x10^{+00}	0.90%	4.538 x10-02	4.518 x10^{-02}	0.45%
80 000	6.988 x10^{+00}	7.007 x10^{+00}	-0.27%	8.359 x10-02	8.371 x10^{-02}	-0.14%
100 000	1.039 x10^{+01}	1.044 x10^{+01}	-0.54%	1.019 x10-01	1.022 x10^{-01}	-0.27%
200 000	3.595 x10^{+01}	3.632 x10^{+01}	-1.01%	1.896 x10-01	1.906 x10^{-01}	-0.50%

These results show good agreement between calculated and simulated results, in particular for higher Reynolds numbers. The model is thus considered capable to operate in a wide range of operational conditions while providing reasonable predictions.

4.1.2 Study of Pipe Length

In the same philosophy of the previous topic, another study was carried to determine the simulation response to the variation in the pipe's length.

At a finite distance from the entrance, L_e, pipe flow is entirely viscous and the axial velocity is then constant along x and thus a fully developed velocity profile is achieved. A valid approximation for smooth walls and turbulent flow is given by [29]:

$$\frac{L_e}{d} = 4.4\, Re_d^{\frac{1}{6}} \tag{45}$$

where, L_e is the entrance length (see Figure 4.10), d is the diameter and Re_d is the Reynolds number obtained for pipe flow.

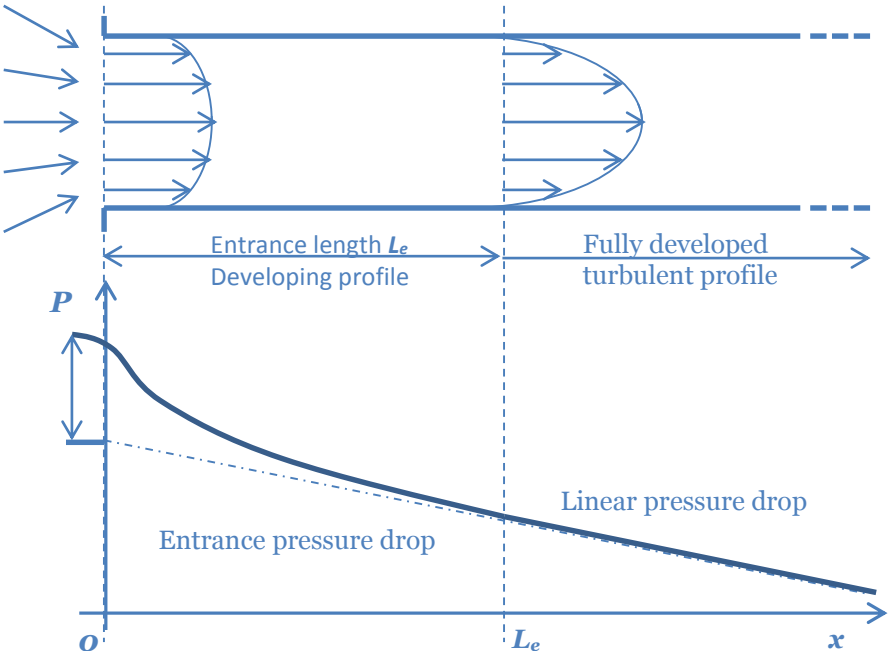

Figure 4.10 - Velocity profiles and pressure drop in a pipe entrance [29]

Taking advantage of FLUENT's automation strategies, in this case using Journal files, a profile feedback study was implemented. The protocol executed involved running a simulation, obtaining a result, saving the corresponding outlet profile and feeding it to the same case as an input velocity profile. The corresponding Journal file can be found in Appendix C. The practical result is an effective 'stretching' of the pipe conditions.

The results in Figure 4.11 show that if starting from a fully developed velocity profile little change is to be expected in the following iterations, as is to be expected in face of eq. (45). The detailed area in Figure 4.11 also demonstrates the same effect with feedback of the turbulent kinetic energy k and the specific dissipation rate ω profiles – little or no consequence is visible in the behavior in the outlet velocity profile. Another common alternative strategy to simulate these results is to

implement the desired inlet profile by programing a corresponding UDF (example provided in Appendix D, but not implemented).

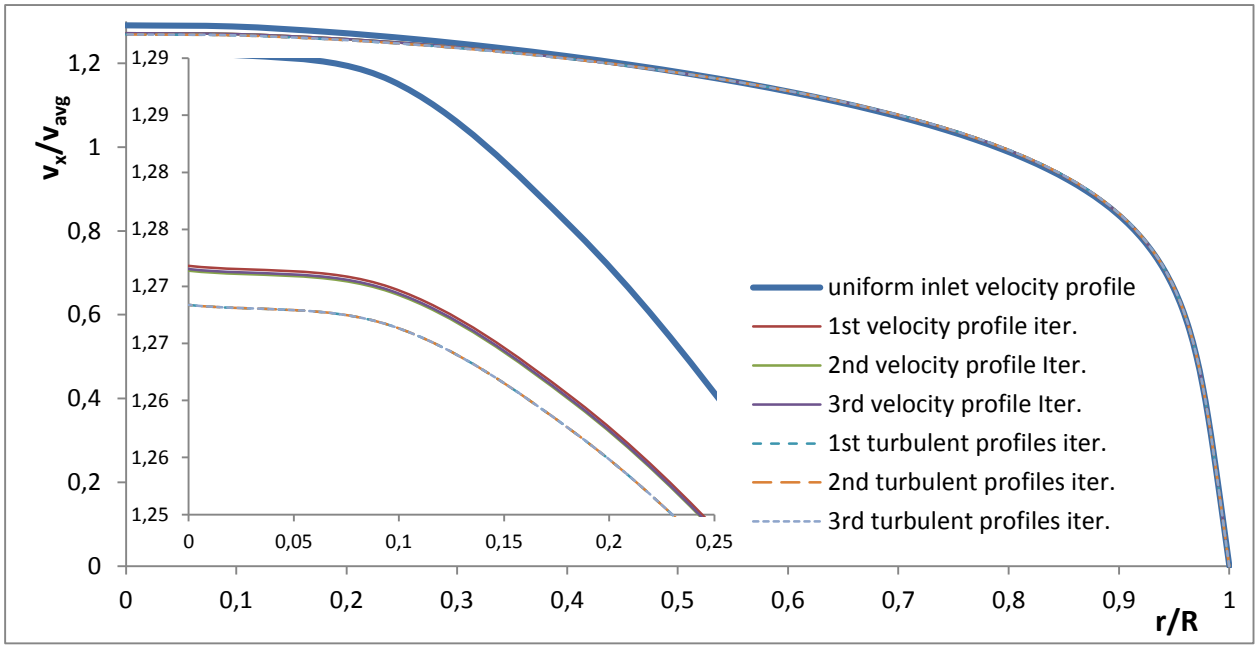

Figure 4.11 – Normalized velocity profiles obtained after velocity and turbulence feedback (Re=9147, L=1,5m)

As regards to the length study, starting from a uniform velocity profile the outlet profiles in Figure 4.12 were obtained for the parametric study shown in Table 4.3:

Table 4.3 – Length parametric study for Re 10 000, D=0.0464

	L_e	10D	15D	20D	30D	32D*	40D
Pipe length (m)	**0.948**	0.464	0.696	0.928	1.392	1.5	1.856

(*) Re 9147

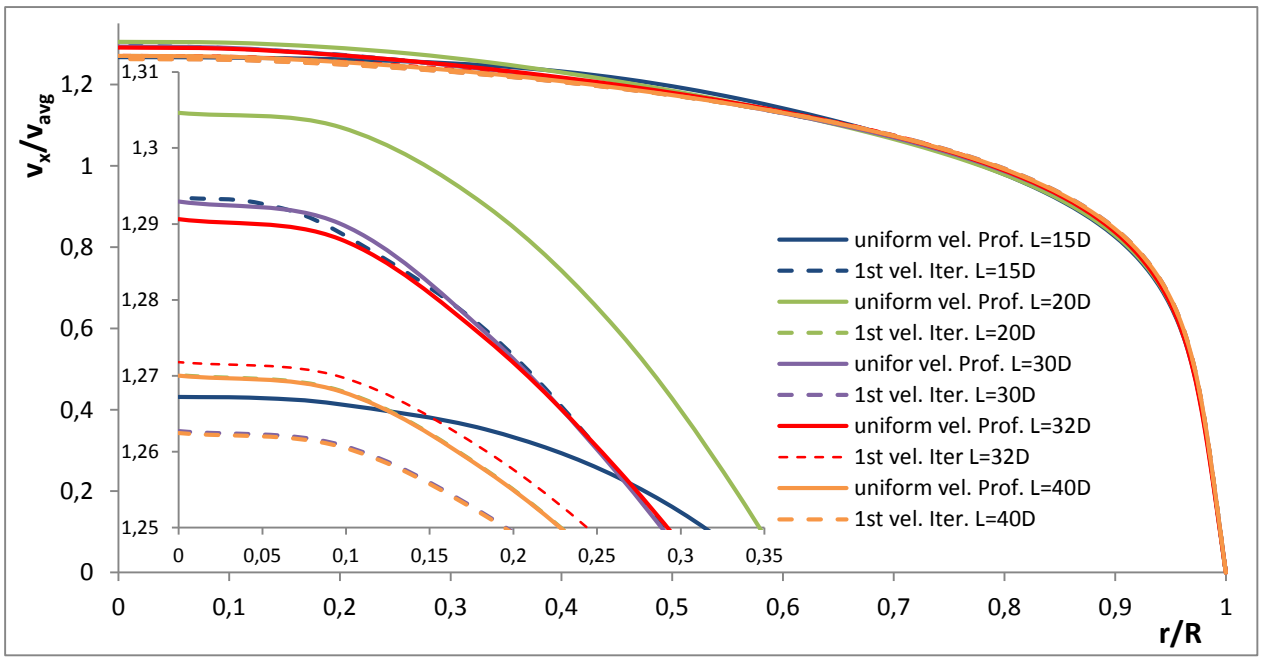

Figure 4.12 - Normalized velocity profiles obtained for the length parametric study

This study shows that the simulation results obtained are in agreement with the outcomes devised by the theory. In fact, for lengths up to $20D$ the profile is not completely formed and the effect in the results can be better understood by looking at the detail of the pipe axial region. In this section for $L = 15D$ it can be seen clearly that the profile has not fully developed yet. Also, the iterative feedback of the profile obtained from the uniform inlet profile has good correspondence to the double of that distance, *i.e.*, the $15D$ feedback closely follow the $30D$ profile and the $20D$ feedback overlaps $40D$ profile, confirming the doubling effect, as expected.

It should be noted that, in agreement with eq. (45) for L around $10D$, or lower, the solution did not converge.

4.2 Reaction Engineering

As mentioned before, as the flow field inside a reactor deviates from the ideal behaviour, the flow patterns became increasingly complex and cumbersome to model. A practical strategy to circumvent the need to detail the entire flow field was popularized by Danckwerts [35] through correlation of the flow field with the time that the fluid elements reside inside the reactor *i.e.*, the distribution of residence times (RTD).

Therefore, RTD analysis is a very simple yet powerful tool that can be used to characterize chemical reactors, maximizing performance and troubleshooting or investigating malfunction by predicting stagnant reactor zones and recycling or channelling of fluid.

In order to analyse the residence time distribution of the fluid in a reactor the following set of relationships have been developed [36].

As different elements of fluid may take different routes through the reactor it seems clear that each will take different amount of time to leave the reactor. The distribution of such exit times, plotted as the E(t) curve, is the RTD of the fluid. The concentration of a tracer $C(t)$ may be used to define $E(t)$ such as:

$$E(t) = \frac{C(t)}{\int_0^\infty C(t)dt} \quad and \quad \int_0^\infty E(t)\,dt = 1 \tag{46}$$

For determining the RTD a step tracer perturbation was implemented, as the cumulative distribution $F(t)$ can be determined directly. The non-dimensional curve $F(t)$ is then obtained by normalizing the tracer concentration at the outlet $C(t)$ by the initial step concentration C_0:

$$F(t) = \frac{C(t)}{C_0} \quad or \quad F(t) = \frac{X(t)}{X_0} \tag{47}$$

Where X_0 and $X(t)$ denotes the initial mass fraction of tracer and at a given time t, respectively.

A relationship between $F(t)$ and $E(t)$ can be obtained by postulating that, in the exit stream, the fraction of tracer is the same as the fractions of tracer younger than an age t, which means:

$$F(t) = \int_0^t E(t)dt \tag{48}$$

And by differentiation:

$$E(t) = \frac{dF(t)}{dt} \tag{49}$$

For ideal reactors, the average residence time $\bar{t}$ is defined as being equal to:

$$\bar{t} = \frac{V}{Q} \tag{50}$$

where V is the reactor volume and Q is the flow rate.

In the absence of dispersion and for constant volumetric flow, the RTD is found to being equal to the mean residence time $\bar{t}$, which is given by [37]:

$$\bar{t} = \int_0^\infty t\, E(t) dt \tag{51}$$

4.2.1 RTD Analysis

For determination of the RTD, a 1% (w/w) step tracer input is introduced at the inlet. This analysis was done in transient time dependency, therefore it is crucial to determine an appropriate time stepping in order to minimize the numerical diffusion. To do so, the adequate time stepping is found by:

$$time\ step = \frac{\Delta_{x,min}}{v_{x,max}} \tag{52}$$

where $\Delta_{x,min}$ is the minimum axial mesh dimension and $v_{x,max}$ is the maximum axial velocity component. Taking the tube length, dividing it for the number specified and reading the maximum value for a velocity profile a value around 0.006 s was obtained. The simulation duration, in number of time steps, can be then calculated by dividing the number the $\bar{t}$ by the time steps. This value should be at least doubled to capture any eventual delay in the simulation results. The results obtained are summarized in the following table:

Table 4.4 – Results summary for the RTD experiment

V (m^3)	Q (m^3/s)	$\bar{t}$ (s)	Time Step (s)	τ(s)	V_d	V_d (%)	σ^2	D/uL
2.54×10^{-03}	3.33×10^{-04}	7.61	0.05	7.52	2.83×10^{-05}	1%	1.79	0.015
			0.006	7.53	2.49×10^{-05}	1%	1.34	0.012
			0.005 (*)	7.53	2.75×10^{-05}	1%	1.49	0.013
			0.005	7.54	2.42×10^{-05}	1%	1.36	0.013
			0.001	7.47	4.69×10^{-05}	2%	0.89	0.008

(*) – uniform inlet profile

As devised, the results presented in Figure 4.13 and Figure 4.14 show that time steps around 0.006 s, or lower, provide very similar results, thus no noticeable impact from numerical diffusion. On the other hand, time step of 0.05 s, provided for comparison purpose, show a much larger deviation as result of numerical diffusion.

The cumulative distribution $F(t)$ curves obtained are displayed in Figure 4.13.

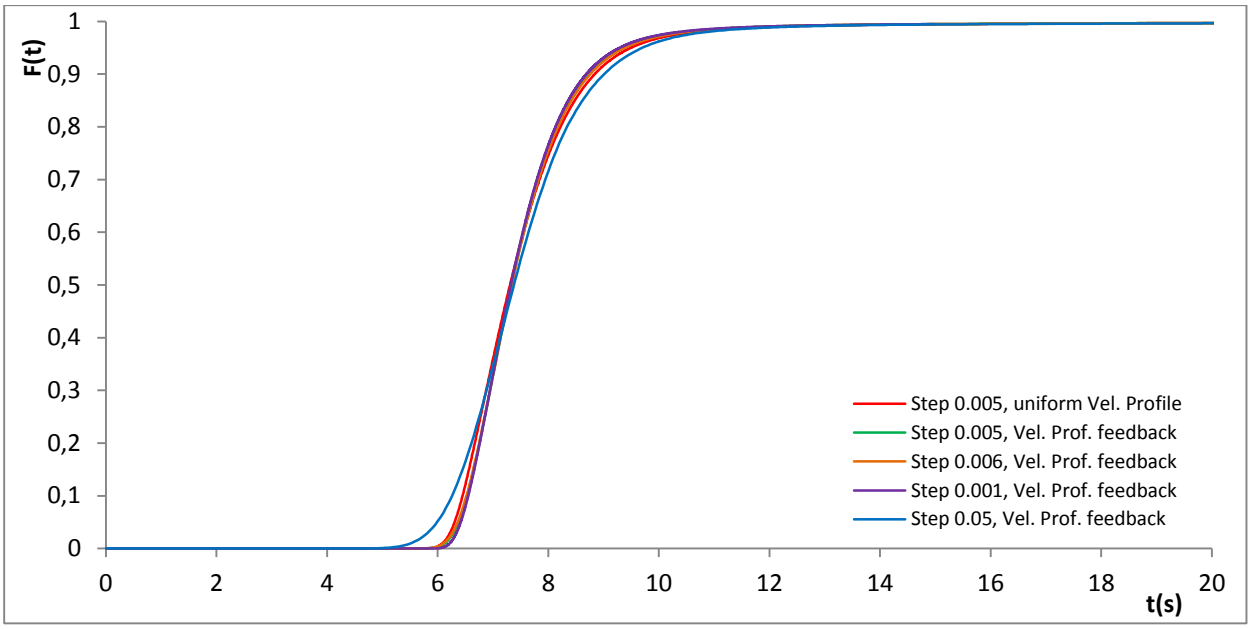

Figure 4.13 - Cumulative distribution $F(t)$ for several time steps

To better analyse the results detailed breakthrough curves are also provided in Figure 4.14.

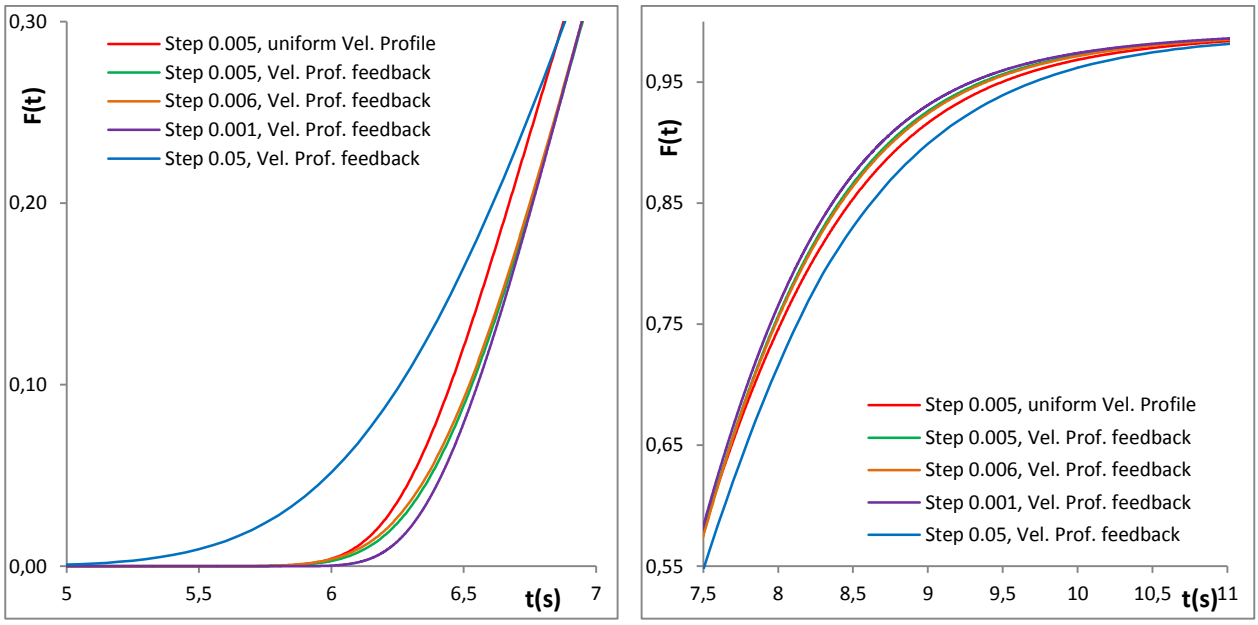

Figure 4.14 – Details of the cumulative distribution $F(t)$ for several time steps

The RTD is obtained by numerically differentiate and integrate the $E(t)$, in a spreadsheet, according to equations (49) and (51), respectively. The results are found in Table 4.4 and plotted in Figure 4.15.

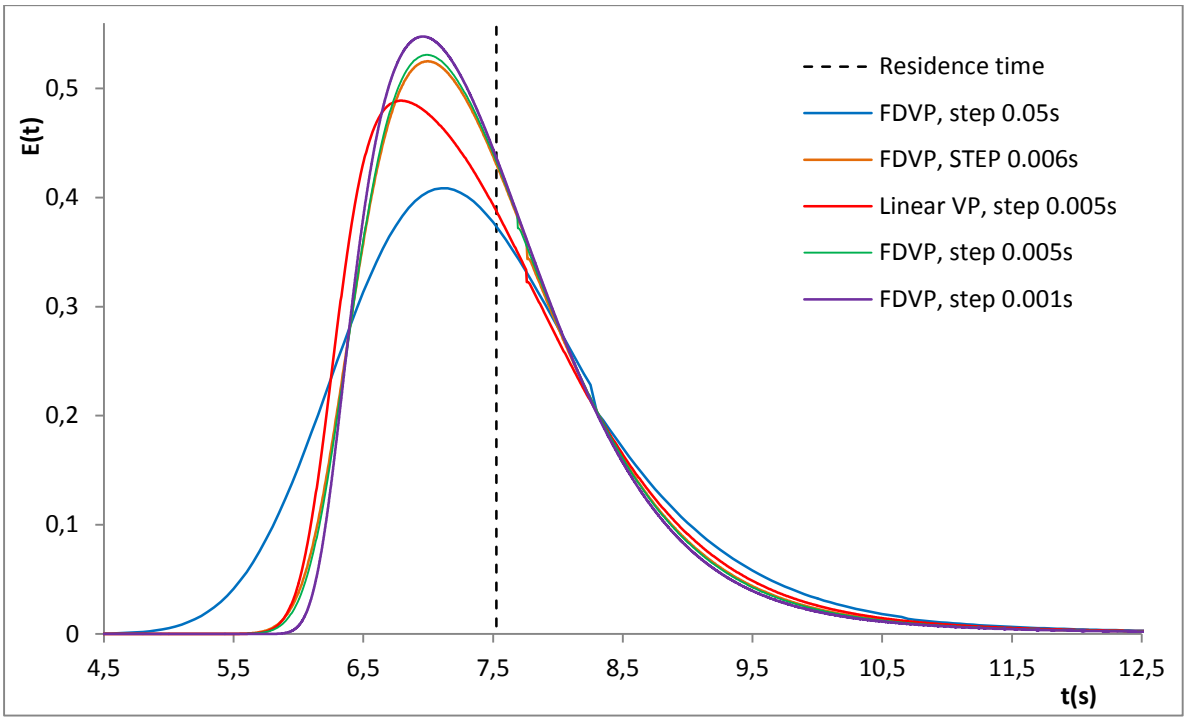

Figure 4.15 – Residence time distribution $E(t)$, for several time steps

Some amount of axial dispersion is indeed present and clearly visible in Figure 4.15. This is also corroborated by the non-zero σ^2 values in Table 4.4, thus deviating from plug flow as expected for turbulent flows. It is also clear that the input profile affects the RTD, in this case (uniform velocity input) providing for a lower residence time due to higher axial dispersion. The dead volumes are found to be negligible as it is normal for this tubular configuration.

4.2.2 Chemical Reaction

FLUENT allows to setup a fairly complex reaction set, and some examples of such implementations can found in the literature [16, 27] with good results prediction. Nonetheless, due to high complexity, to observe time constrains and due to lack of availability of some chemical reaction data, this objective was not pursued.

Thus, in order to study the simulator response, a simple irreversible reaction was set up in FLUENT, of the type:

$$A \longrightarrow Products \tag{53}$$

Given the previous studies conducted in the pilot plant (see chapter 3), a first-order rate equation of the following type was implemented:

$$-r_A = \frac{dC_A}{dt} = kC_A \tag{54}$$

where C_A is the instantaneous concentration of the species A and k is the reaction kinetic constant. The kinetic constant used was the same found in chapter 3, after conversion to time dependency.

The conversion of A, X_A, may be obtained by:

$$X_A = \frac{F_{A,in} - F_{A,out}}{F_{A,in}} \tag{55}$$

where $F_{A,in}$ and $F_{A,out}$ are the flow rates of A entering and leaving the reactor, respectively.

For steady state ($Q_{in} = Q_{out}$), and for a first order rate of conversion of A (eq. (55)) this can be rewritten to obtain the following relation:

$$X_A = 1 - e^{-k\tau} \tag{56}$$

where k is the kinetic constant and τ is the residence time. For small deviations from plug flow, the dispersion term $\frac{D}{uL}$ becomes small and the conversion can be obtained by [36]:

$$X_A = 1 - e^{-k\tau + (k\tau)^2 \frac{D}{uL}} \tag{57}$$

FLUENT provides a finite-rate combined with an eddy-dissipation model, where both the Arrhenius and eddy-dissipation (mixing limited) reaction rates are calculated, and the resulting net reaction rate is taken as the minimum of these two rates [18]. As a first order rate or an UDF were used to calculate the chemical rate, and not the Arrhenius equation, preliminary testing shows that the limiting reaction is in fact in the chemical rate and not in the mixing rate.

Therefore, the reaction was setup in FLUENT as laminar finite-rate, thus not accounting for turbulent mixing limitations.

Also, providing that the chemical reaction implemented follows a first order concentration decay, FLUENT's User Interface can be used to insert such reaction by manipulation of the Arrhenius equation parameters. This is better understood by taking eq. (19) and assuming that the pre-exponential factor A_r will host the value for the kinetic constant k, by forcing the temperature exponent β_r and the activation energy E_r exponentials to zero. The first order dependency of the concentration is obtained in eq. (17) by inserting a singular rate exponent for the species A, which would ultimately result in eq. (54). The most common strategy though, is to code a volumetric rate reaction using FLUENT's UDF, as provided in Appendix D, compile it and properly hook it to the simulation. The comparison between both strategies confirms that they provide the same results. Nonetheless, UDF will be crucial for coupling the radiation field and thus was be extensively used. The results obtained are summarized in Table 4.5.

Table 4.5 – Chemical reaction conversion results

X_A		X_A FLUENT					
eq. (56)	eq. (57)	UI (Mod. Arrh.)	UDF	UDF Step=0.001	UDF High. Trans. formulation	UDF Higher Residuals	UDF Combined
5,977%	5,973%	6,391%	6,391%	6,383%	6,386%	6,384%	6,383%

Table 4.5 shows that FLUENT's results are overestimating the conversion, which for this reactor configuration and operational conditions should be lower than the conversion given by equation (56) or (57). As this could be due to configuration of FLUENT spatial discretization, solution monitors or the time stepping used, further studies were carried to find that these have little impact, even when combined, in the conversion obtained by FLUENT – see Table 4.5. At this stage one should also conjecture if the meshing has the necessary resolution. Nonetheless, due to time constrains this hypothesis was not validated. Figure 4.16 shows the reactant and products breakthrough curves as the reactant A is depleted and products are formed.

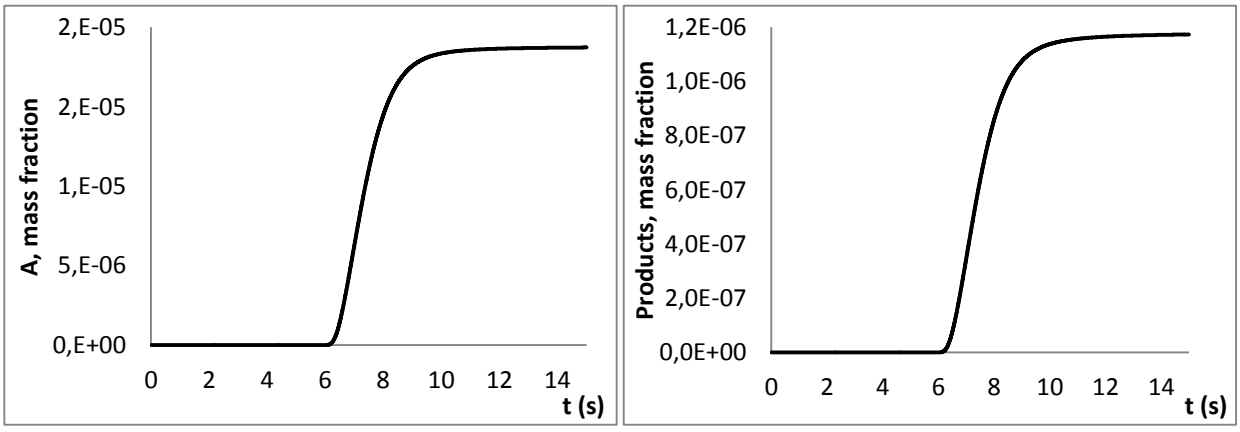

Figure 4.16 – Mass fraction of A and products breakthrough curves

Figure 4.17 provides a clear depiction of the early chemical reaction stages, as the reactant *A* in added in the reaction medium.

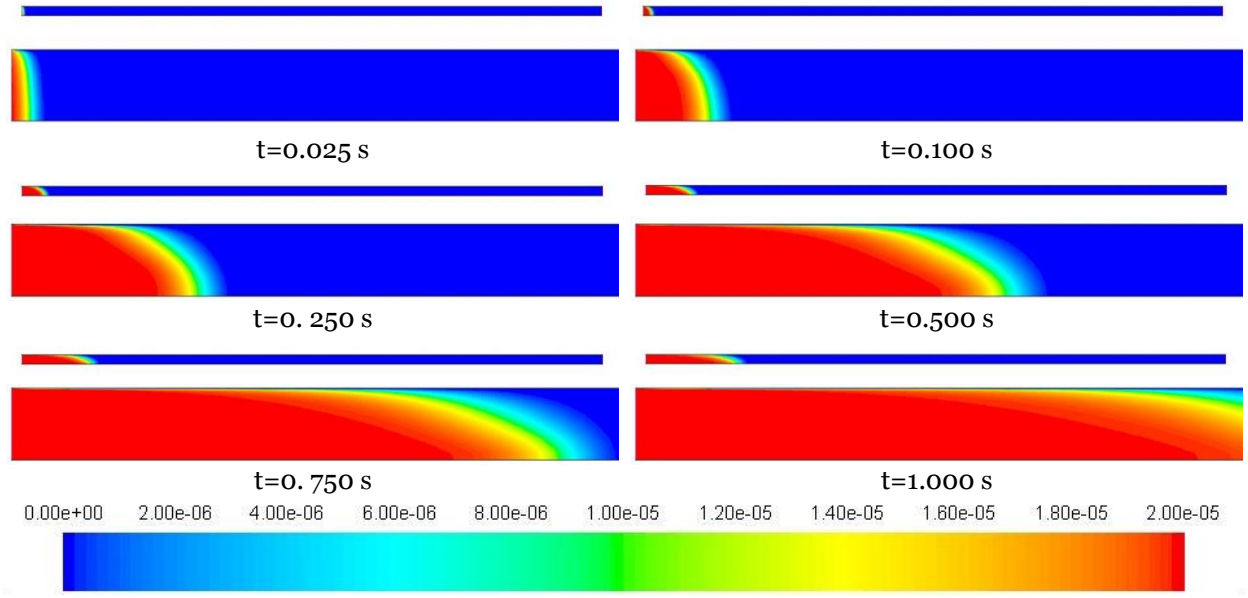

Figure 4.17 – Mass fraction of A – detail at inlet during first simulation steps

Figure 4.18 shows that, as the reaction advances with flow and time, the formation of products is also noticeable.

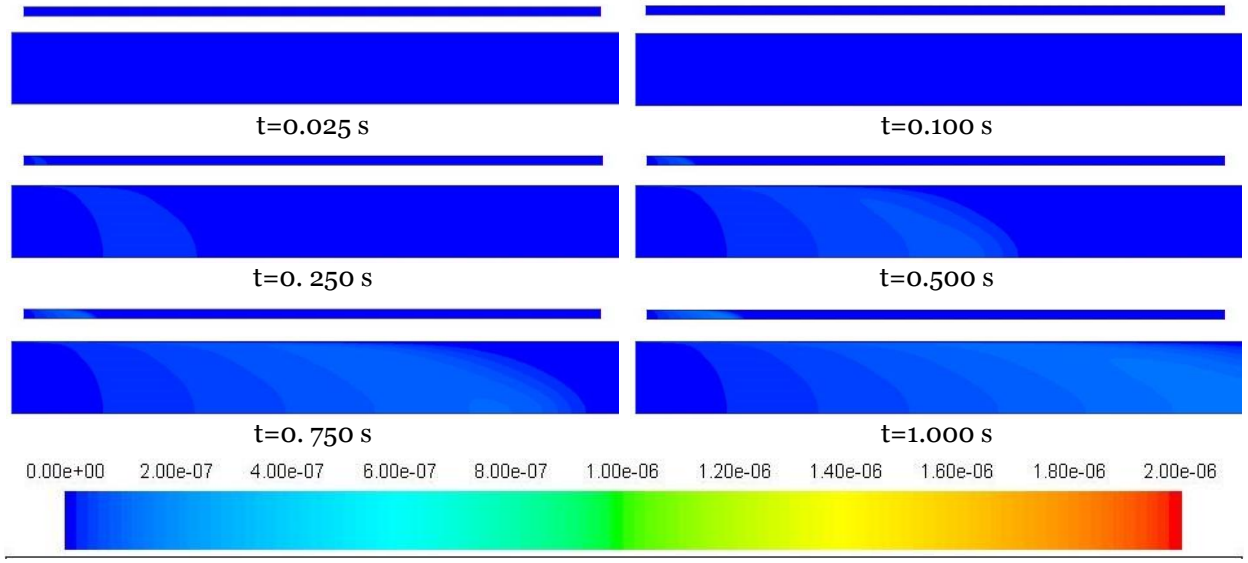

Figure 4.18 - Mass fraction of Products – detail at inlet during first simulation steps

This visual qualitative information is one of the many advantages that come attached to CFD tools where the provided valuable glimpse of what is happening may denounce a bad physics model.

Figures 4.19 to 4.22 provide a comprehensive visual asset of the chemical reaction, as it occurs throughout the reactor.

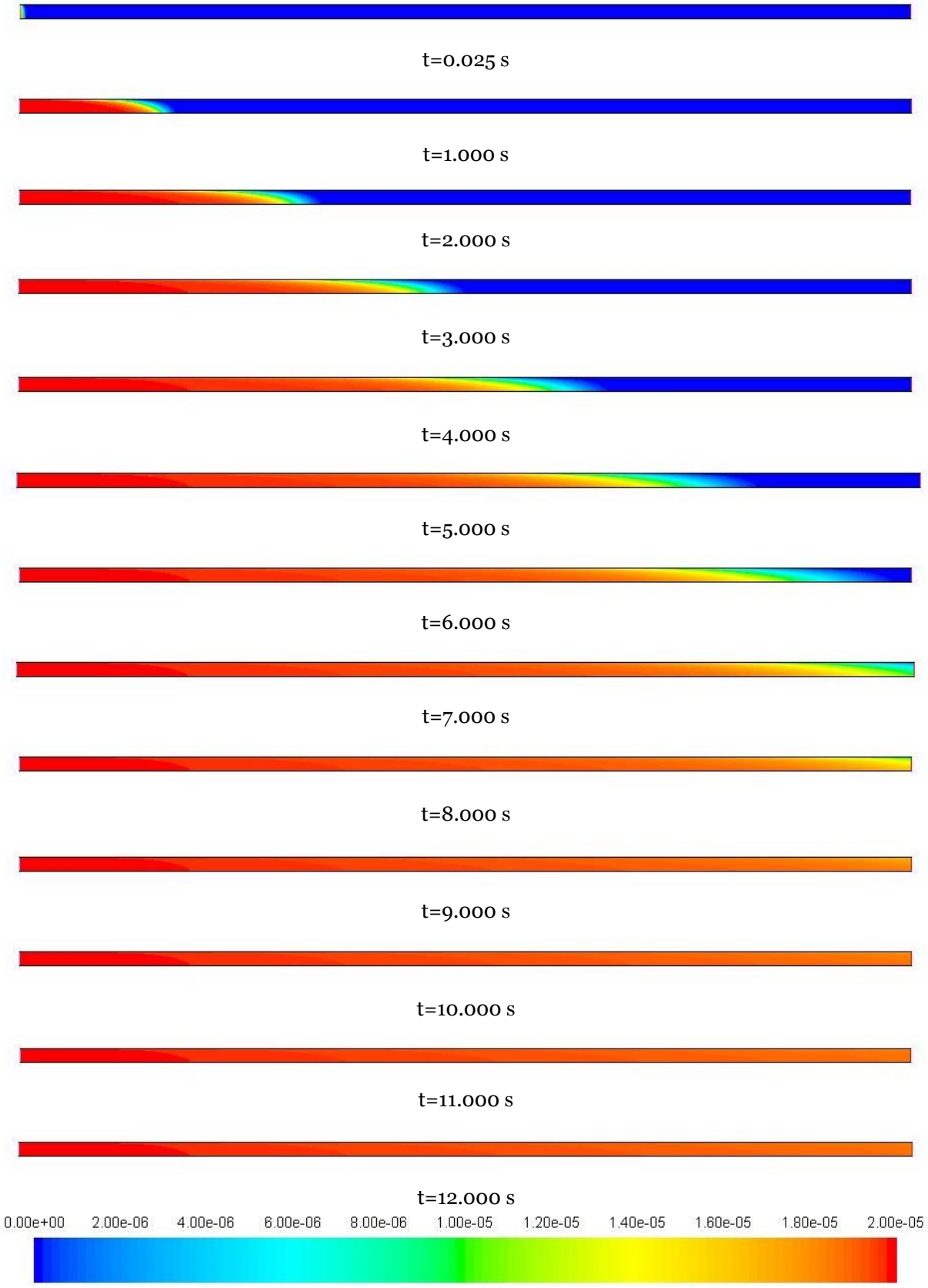

Figure 4.19 - Mass fraction of A – throughout the reactor at several time steps

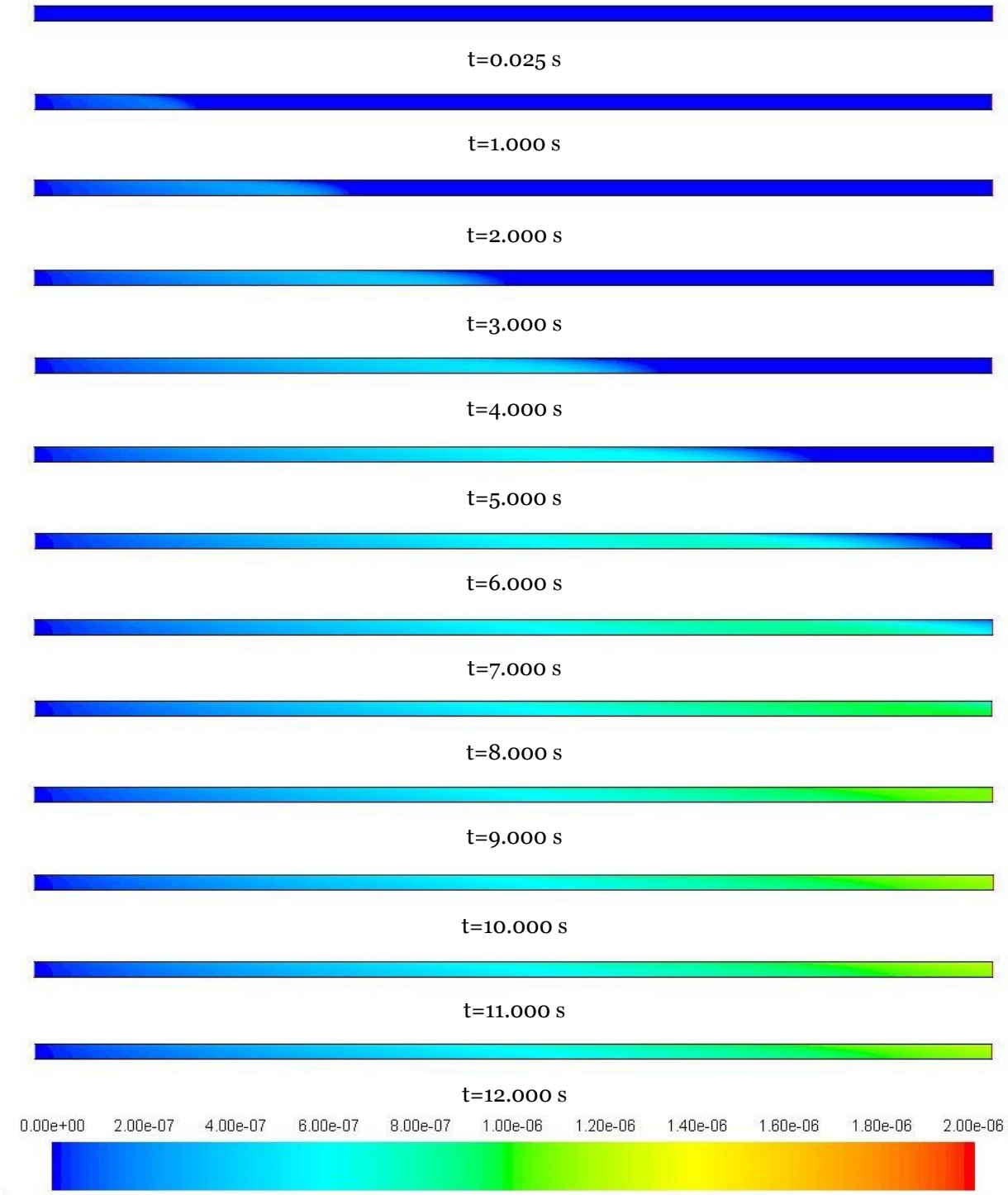

Figure 4.20 - Mass fraction of Products – throughout the reactor at several time steps

Examining Figure 4.17 through Figure 4.20 it is clearer the presence of axial dispersion and how it affects the concentration profile and ultimately the conversion of *A*. This is caused by a combination of the velocity (profile), turbulent mixing and molecular diffusion.

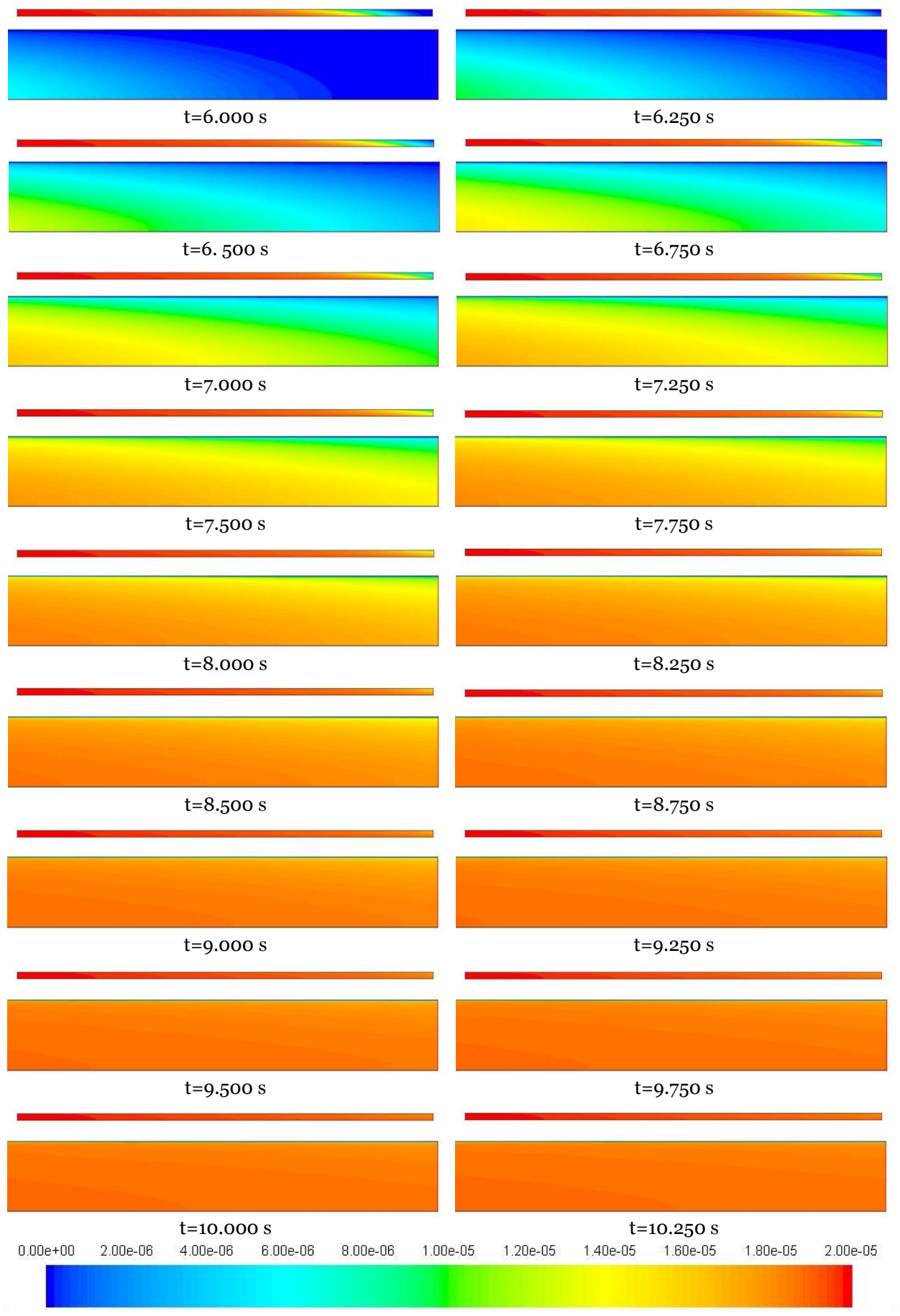

Figure 4.21 - Mass fraction of A – detail at outlet during the last simulation steps

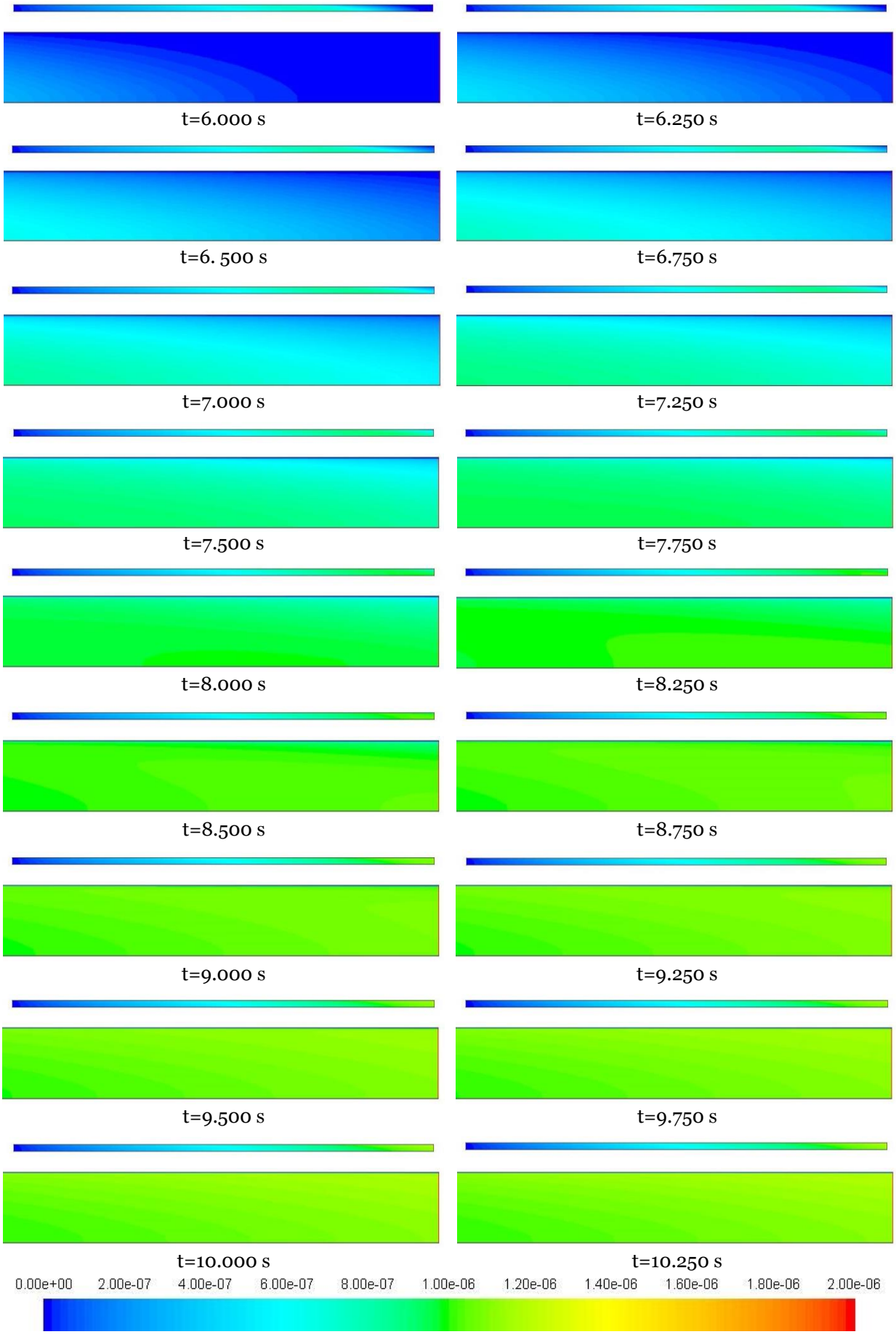

Figure 4.22 - Mass fraction of Products – detail at outlet during the last simulation steps

4.3 Radiation

As mentioned in the previous chapters, radiation is involved in key steps in any photochemical or photocatalytic process. Hence, in order to combine the radiation effect with the chemical reaction it is mandatory to know and account for the radiation field inside the reactor.

4.3.1 Radiation Field

To obtain a radiation field, and since a $2D$ model is being used, some simplifications and assumptions had to be made. Given that the average UV radiation measured at the pilot plant during the experiments was 30 W/m^2 this value was taken as reference for the available radiation at the exterior tube wall. The resulting radiation passing through the glass tube walls was then subtracted by 4%, to account for reflected light (air/glass), and further reduced by assuming that the borosilicate tube has an UV transmittance of at least 80%, which was found to be a typical value for this material. This points to a radiation power of ~24 W/m^2 available at the inside wall. With respect to the reaction domain, the fluid was assumed to have a UV Transmittance of 88%, which corresponds to an absorption coefficient of 12.78 (m^{-1}). The other properties were maintained similar to those of water, as the concentration of the pollutants could be considered residual.

The Radiation model was activated in FLUENT and the Discrete Ordinates Model was selected. The angular discretization was increased to 6x6 divisions and 3x3 pixels, which should provide sufficient resolution for this application. Also, in order to minimize the effects of thermal radiation from temperature gradients between the fluid and the boundaries, the temperature of the fluid, inlet and outlet, was reduced to 1 K. The resulting field is displayed in Figure 4.23:

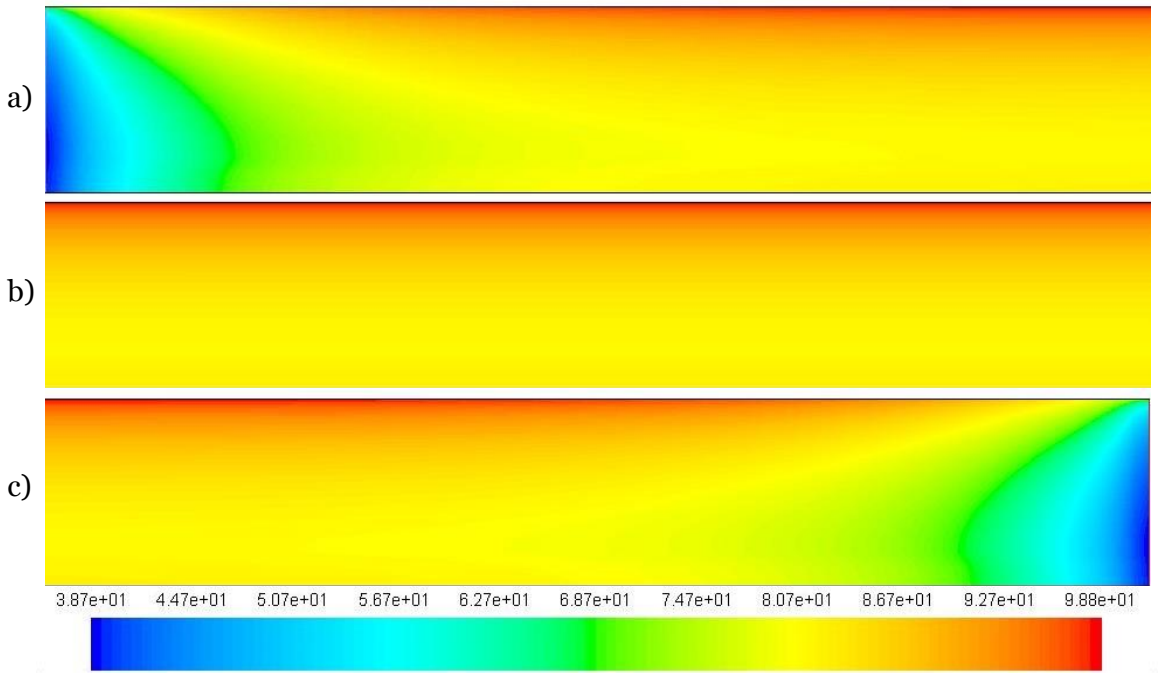

Figure 4.23 – Contours of incident radiation (Wm^{-2}): a) inlet side; b) middle section; and, c) outlet side.

Looking at the above picture, a shadowed region is clearly present both at inlet and outlet. This is due to the lack of radiation contribution from the dark sides. It is also noticeable, that the Incident Radiation field have the same distribution throughout middle section and is symmetrical at the inlet and outlet. The calculated average Incident radiation was 90.3 Wm^{-2}.

4.3.2 Coupling Radiation and Chemical Reaction

To account for the radiation field, earlier studies suggested [38, 39] that the influence of radiation could be correlated with the reaction rate constant k, as a function of light intensity I, by the following relationship:

$$k = k'I^{\alpha} \qquad (58)$$

where k′ ($s^{-1}(Wm^{-2})^{-\alpha}$) is by definition a rate constant independent of light intensity and α is an order constant.

In the absence of experimental data at several radiation intensities, necessary to compute k' and α values, these were estimated taking in to consideration the global reaction rate constant and linearizing eq. (58) by arbitrage of reaction constants around the known value. The following table holds the parameters tested and the resulting conversion of A:

Table 4.6 – Eq. (58) parameters and conversion of A obtained by FLUENT UDF

k'	α	X_A
0.002082	0.40	6,10%
0.002952	0.30	6,18%
0.004064	0.20	6,19%
0.004840	0.10	6,32%
0.006886	0.05	6,40%

The above parameters were once more inserted in FLUENT's user interface and passed to the UDF. This greatly simplified the iterative process that followed. The UDF also takes the value of the radiation intensity for each grid cell and use it to compute the reaction rate taking place in that cell. As a conversion similar to the global reaction is achieved between α=0.1 to 0.05, this indicates that we are operating in a region – or very close to – where the reaction have little dependency on the radiation intensity, *i.e.*, increasing the radiation intensity doesn't translate to improved reaction speed. This finding is consistent with the results of other studies [40] which translates to a lower quantum yield, that is, the growing number of absorbed photons does not result in the initiation of more primary events, nor the steps that follow, thus a plateau is attained.

Figures 4.24 and 4.25 compare both strategies outcomes.

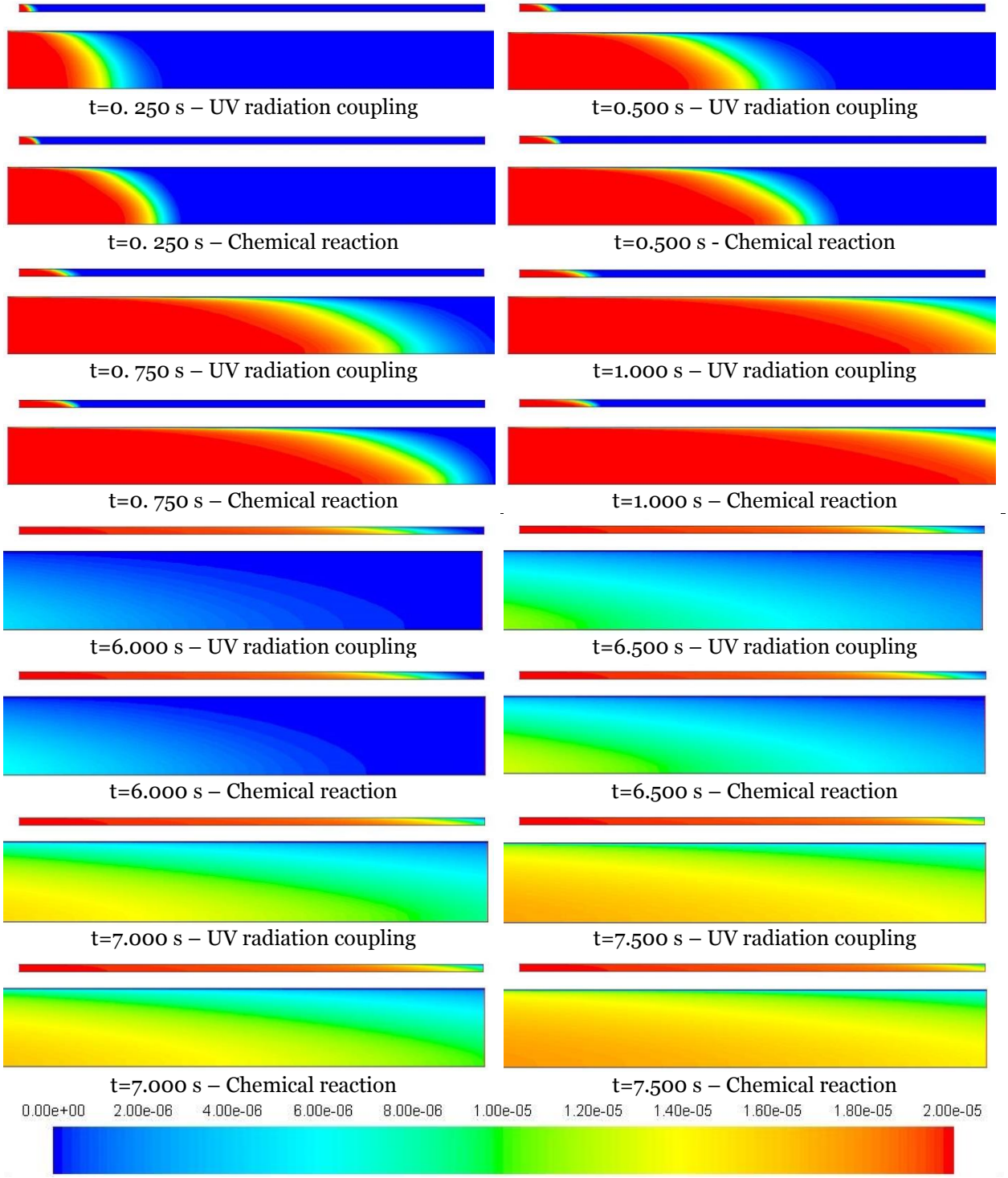

Figure 4.24 - Comparison between the mass fraction of A obtained for Chemical reaction and UV radiation coupling– detail at inlet and outlet

As expected the advance of the mass fraction is very similar as it is heavily dependent on the hydrodynamics. Very small differences may also arise from the fact of the stepping used was different (0.005 rad. Vs 0.001 che.), as was clearly shown on RTD studies in the previous chapters. The introduction of the influence of the radiation is clearly visible in a wider reaction front in the case of UV radiation coupling.

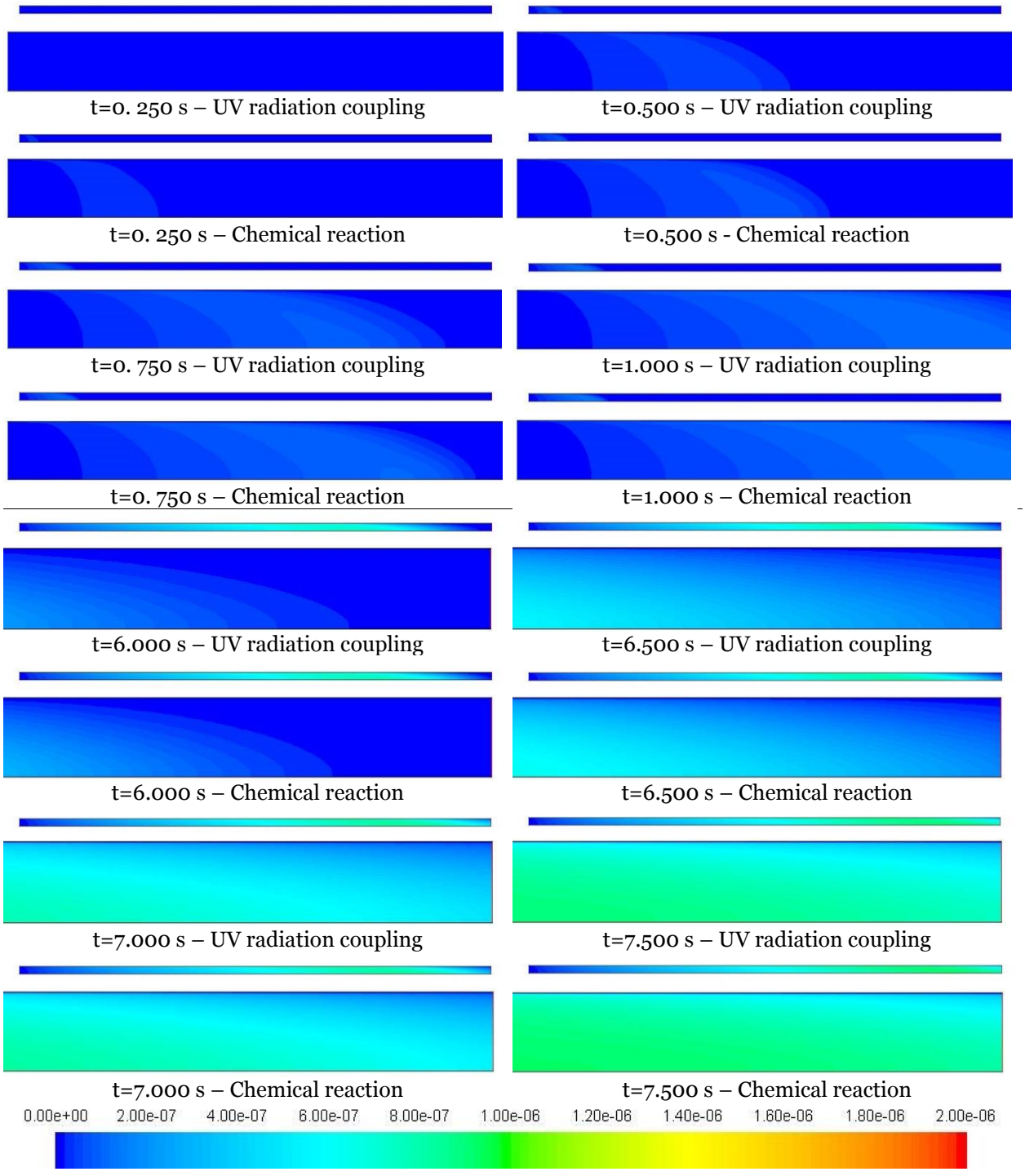

Figure 4.25 – Comparison between the mass fraction of Products obtained for Chemical reaction and UV radiation coupling– detail at inlet and outlet

Again, these results are very similar. In fact, the small differences at the inlet could be explained by the dark or shadowed areas which, for UV radiation coupling, clearly influence the reaction in those regions as should be expected.

Intentionally left blank

5

CONCLUSIONS

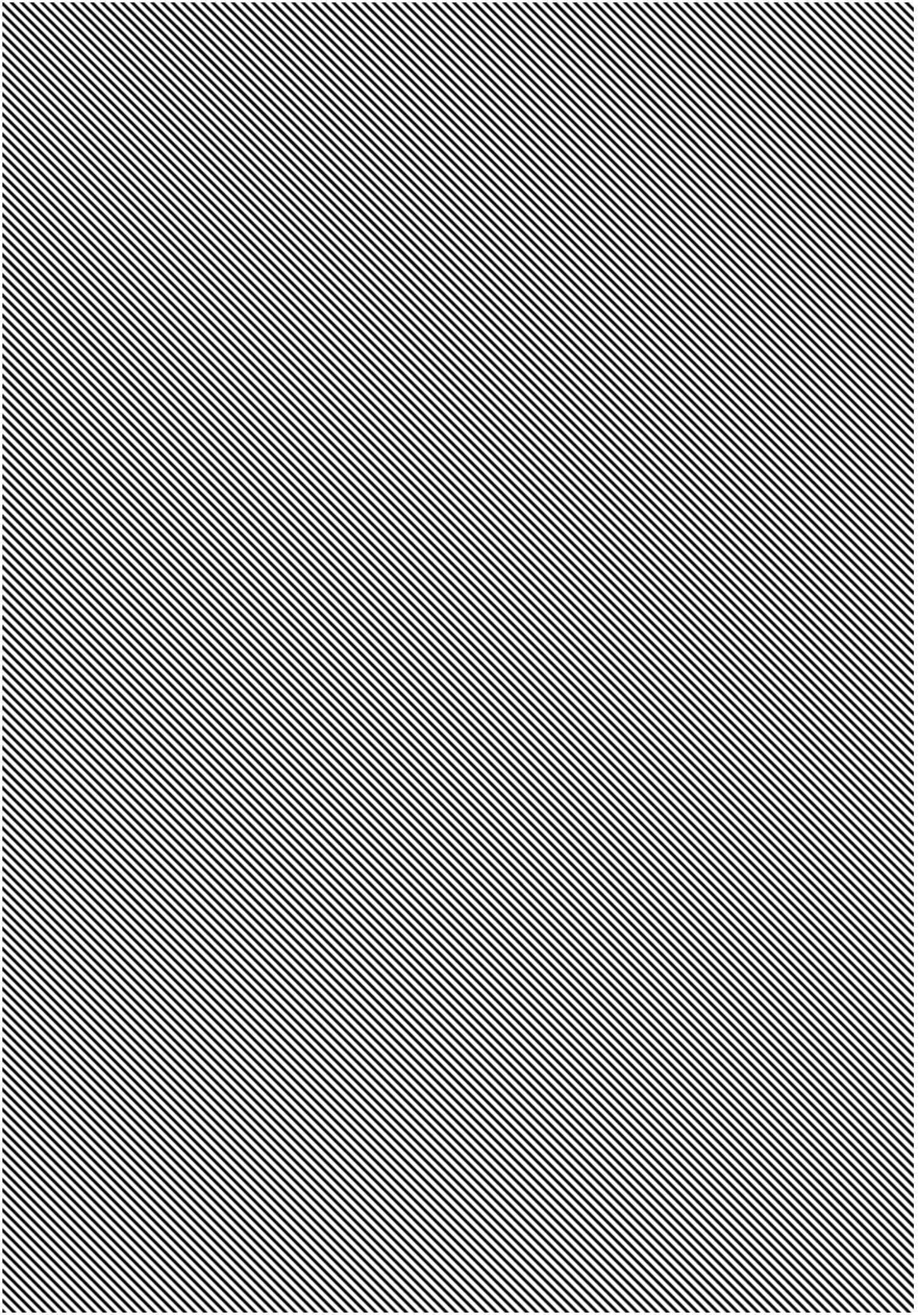

5 Conclusions

A simple process model was accomplished where a reaction model considering the influence of a radiation field and the concentration of a pollutant, as well as mass transfer and fluid dynamics within the reactor were also accounted for. Thus, to some extent, the adopted strategy will be independent of the reactor configuration and dimension and can be consequently used for scale-up purposes, process optimization or for the development of entirely new reactor setup.

While some of the work can be deemed incomplete or needing of further experimental data (radiation impact on reaction kinetics) or validation (ideally, PIV or LDA for hydrodynamics) it also lays ground for future developments which cannot be achieved without encountering such challenges along the path. In fact, many original objectives suffered several adjustments toward the objective of fully simulate a photocatalytic reactor.

5.1 Objectives Completion

Following the objectives outlined in chapter 1, the following remarks summarize the degree of accomplishment of each proposed goal.

An extensive and broad knowledge regarding the ANSYS CFD package was successfully gathered and consolidated. To fulfil this goal, numerous unrelated engineering cases were studied and implemented in ANSYS, as provided in the training materials. This would also involve gathering data for other sources and studying the theory guides.

Adding to the experience gathered, as mentioned previously, an extensive bibliographic research was carried and some linked study cases were implemented. This will support the selection of a suitable turbulence model. Successful testing and validation of hydrodynamics studies was performed. A parametric study as carried to access the model behaviour to geometric and operational constraints.

The reactor was characterized in terms of residence time distribution, laying the foundations for chemical reaction implementation. Afterwards, a simple chemical reaction was implemented in FLUENT. Furthermore, for added flexibility and future radiation accounting the chemical reaction was also implemented through means of an UDF.

As regards to the radiation, a feasible associated field was obtained and a simple strategy for coupling the radiation with chemical reaction was devised and implemented with relative success.

As such, the objective of obtaining an integrated methodology, combining the hydrodynamics, chemical reaction and radiation is believed to be achieved.

Generally, all the initially proposed goals and objectives were reached, as demonstrated in the previous chapters.

5.2 Limitations and Future Work

There are some limitations that should be noted and taken in to account when developing future related work.

First, insufficient data regarding the impact of radiation on the global kinetic constant forced an iterative process to adjust to the selected power law model. Ideally, this could be obtained by performing the pollutant degradation at several irradiation intensities and correlating with the global kinetic constant [39]. This could be challenging in a pilot plant where the solar radiation is used as source.

Second, to gain supplementary confidence in the predicted flow field, taking advantage of available technologies, such as PIV, further experimental testing could bring added confirmation and reliance on the implemented models. However, this study could be very time consuming and expensive to implement.

Third, strategies for accounting the turbulent mixture/reaction in the chemical reaction step should be researched and implemented.

Finally, as regards to the model used, the 2D planar section simulated may be too simple to account for all the physics normally involved in such turbulent systems (as 3D motion: rotational, torsional, etc.). In fact, as recommendation for future work, a full 3D model was started to be developed, as can be seen in Appendix B. Besides accounting for all the physical dimension of the flow, a 3D model would enable the usage of FLUENT's Solar Load as radiation source (only available in 3D). This was the main drive when developing such preliminary model.

6

REFERENCES

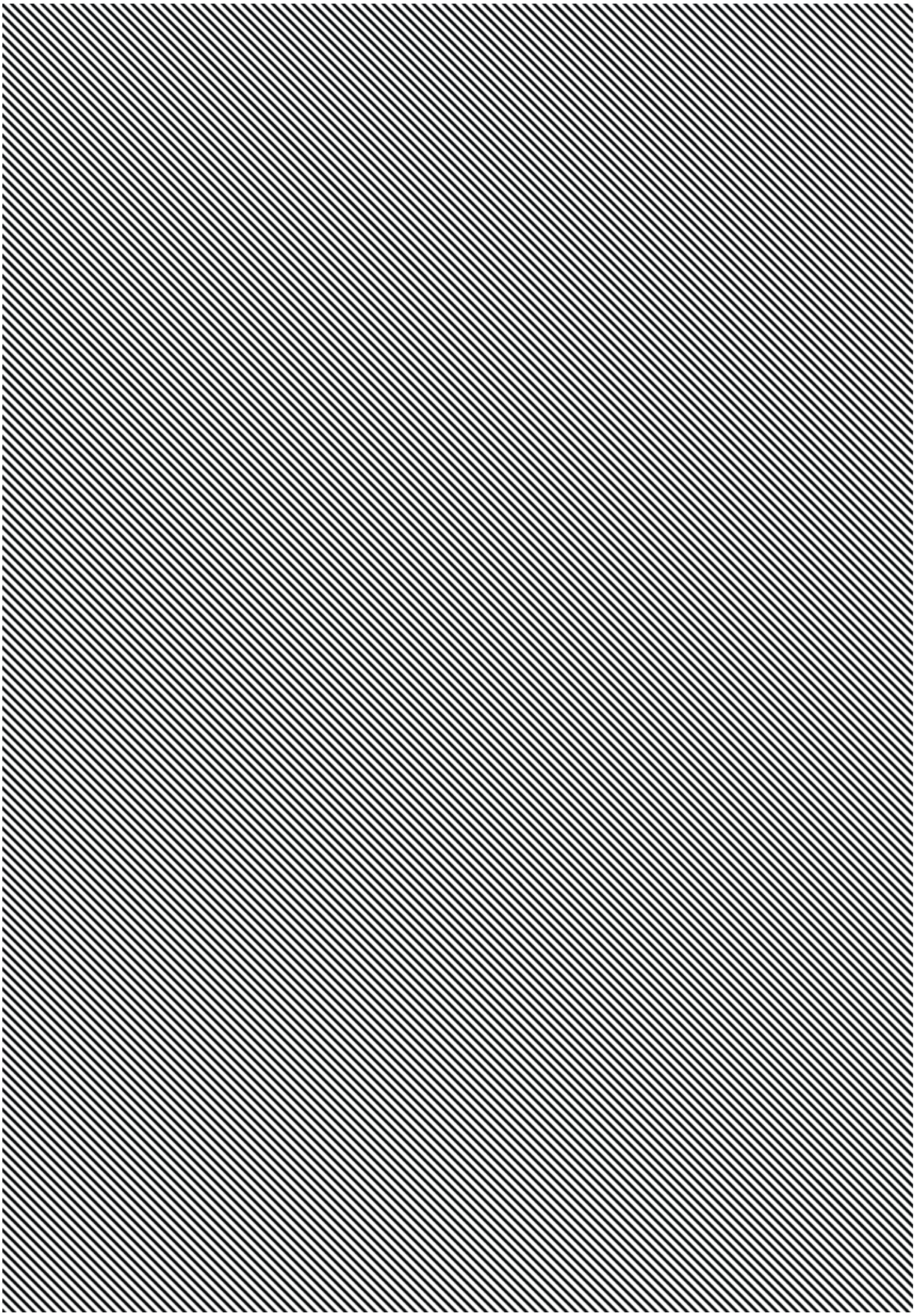

6 References

[1] Rodrigues, A.E.; Minceva, M., Modelling and simulation in chemical engineering: Tools for process innovation. *Computers & Chemical Engineering* **2005,** *29*, (6), 1167-1183.

[2] Le-Minh, N.; Khan, S.J.; Drewes, J.E.; Stuetz, R.M., Fate of antibiotics during municipal water recycling treatment processes. *Water Research* **2010,** *44*, (15), 4295-4323.

[3] Richardson, S.D., Environmental Mass Spectrometry: Emerging Contaminants and Current Issues. *Analytical Chemistry* **2011,** *84*, (2), 747-778.

[4] Comninellis, C.; Kapalka, A.; Malato, S.; Parsons, S.A.; Poulios, I.; Mantzavinos, D., Advanced oxidation processes for water treatment: advances and trends for R&D. *Journal of Chemical Technology & Biotechnology* **2008,** *83*, (6), 769-776.

[5] Andreozzi, R.; Caprio, V.; Insola, A.; Marotta, R., Advanced oxidation processes (AOP) for water purification and recovery. *Catalysis Today* **1999,** *53*, (1), 51-59.

[6] Fenton, H.J.H., LXXIII.-Oxidation of tartaric acid in presence of iron. *Journal of the Chemical Society, Transactions* **1894,** *65*, (0), 899-910.

[7] Lapertot, M.; Ebrahimi, S.; Dazio, S.; Rubinelli, A.; Pulgarin, C., Photo-Fenton and biological integrated process for degradation of a mixture of pesticides. *Journal of Photochemistry and Photobiology A: Chemistry* **2007,** *186*, (1), 34-40.

[8] Reynolds, O., On the Dynamical Theory of Incompressible Viscous Fluids and the Determination of the Criterion. *Philosophical Transactions of the Royal Society of London. (A.)* **1895,** *186*, 123-164.

[9] Boussinesq, J., Théorie de l'Écoulement Tourbillant. *Acad. Sci. Inst. Fr.* **1877,** *23*, 46-50.

[10] Liu, D.; Ducoste, J.; Jin, S.; Linden, K., Evaluation of alternative fluence rate distribution models. *Journal of Water Supply: Research & Technology-AQUA* **2004,** *53*, (6), 391-408.

[11] Wols, B.A.; Hofman-Caris, C.H.M.; Harmsen, D.J.H.; Beerendonk, E.F.; van Dijk, J.C.; Chan, P.-S.; Blatchley, E.R., Comparison of CFD, Biodosimetry and Lagrangian Actinometry to Assess UV Reactor Performance. *Ozone: Science & Engineering* **2012,** *34*, (2), 81-91.

[12] Xu, C.; Zhao, X.S.; Rangaiah, G.P., Performance analysis of ultraviolet water disinfection reactors using computational fluid dynamics simulation. *Chemical Engineering Journal* **2013,** *221*, (0), 398-406.

[13] Sozzi, D.A.; Taghipour, F., UV Reactor Performance Modeling by Eulerian and Lagrangian Methods. *Environmental Science & Technology* **2006,** *40*, (5), 1609-1615.

[14] Mbonimpa, E.G.; Vadheim, B.; Blatchley Iii, E.R., Continuous-flow solar UVB disinfection reactor for drinking water. *Water Research* **2012,** *46*, (7), 2344-2354.

[15] Wang, Z.; Liu, J.; Dai, Y.; Dong, W.; Zhang, S.; Chen, J., CFD modeling of a UV-LED photocatalytic odor abatement process in a continuous reactor. *Journal of Hazardous Materials* **2012,** *215–216*, (0), 25-31.

[16] Ghafoori, S.; Mehrvar, M.; Chan, P.K., Photoassisted Fenton-like degradation of aqueous poly(acrylic acid): From mechanistic kinetic model to CFD modeling. *Chemical Engineering Research and Design* **in press**.

[17] Liu, Y.; Ducoste, J., Numerical simulation of chloramines formation in turbulent flow using a multi-fluid micromixing model. *Environmental Modelling & Software* **2006,** *21*, (8), 1198-1213.

[18] ANSYS *FLUENT Theory Guide / User's guide*, Version 14.5; 2013.

[19] ANSYS, I. *Introduction to ANSYS FLUENT - Customer Training Material- Turbulence Modeling* 2010.

[20] Wilcox, D.C., *Turbulence modeling for CFD*, DCW industries: 1998.

[21] Liu, D.; Wu, C.; Linden, K.; Ducoste, J., Numerical simulation of UV disinfection reactors: Evaluation of alternative turbulence models. *Applied Mathematical Modelling* **2007,** *31*, (9), 1753-1769.

[22] Bakker, A.; Haidari, A.H.; Marshall, E.M., Design reactors via CFD. *Chem. Eng. Progress* **2001**, 30–39.

[23] Bakker, A., The online CFM book home page, http://www.bakker.org/cfm/, (accessed on 2013).

[24] Cassano, A.E.; Martin, C.A.; Brandi, R.J.; Alfano, O.M., Photoreactor Analysis and Design: Fundamentals and Applications. *Industrial & Engineering Chemistry Research* **1995,** *34*, (7), 2155-2201.

[25] Blatchley Iii, E.R., Numerical modelling of UV intensity: Application to collimated-beam reactors and continuous-flow systems. *Water Research* **1997,** *31*, (9), 2205-2218.

[26] Ho, C.K., Evaluation of reflection and refraction in simulations of ultraviolet disinfection using the discrete ordinates radiation model. *Water Science & Technology* **2009,** *59*, (12), 2421-2428.

[27] Santoro, D.; Raisee, M.; Moghaddami, M.; Ducoste, J.; Sasges, M.; Liberti, L.; Notarnicola, M., Modeling Hydroxyl Radical Distribution and Trialkyl Phosphates Oxidation in UV–H2O2 Photoreactors Using Computational Fluid Dynamics. *Environmental Science & Technology* **2010,** *44*, (16), 6233-6241.

[28] Pignatello, J.J.; Oliveros, E.; MacKay, A., Advanced Oxidation Processes for Organic Contaminant Destruction Based on the Fenton Reaction and Related Chemistry. *Critical Reviews in Environmental Science and Technology* **2006,** *36*, (1), 1-84.

[29] White, F.M., *Fluid Mechanics*, 4th Edition, McGraw-Hill.

[30] Goudar, C.T.; Sonnad, J.R., Comparison of the iterative approximations of the Colebrook-White equation. *Hydrocarbon Processing* **2008,** *87*, (8), 79-+.

[31] Bird, R.B.; Stewart, W.E.; E. N. Lightfoot, *Transport phenomena*, 2nd ed., John Wiley and Sons, Inc.: New York 2002.

[32] Gas Dynamics Laboratory, Princeton University, http://www.princeton.edu/~gasdyn/#superpipe_data, (accessed on 2013).

[33] Eggels, J.G.M.; Westerweel, J.; Nieuwstadt, F.T.M.; Adrian, R.J., Direct numerical simulation of turbulent pipe flow. *Applied Scientific Research* **1993,** *51*, (1-2), 319-324.

[34] Shames, I.H., *MECHANICS OF FLUIDS*, 3rd edition, McGraw-Hill, Inc.: 2003.

[35] Danckwerts, P.V., Continuous flow systems: Distribution of residence times. *Chemical Engineering Science* **1953,** *2*, (1), 1-13.

[36] Levenspiel, O., *Chemical Reaction Engineering*, 3rd ed., John Wiley & Sons: 1999.

[37] FOGLER, H.S., *Elements of Chemical Reaction Engineering*, Prentice Hall PTR: 2006.

[38] Vincent, G.; Schaer, E.; Marquaire, P.-M.; Zahraa, O., CFD modelling of an annular reactor, application to the photocatalytic degradation of acetone. *Process Safety and Environmental Protection* **2011,** *89*, (1), 35-40.

[39] Wang, K.-H.; Tsai, H.-H.; Hsieh, Y.-H., The kinetics of photocatalytic degradation of trichloroethylene in gas phase over TiO2 supported on glass bead. *Applied Catalysis B: Environmental* **1998,** *17*, (4), 313-320.

[40] Ollis, D.F., Kinetics of Liquid Phase Photocatalyzed Reactions: An Illuminating Approach†. *The Journal of Physical Chemistry B* **2005,** *109*, (6), 2439-2444.

APPENDICES

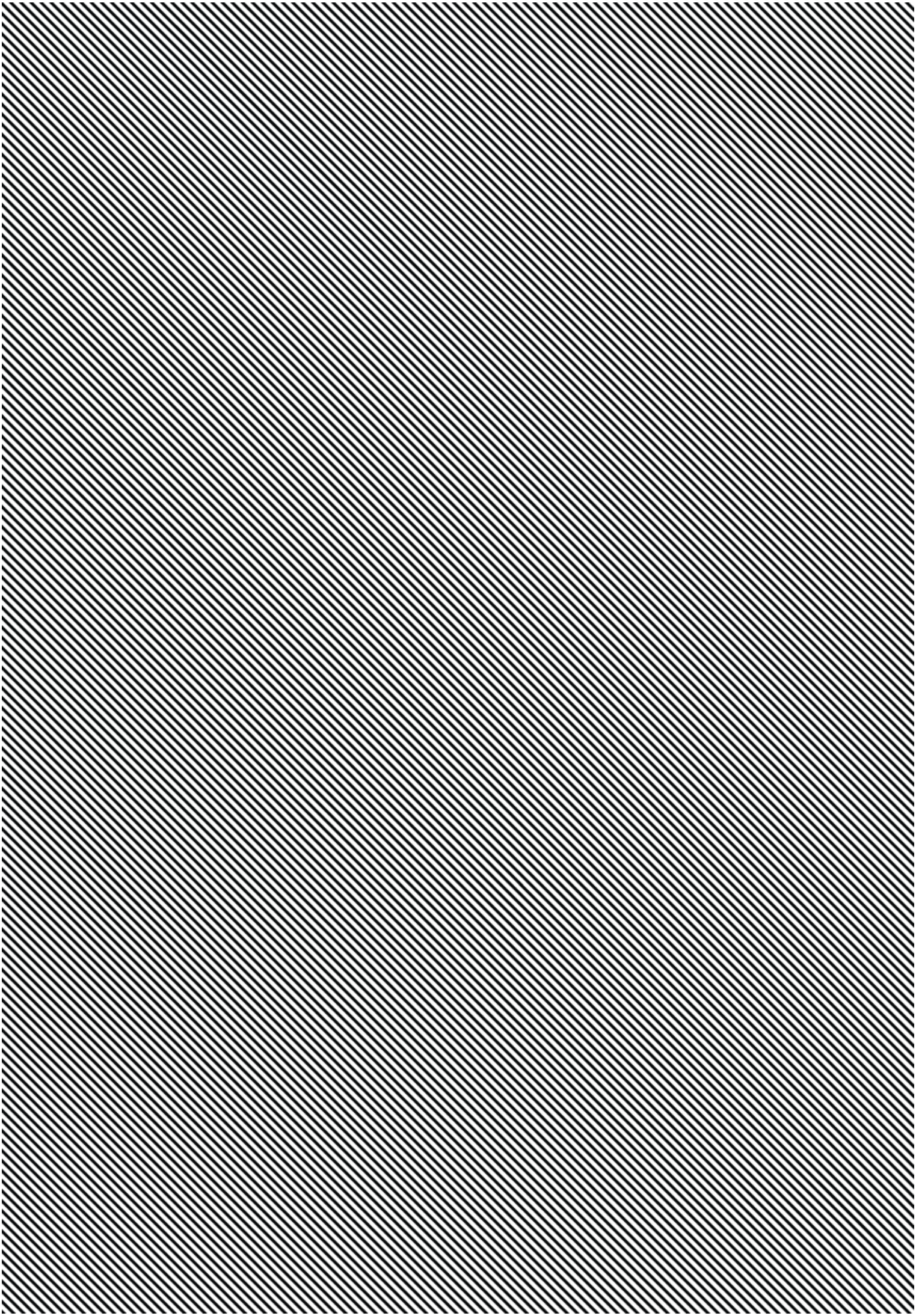

APPENDIX A – ANSYS WORKBENCH

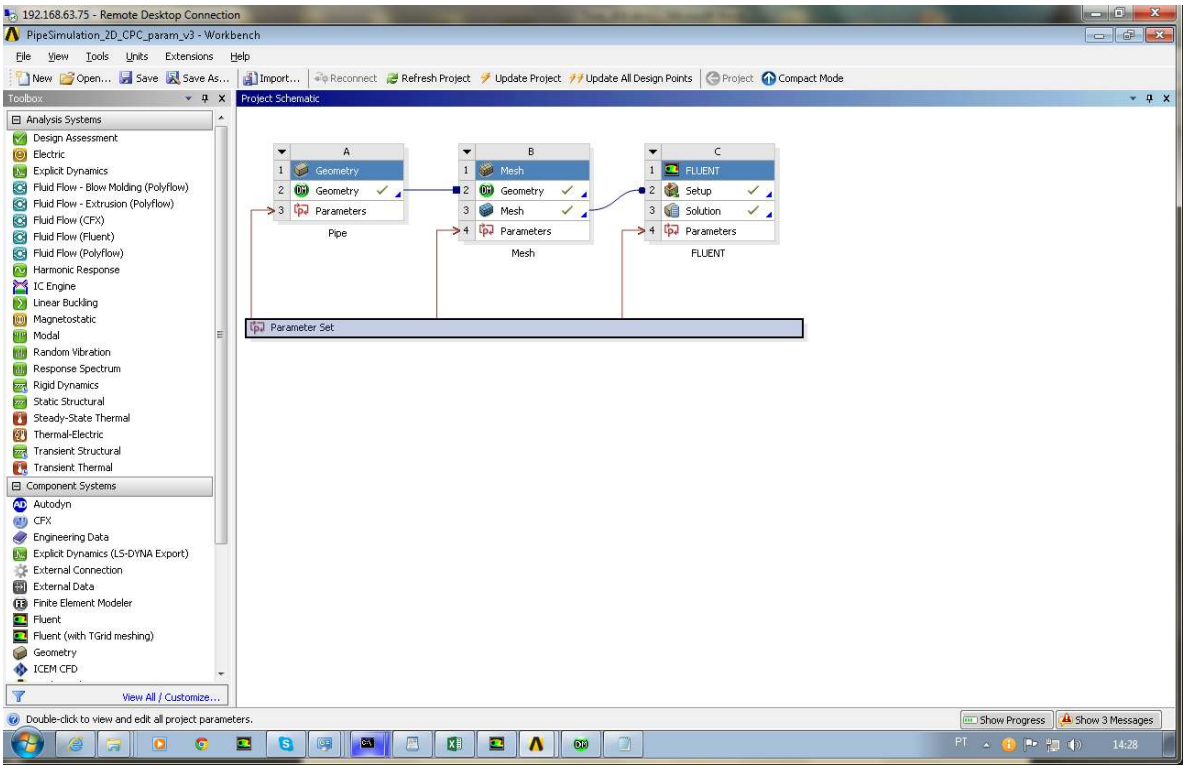

Appendix figure 1 – ANSYS WORKBENCH environment window

a)

Outline: No data

	A	B	C	D
1	ID	Parameter Name	Value	Unit
2	Input Parameters			
3	Pipe (A1)			
4	P6	Radius	0,0232	
5	P5	Length	1,5	
6	Mesh (B1)			
7	P24	Edge Sizing 2 Number of Divisions	57	
8	P25	Edge Sizing 2 Bias Factor	228,76	
9	P26	Edge Sizing 3 Number of Divisions	57	
10	P27	Edge Sizing 3 Bias Factor	228,76	
11	P28	Edge Sizing Number of Divisions	1000	
12	FLUENT (C1)			
13	P29	density	1000	kg m^-3
14	P30	viscosity	0,001	Pa s
15	P31	diameter	0,0464	m
16	P32	velocity	2,1552	m s^-1
17	P33	intensity-turb	0,05	
18	P34	Re_input	1E+05	
19	P35	Di_input	0,0464	
20	P36	Density_input	1000	
21	P37	Viscosity_input	0,001	
22	P38	Rughness_input	0	
23	P39	Inflation_input	1,1	
*	New input parameter	New name	New expression	
25	Output Parameters			
46	Charts			

b)

Outline: No data

	A	B	C	D
1	ID	Parameter Name	Value	Unit
2	Input Parameters			
25	Output Parameters			
26	P3	Re	1E+05	
27	P4	Diameter	0,0464	
28	P7	Density	1000	
29	P8	Viscosity	0,001	
30	P9	Roughness	0	
31	P10	y+=1	9,7848E-06	
32	P11	Friction velocity	0,1022	
33	P12	a	0,86859	
34	P13	b	0	
35	P14	d	45868	
36	P15	s	10,734	
37	P16	q	8,7679	
38	P17	g	8,5624	
39	P18	z	0,023716	
40	P19	dla	0,021236	
41	P20	dcfa	0,021238	
42	P21	Darcy FF	0,01799	
43	P22	Velocity	2,1552	
44	P23	Inflation	1,1	
*	New output parameter		New expression	
46	Charts			

Appendix figure 2 – ANSYS WORKBENCH detail of a) - inputs (provided and calculated) and, b) - outputs, either for design and/or parametric studies.

Intentionally left blank

APPENDIX B – Preliminary 3D Model

As proposed for future developments, in order to overcome inherent 2D models limitations, and allow for direct Solar Radiation a 3D model was started to be developed. Due to time limitations this wasn't implemented. The 3D model should then allow for the usage of a Solar Radiation Load, available in Discrete Ordinates radiation model. Therefore, care was taken so that the dimensions and shapes were reliable to the pilot plant specifications. Thus, the typical CPC involution was created in Excel, exported to SolidWorks, and exported again as *Parasolid* for usage in ANSYS DESIGN MODELLER. After some manipulation steps, the result can be seen in the following picture:

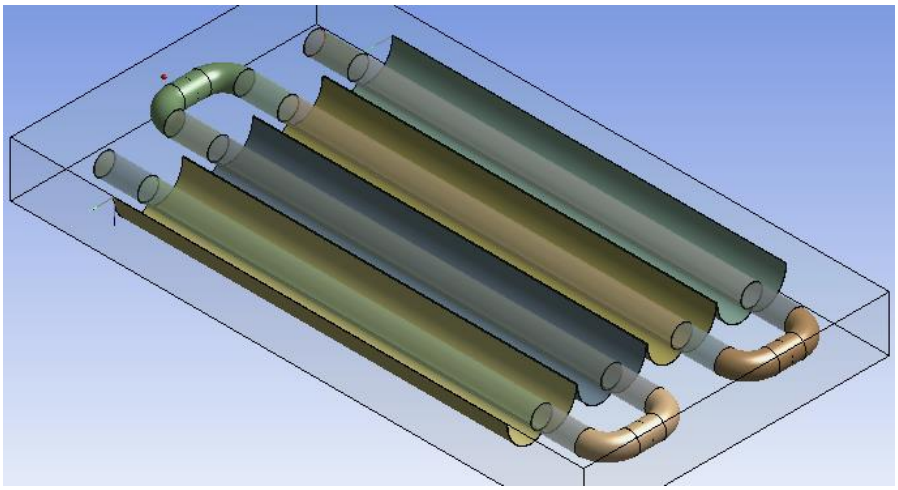

Appendix figure 3- Full pilot plant 3D model

This can be further simplified, as needed, to a unitary CPC:

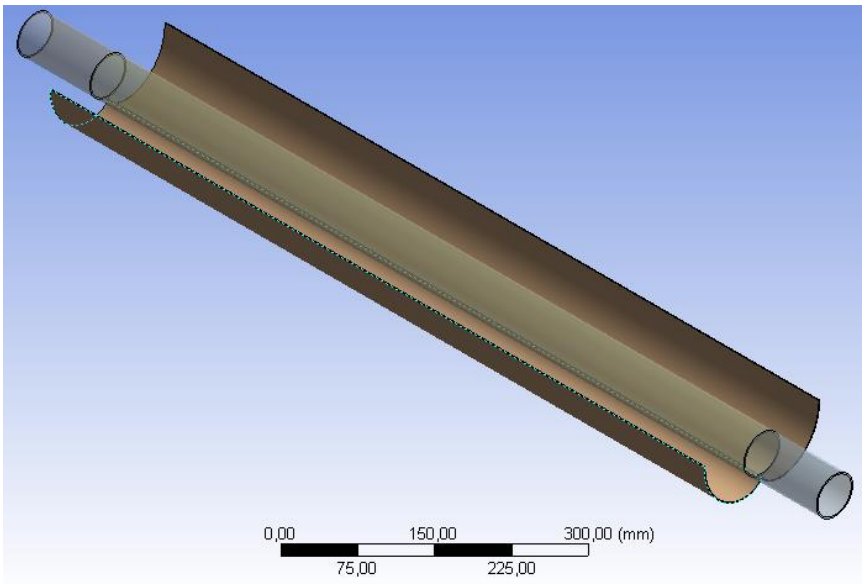

Appendix figure 4 – Unitary CPC 3D model

Intentionally left blank

APPENDIX C – Example Journal File

The file presented as example show the outline used to feedback the velocity profiles after the solution have converged.

```
/file/read-case-data "15D"
/file/write-profile "15D_out_prof_1" outlet () velocity-magnitude turb-kinetic-energy specific-diss-rate quit
/file/read-profile "15D_out_prof_1"
/plot/plot yes "15D_wall-shear-stress_1" y y 1 0 no no wall-shear wall ()
/plot/plot y "15D_vel_mag_out_1" y y 0 1 no no velocity-magnitude outlet ()
/plot/plot yes "15D_turb_k_e_out_1" y y 0 1 no no turb-kinetic-energy outlet ()
/report/surface-integrals/area-weighted-avg outlet () velocity-magnitude y "15D_vel_mag_out_awavg_1"
/define/boundary-conditions/velocity-inlet inlet no no yes yes n y n "outlet" "velocity-magnitude" n 0. y y n
"outlet" "turb-kinetic-energy" y n "outlet" "specific-diss-rate"
it 10000
/file/write-profile "15D_out_prof_2" outlet () velocity-magnitude turb-kinetic-energy specific-diss-rate quit
/file/read-profile "15D_out_prof_2"
/plot/plot yes "15D_wall-shear-stress_2" y y 1 0 no no wall-shear wall ()
/plot/plot y "15D_vel_mag_out_2" y y 0 1 no no velocity-magnitude outlet ()
/plot/plot yes "15D_turb_k_e_out_2" y y 0 1 no no turb-kinetic-energy outlet ()
/report/surface-integrals/area-weighted-avg outlet () velocity-magnitude y "15D_vel_mag_out_awavg_2"
it 10000
/file/write-profile "15D_out_prof_3" outlet () velocity-magnitude turb-kinetic-energy specific-diss-rate quit
/file/read-profile "15D_out_prof_3"
/plot/plot yes "15D_wall-shear-stress_3" y y 1 0 no no wall-shear wall ()
/plot/plot y "15D_vel_mag_out_3" y y 0 1 no no velocity-magnitude outlet ()
/plot/plot yes "15D_turb_k_e_out_3" y y 0 1 no no turb-kinetic-energy outlet ()
/report/surface-integrals/area-weighted-avg outlet () velocity-magnitude y "15D_vel_mag_out_awavg_3"
it 10000
/file/write-profile "15D_out_prof_4" outlet () velocity-magnitude turb-kinetic-energy specific-diss-rate quit
/file/read-profile "15D_out_prof_4"
/plot/plot yes "15D_wall-shear-stress_4" y y 1 0 no no wall-shear wall ()
/plot/plot y "15D_vel_mag_out_4" y y 0 1 no no velocity-magnitude outlet ()
/plot/plot yes "15D_turb_k_e_out_4" y y 0 1 no no turb-kinetic-energy outlet ()
/report/surface-integrals/area-weighted-avg outlet () velocity-magnitude y "15D_vel_mag_out_awavg_4"
/file/write-case-data "15D-end.cas.gz"
/file/read-case-data "20D"
/file/write-profile "20D_out_prof_1" outlet () velocity-magnitude turb-kinetic-energy specific-diss-rate quit
/file/read-profile "20D_out_prof_1"
/plot/plot yes "20D_wall-shear-stress_1" y y 1 0 no no wall-shear wall ()
/plot/plot y "20D_vel_mag_out_1" y y 0 1 no no velocity-magnitude outlet ()
/plot/plot yes "20D_turb_k_e_out_1" y y 0 1 no no turb-kinetic-energy outlet ()
/report/surface-integrals/area-weighted-avg outlet () velocity-magnitude y "20D_vel_mag_out_awavg_1"
/define/boundary-conditions/velocity-inlet inlet no no yes yes n y n "outlet" "velocity-magnitude" n 0. y y n
"outlet" "turb-kinetic-energy" y n "outlet" "specific-diss-rate"
it 10000
/file/write-profile "20D_out_prof_2" outlet () velocity-magnitude turb-kinetic-energy specific-diss-rate quit
/file/read-profile "20D_out_prof_2"
/plot/plot yes "20D_wall-shear-stress_2" y y 1 0 no no wall-shear wall ()
/plot/plot y "20D_vel_mag_out_2" y y 0 1 no no velocity-magnitude outlet ()
/plot/plot yes "20D_turb_k_e_out_2" y y 0 1 no no turb-kinetic-energy outlet ()
```

```
/report/surface-integrals/area-weighted-avg outlet () velocity-magnitude y "20D_vel_mag_out_awavg_2"
it 10000
/file/write-profile "20D_out_prof_3" outlet () velocity-magnitude turb-kinetic-energy specific-diss-rate quit
/file/read-profile "20D_out_prof_3"
/plot/plot yes "20D_wall-shear-stress_3" y y 1 0 no no wall-shear wall ()
/plot/plot y "20D_vel_mag_out_3" y y 0 1 no no velocity-magnitude outlet ()
/plot/plot yes "20D_turb_k_e_out_3" y y 0 1 no no turb-kinetic-energy outlet ()
/report/surface-integrals/area-weighted-avg outlet () velocity-magnitude y "20D_vel_mag_out_awavg_3"
it 10000
/file/write-profile "20D_out_prof_4" outlet () velocity-magnitude turb-kinetic-energy specific-diss-rate quit
/file/read-profile "20D_out_prof_4"
/plot/plot yes "20D_wall-shear-stress_4" y y 1 0 no no wall-shear wall ()
/plot/plot y "20D_vel_mag_out_4" y y 0 1 no no velocity-magnitude outlet ()
/plot/plot yes "20D_turb_k_e_out_4" y y 0 1 no no turb-kinetic-energy outlet ()
/report/surface-integrals/area-weighted-avg outlet () velocity-magnitude y "20D_vel_mag_out_awavg_4"
/file/write-case-data "20D_end.cas.gz"
/file/read-case-data "30D"
/file/write-profile "30D_out_prof_1" outlet () velocity-magnitude turb-kinetic-energy specific-diss-rate quit
/file/read-profile "30D_out_prof_1"
/plot/plot yes "30D_wall-shear-stress_1" y y 1 0 no no wall-shear wall ()
/plot/plot y "30D_vel_mag_out_1" y y 0 1 no no velocity-magnitude outlet ()
/plot/plot yes "30D_turb_k_e_out_1" y y 0 1 no no turb-kinetic-energy outlet ()
/report/surface-integrals/area-weighted-avg outlet () velocity-magnitude y "30D_vel_mag_out_awavg_1"
/define/boundary-conditions/velocity-inlet inlet no no yes yes n y n "outlet" "velocity-magnitude" n 0. y y n
"outlet" "turb-kinetic-energy" y n "outlet" "specific-diss-rate"
it 10000
/file/write-profile "30D_out_prof_2" outlet () velocity-magnitude turb-kinetic-energy specific-diss-rate quit
/file/read-profile "30D_out_prof_2"
/plot/plot yes "30D_wall-shear-stress_2" y y 1 0 no no wall-shear wall ()
/plot/plot y "30D_vel_mag_out_2" y y 0 1 no no velocity-magnitude outlet ()
/plot/plot yes "30D_turb_k_e_out_2" y y 0 1 no no turb-kinetic-energy outlet ()
/report/surface-integrals/area-weighted-avg outlet () velocity-magnitude y "30D_vel_mag_out_awavg_2"
it 10000
/file/write-profile "30D_out_prof_3" outlet () velocity-magnitude turb-kinetic-energy specific-diss-rate quit
/file/read-profile "30D_out_prof_3"
/plot/plot yes "30D_wall-shear-stress_3" y y 1 0 no no wall-shear wall ()
/plot/plot y "30D_vel_mag_out_3" y y 0 1 no no velocity-magnitude outlet ()
/plot/plot yes "30D_turb_k_e_out_3" y y 0 1 no no turb-kinetic-energy outlet ()
/report/surface-integrals/area-weighted-avg outlet () velocity-magnitude y "30D_vel_mag_out_awavg_3"
it 10000
/file/write-profile "30D_out_prof_4" outlet () velocity-magnitude turb-kinetic-energy specific-diss-rate quit
/file/read-profile "30D_out_prof_4"
/plot/plot yes "30D_wall-shear-stress_4" y y 1 0 no no wall-shear wall ()
/plot/plot y "30D_vel_mag_out_4" y y 0 1 no no velocity-magnitude outlet ()
/plot/plot yes "30D_turb_k_e_out_4" y y 0 1 no no turb-kinetic-energy outlet ()
/report/surface-integrals/area-weighted-avg outlet () velocity-magnitude y "30D_vel_mag_out_awavg_4"
/file/write-case-data "30D_end.cas.gz"
/file/read-case-data "40D"
/file/write-profile "40D_out_prof_1" outlet () velocity-magnitude turb-kinetic-energy specific-diss-rate quit
/file/read-profile "40D_out_prof_1"
/plot/plot yes "40D_wall-shear-stress_1" y y 1 0 no no wall-shear wall ()
/plot/plot y "40D_vel_mag_out_1" y y 0 1 no no velocity-magnitude outlet ()
/plot/plot yes "40D_turb_k_e_out_1" y y 0 1 no no turb-kinetic-energy outlet ()
/report/surface-integrals/area-weighted-avg outlet () velocity-magnitude y "40D_vel_mag_out_awavg_1"
```

```
/define/boundary-conditions/velocity-inlet inlet no no yes yes n y n "outlet" "velocity-magnitude" n 0. y y n
"outlet" "turb-kinetic-energy" y n "outlet" "specific-diss-rate"
it 10000
/file/write-profile "40D_out_prof_2" outlet () velocity-magnitude turb-kinetic-energy specific-diss-rate quit
/file/read-profile "40D_out_prof_2"
/plot/plot yes "40D_wall-shear-stress_2" y y 1 0 no no wall-shear wall ()
/plot/plot y "40D_vel_mag_out_2" y y 0 1 no no velocity-magnitude outlet ()
/plot/plot yes "40D_turb_k_e_out_2" y y 0 1 no no turb-kinetic-energy outlet ()
/report/surface-integrals/area-weighted-avg outlet () velocity-magnitude y "40D_vel_mag_out_awavg_2"
it 10000
/file/write-profile "40D_out_prof_3" outlet () velocity-magnitude turb-kinetic-energy specific-diss-rate quit
/file/read-profile "40D_out_prof_3"
/plot/plot yes "40D_wall-shear-stress_3" y y 1 0 no no wall-shear wall ()
/plot/plot y "40D_vel_mag_out_3" y y 0 1 no no velocity-magnitude outlet ()
/plot/plot yes "40D_turb_k_e_out_3" y y 0 1 no no turb-kinetic-energy outlet ()
/report/surface-integrals/area-weighted-avg outlet () velocity-magnitude y "40D_vel_mag_out_awavg_3"
it 10000
/file/write-profile "40D_out_prof_4" outlet () velocity-magnitude turb-kinetic-energy specific-diss-rate quit
/file/read-profile "40D_out_prof_4"
/plot/plot yes "40D_wall-shear-stress_4" y y 1 0 no no wall-shear wall ()
/plot/plot y "40D_vel_mag_out_4" y y 0 1 no no velocity-magnitude outlet ()
/plot/plot yes "40D_turb_k_e_out_4" y y 0 1 no no turb-kinetic-energy outlet ()
/report/surface-integrals/area-weighted-avg outlet () velocity-magnitude y "40D_vel_mag_out_awavg_4"
/file/write-case-data "40D_end.cas.gz"
```

Intentionally left blank

APPENDIX D – UDF/Custom Field Functions

UDF for chemical reaction / radiation coupling

```
/************************************************************************
        rate.c
        UDF for computing UV Fluence rate
************************************************************************/

#include "udf.h"
#define C_DO(c,t)C_STORAGE_R_XV(c,t,SV_DO_IRRAD,0)

DEFINE_VR_RATE(first_order_rate,c,t,r,wk,yk,rate,rr_t)
{
        real ci, prod, I, rmax, eps, radius, x[ND_ND];
        int  i;

        /* calculate concentration of reagent(s) */

        prod = 1;

        for(i = 0; i < r->n_reactants; i++)
        {
                ci= C_R(c,t) * yk[r->reactant[i]] / wk[r->reactant[i]];
                prod  *= pow(ci, r->exp_reactant[i]);
        }

        /* please note: the FLUENT UI is used to pass K (= A) values to the UDF*/

        *rate = r->A * prod;

        *rr_t = *rate;
}

DEFINE_VR_RATE(UV_fluence_rate,c,t,r,wk,yk,rate,rr_t)
{
        real ci, prod, I, rmax, eps, radius, x[ND_ND];
        int  i;

        rmax=0.0232; /* m */
        eps=183.5; /* l/(g m) */


        C_CENTROID(x,c,t);

        /*for 3D: radius=sqrt(pow(x[1],2)+pow(x[2],2));*/

        /*for 2D: */

        radius=x[1];

        /* aproximate radiation intensity (I) based on Lambert-Beer's law */
```

```
        I=50*exp(-eps*(rmax-radius));

        /* calculate concentration of reagent(s) */

        prod = 1;

        for(i = 0; i < r->n_reactants; i++)
        {
                ci= C_R(c,t) * yk[r->reactant[i]] / wk[r->reactant[i]];
                prod  *= pow(ci, r->exp_reactant[i]);
        }

        /* please note: the FLUENT UI is used to pass K (= A) values to the UDF*/

        *rate = r->A * prod * I / 30;

        *rr_t = *rate;
}

DEFINE_VR_RATE(ordinates_UV_rate,c,t,r,wk,yk,rate,rr_t)
{
        real ci, prod, I;
        int  i;


        /* get UV Intensity */

        I=C_DO(c,t);

        /* calculate concentration of reagent(s) */

        prod = 1;

        for(i = 0; i < r->n_reactants; i++)
        {
                ci= C_R(c,t) * yk[r->reactant[i]] / wk[r->reactant[i]];
                prod  *= pow(ci, r->exp_reactant[i]);
        }

        I=pow(I, r->b);
        /* please note: the FLUENT UI is used to pass k0 (=A) and alpha (=b) values to the UDF*/
        *rate = r->A * prod * I;

        *rr_t = *rate;
}
DEFINE_VR_RATE(normal_DO_UV_rate,c,t,r,wk,yk,rate,rr_t)
{
        real ci, prod, I;
        int  i;


        /* get UV Intensity */

        I=C_DO(c,t);
        /* normalize UV Intensity */
```

```
        I=I/98.757416;
        /* set maximum UV Intensity =30w/m2 */
        I=I*30;
        /* calculate concentration of reagent(s) */

        prod = 1;

        for(i = 0; i < r->n_reactants; i++)
        {
                ci= C_R(c,t) * yk[r->reactant[i]] / wk[r->reactant[i]];
                prod  *= pow(ci, r->exp_reactant[i]);
        }

        I=pow(I, r->b);

        *rate = r->A * prod * I;

        *rr_t = *rate;
}
```

Custom Field Functions

S_{ij}

```
1 / 2 * (dradial-velocity-dx + daxial-velocity-dy)
```

$u_i u_j$

```
- 2 * viscosity-turb / density * sij
```

UDF Velocity Profile Example

```
#include "udf.h"

DEFINE_PROFILE(turb_profile, thread, position)
{
        real x[ND_ND];
        real r;
        real rmax;
        real vmed;
        real dens;
        real visc;
        real roughness;
        real a;
        real b;
        real d;
        real s;
        real q;
        real g;
        real z;
        real dla;
        real dcfa;
        real darcy_ff;
        real frict_vel;
        face_t f;

        /* Insert Parameters below */
```

```
        rmax=0.0645; /* m */
        vmed=0.7752; /* m/s */
        dens=1000.; /* kg/m3 */
        visc=1.0e-3; /* Pa.s */
        roughness=0; /* m */

        a=2./log(10.);
        b=(roughness/(2.*rmax))/3.7;
        d=log(10.)*dens*vmed*2.*rmax/(5.02*visc);
        s=b *d+log(d);
        q=pow(s,(s/(s+1)));
        g=b*d+log(d/q);
        z=log(q/g);
        dla=z*g/(g+1.);
        dcfa=dla*(1.+(z/2.)/(pow((g+1.),2)+(z/3.)*(2.*g-1.)));

        darcy_ff=pow((1./(a*(log(d/q)+dcfa))),2);

        frict_vel=sqrt(darcy_ff*pow(vmed,2)/8.); /* m/s */

        begin_f_loop(f, thread)
        {
                F_CENTROID(x,f,thread);

                r = sqrt(pow(x[1],2)+pow(x[2],2));

                if(((rmax-r)*frict_vel*dens/visc)>=11.63505667)
                        F_PROFILE(f,thread, position)=frict_vel*(2.5*log((rmax-r)*frict_vel*dens/visc)+5.5);
                else
                        F_PROFILE(f,thread, position)=(rmax-r)*pow(frict_vel,2)*dens/visc;

        }
        end_f_loop(f, thread)

}
```

APPENDIX E – Glossary of Photocat. Terms

Some Photocatalysis terms are provided below for reference, as taken from:

Silvia E. Braslavsky, André M. Braun, Alberto E. Cassano, Alexei V. Emeline, Marta I. Litter, Leonardo Palmisano, Valentin N. Parmon, and Nick Serpone, ***Glossary of terms used in photocatalysis and radiation catalysis (IUPAC Recommendations 2011)***, Pure Appl. Chem., Vol. 83, No. 4, pp. 931–1014, 2011.

absorption (of electromagnetic radiation)

Transfer of energy from an electromagnetic field to a material or a molecular entity.

efficiency (of a step)

Ratio between the useful energy delivered or bound and the energy supplied, i.e., energy output/energy input.

einstein

One mol of photons. Widely used, although it is neither an SI unit nor recognised to be used with the SI.

energy transfer

excitation transfer

Process by which a molecular entity is excited (e.g., by absorption of ultraviolet, visible, or infrared radiation or by chemiexcitation) and a phenomenon (a physical or a chemical process) originates from the excited state of another molecular entity, which has interacted with the originally absorbing entity.

fluence,

radiant energy fluence

Radiant energy, Q, incident on a small sphere from all directions divided by the cross-sectional area of that sphere. SI unit is J m^{-2}.

fluence rate

radiant energy fluence rate

Total radiant power, P, incident from all directions onto a small sphere divided by the cross-sectional area of that sphere. SI unit is W m^{-2}.

intensity (of a spectral feature)

Describes the magnitude of the particular feature in the spectrum.

irradiance (at a point of a surface), E

Radiant power, P, of all wavelengths incident from all upward directions on a small element of surface containing the point under consideration divided by the area of the element. SI unit is Wm^{-2}.

LVREA

Abbreviation of *local volumetric rate of energy absorption*.

LVRPA

Abbreviation of *local volumetric rate of photon absorption*.

photocatalysis

Change in the rate of a chemical reaction or its initiation under the action of ultraviolet, visible, or infrared radiation in the presence of a substance—the photocatalyst—that absorbs light and is involved in the chemical transformation of the reaction partners.

quantum yield

Number of defined events, occurring per photon absorbed by the system at a specified wavelength.

radiance

Radiant power, P, leaving or passing through a small transparent element of surface in a given direction from the source about the solid angle Ω, divided by the solid angle and by the orthogonally projected area of the element in a plane normal to the given beam direction, $dS_{\perp} = dS\ cos\theta$.

radiant dose

Radiant energy (Q, SI unit is J) or amount of photons (in mol or the non-SI unit einstein) absorbed per area or volume by an object irradiated during a given exposure time.

radiant energy, Q, W

Total energy emitted, transferred or received as radiation of all wavelengths in a defined period of time. SI unit is J.

radiant intensity, I

intensity

Radiant power, P, at all wavelengths per solid angle, Ω. The radiant power emitted in a given direction by a source or an element of the source in a small cone containing the given direction divided by the solid angle of the cone. SI unit is Wsr^{-1}.

radiant power, P

Power emitted, transferred or received as radiation. SI unit is $J\ s^{-1} = W$.

radiation

Term embracing electromagnetic waves as well as fast-moving particles. In radioanalytical chemistry the term usually refers to radiation emitted during a nuclear process (e.g., radioactive decay, nuclear reaction, nuclear fission, accelerators). NOTE: In this Glossary, however, in general we refer to radiation as embracing electromagnetic waves from all wavelength and not fast-moving particles.